Experimental and theoretical study of a compression/absorption heat pump with ammonia/water as working fluid

by
Stein Rune Nordtvedt

Thesis submitted in partial fullfilment of the requirements
for the degree of Doktor Ingeniør (Ph.D.)

Norwegian University of Science and Technology
Faculty of Mechanical Engineering
Department of Refrigeration and Air-Conditioning

Trondheim, 2005

Preface

This thesis presents the results of a doctoral engineering project carried out at the Norwegian University of Science and Technology (NTNU), Department of Refrigeration and Air Conditioning, during the period from June 1998 through February 2005.

The project has been made possible and carried out with financial support from the Norwegian Research Council (NFR) and the project group consisting of Alfa Laval AS, York Refrigeration and Mobil. Their support have been highly appreciated.

I would like to thank Institute for Energy Technology (IFE) and my colleagues at the department of Energy Systems (ENSYS) for letting me work here, and the Norwegian Research Council (NFR) for sponsoring the study through a strategic institute program (SIP).

My supervisors have been Professor Arne M. Bredesen,NTNU, Professor Geir A. Owren, NTNU, and Dr. Svein Grandum, IFE. Their supervision and support during the progress of my work have been highly appreciated.

A special thank to Bjarne Horntvedt and Tove Risberg at IFE for fruitful discussions and help.

Finally, I am thankful to my life companion, Aud, the her everlasting patience and help during writing and compiling this work.

Kjeller, Norway
April, 2005

Stein Rune Nordtvedt

Abstract

In several industrial processes, a large amount of thermal energy in the form of low-grade energy is released to the surroundings due to difficulties of transforming the energy into useful high-grade energy. High-grade energy fluids can typically be water at temperatures above 100 ° C. Conventional heat pumps have limitations of delivering such high temperatures. Because of the unknown consequences and impact of synthetic working fluids, the future solutions will probably involve mainly natural working fluids. The aim of this project was to find a heat pump solution with a natural working fluid, capable of upgrading waste heat from industrial processes to at least 90 to 100 ° C. A survey of the alternative working fluids leads to the mixture of ammonia and water. Temperatures between -10 to +160 ° C are feasible with ammonia water as working fluid, and with system pressures below 20 bars.

A compression/absorption heat pump cycle using ammonia/water as working fluid offer advantages like high temperature lifts, low-pressure ratios and capacity control. A laboratory compression/absorption heat pump was designed and built at Institute for Energy Technology (IFE) to study the performance potential of such a heat pump. To ensure that the technology is feasible for the industry and economical comparable to other alternatives, the cost involved must be competitive. This means, as far as possible choosing standard refrigeration components. Another important issue is to reduce the physical dimensions of the apparatus, in particularly the heat exchangers. Therefore plate heat exchangers have been chosen, which are very compact and effective, but usually not preferred for absorption applications.

A steady-state computer model of the compression/absorption heat pump cycle was developed, and used to find the design conditions for the heat pump components. A heating COP of 3.41 was predicted at the design condition, where the heat pump heats water from 50 to 96 ° C, and cools water from 50 to 6 ° C. A second law analysis of the heat pump cycle was carried out.

The test plant was built based on a two-stage reciprocating ammonia compressor. The compressor is oil lubricated and has water-cooled cylinder heads. A membrane pump was chosen as solution pump. In addition a turbine pump was installed as a booster pump upstream the solution pump. All heat exchanger in contact with the working fluid are nickel-brazed plate heat exchangers. Tests verified the capability to vary the heat capacity. The heating capacity was varied from 30 to 47kW. A heating COP of 2.47 was measured when heating water from 50 to 93 ° C, and at the same time cooling water from 50 to 17 ° C. Several losses were found in the test unit. If these losses were accounted for, the heating COP would increase to 3.05.

A computer model for the design of the absorber and the desorber using plate heat exchangers was developed. The method by Silver for prediction of the effective two-phase heat transfer coefficient during condensation and evaporation was implemented into the model. The one-phase forced convection heat transfer coefficient was predicted with an empirical correlation provided by the heat exchanger manufacturer. The two-phase pressure drop was predicted

using the Lockhart-Martinelli method. The model was compared with experimental results. The predicted heat transfer coefficients were 2.2 to 2.5 times the experimental values in the absorber, and 3.2 to 3.9 times the experimental values in the desorber. The mismatch between the model predictions and the experimental results can be explained by the combined effect of poor solution distribution and surface wetting and an oil film on the heat transfer surface. To account for potential solution distribution and inadequate wetting problems, a correction factor in the form of an area effectiveness ratio was introduced. The area effectiveness factor is defined as the ratio between the effective heat transfer surface to the actual heat transfer surface. The value of the area effectiveness ratio required achieving correspondence between model and experiment varied from 0.27 to 0.32 in the absorber, and from 0.28 to 0.30 in the desorber. The effect of an oil film on the overall heat transfer coefficient surface was predicted. The reduction of the overall heat transfer coefficient in the absorber increases from 17% to 68% when the oil film thickness increases from 0.01mm to 0.1mm. The reduction of the overall heat transfer coefficient in the desorber was 16% for an oil film with a thickness of 0.01mm, and increases to 65% for an oil film thickness of 0.1mm. The mass transfer resistance in the vapour phase needs to be studied further.

Table of Contents

.

Nomenclature

Latin letters

A	Helmholtz free energy	kJ/kg
A_{HT}	heat transfer area	m^2
A_a	Ackermann factor	-
C_f	correction factor interfacial roughness	-
C_c	Chisholm parameter	-
COP	Coefficient of Performance	-
c_p	specific heat capacity	kJ/kg·K
CR	Circulation ratio	-
D_h	hydraulic diameter	m
D_p	port diameter	m
f	friction factor	-
$\dot{G}$	mass flux	kg/m^2
h	enthalpy	kJ/kg
L	length	m
L_h	horisontal distance between center of plate ports	m
L_p	horisontal distance between plate ports	m
L_v	vertical distance between center of plate ports	m
L_w	plate width	m
LMTD	logarithmic mean temperature difference	K
$\dot{m}$	mass flow	kg/s
M	molar mass	kg/kmol
M_c	condensation mass flux	$kg/m^2·s$
N_c	number of channels	-
Nu	Nusselt number	-
P	pressure	bar
PR	pressure ratio	-
Pr	Prandtl number	-
$\dot{q}$	heat flux	kW/m^2
Qu	vapour mass fraction	-
r	radius	m
R	area effectiveness ratio	-
R_f	thermal resistance in oil film	m^2K/kW
R_m	universal gas constant	J/mol·K
Re	Reynolds number	-
s	entropy	kJ/kg·K

T	temperature	$°C$
U	overall heat transfer coefficient	$kW/m^2 \cdot K$
u	internal energy, velocity	kJ/kg, m/s
$\dot{V}$	volume flow rate	m^3/s
W	work	kW
X_{lm}	Lockhart-Martinelli parameter	-
X	ammonia mass fraction in saturated liquid solution	kg/kg
Z	overall ammonia mass fraction	kg/kg
Z_s	parameter used in the Silver method	-

Greek letters

α	heat transfer coefficient	$kW/m^2 \cdot K$
β_f	liquid-phase mass transfer coefficient	m/s
β	corrugation angle	°
Δ	change = final minus initial	-
ε	thermal efficiency	-
η	volumetric, isentropic and second law efficiency	
θ	correction factor for condensation mass flux effects	-
σ	surface tension	N/m
τ	shear stress	$kg/m \cdot s^2$

Subscript

acc	accelerational	-
avg	average	-
bub	bubble point	-
C	cold	-
cond	condensation	-
cr	critical	-
dew	dew point	-
disp	displacement	-
eff	effective	-
fric	friction	-
film	film (heat transfer)	-
g	gas	-
gen	generation (entropy)	-
H	hot	-
hp	high-pressure	-
II	second law	-

isen	isentropic	-
l	liquid	-
lg	liquid-gas (latent heat)	-
lp	low-pressure	-
lo	liquid only	-
max	maximum	-
mix	mixture	-
nbf	nucleate boiling factor	-
rev	reversible	-
sat	saturated	-
shx1	solution heat exchanger 1	-
shx2	solution heat exchanger 2	-
sp	single-phase	-
ss	strong solution	-
tot	total	-
tp	two-phase	-
vol	volumetric	-
v	vapour	-
ws	weak solution	-
wa	water absorber	-
wd	water desorber	-

Superscripts

-

Abbrevations

CAHP	compression-absorption heat pump
CFC	chlorofluorocarbons
EES	Engineering Equation Solver
HCFC	hydrochlorofluorocarbon
HTC	heat transfer coefficient
IIR	International Institute of Refrigeration
NPSH	netto positive suction head
PAG	polyalphaglycol
PAO	polyalphaolefin

.

1 Introduction

1.1 Background

The CFCs and HCFCs were the refrigerant fluids of choice for many applications for many years up to the early 1990s, after which the non-ozone depleting HFCs became favoured. In 1987 the Montreal protocol banned production and consumption of ozone depleting compounds. The Montreal Protocol accelerated the rate of CFC and HCFC phase out in order to reduce ozone depletion, and this was only possible by using HFCs in many applications. In 1997 the Kyoto protocol introduced goals for the reduction of global warming substances.

The heat pump industry has consequently been forced to look for subtitutes for the CFCs and HCFCs. There has been a growth in use of hydrocarbons, but this has been limited by safety considerations.

Possible actions in response to climate change fall into three groups. The first is system design, which includes the selection of refrigerant cycle and refrigerant fluid, and the minimisation of refrigerant quantity and leakage. The second relates to installation and service procedures, and the third is the improvement of energy efficiency to reduce indirect emissions of carbon dioxide.

Heat pump technology decreases the use of primer energy, because heat pumps are capable to reuse waste energy or low-grade energy. In the industrial sector, the waste energy often is water with a temperature of 30-50 °C. In industrial process plants, there is an large amount of waste energy that will not be utilised because the temperature is too low. Until today, there have been few good technical and economical possibilities to upgrade the waste energy up to a more feasible high temperature. As a consequence large amount of waste heat is dumped. Commercial heat pumps with i.e. R114 have been installed for high temperature applications, but when considering the environmental impact of the CFC and HCFC working fluids, R114 is no longer an alternative. In the past decades, there have been performed considerable efforts to find heat pump solutions with natural working fluids, also for high temperature applications. Investigated solutions has mainly been water, ammonia/water and hydrocarbons.

It is often economical desirable to provide both heating and cooling duty with one system. This means that industrial heat pumps have to work with high temperature lift from heat source to heat sink to accomplish the task of working as a heater and a chiller at the same time. Vapour compression heat pumps have limitations with high temperature lifts, mainly because of the increasing pressure ratio when the temperature lift increases. This is a consequence of that most of the working fluids vapour curves are very steep, which results in a higher pressure ratio versus temperature raise. To achieve temperature lifts of more than 100 K the combination of ammonia/water is one possibility. Temperatures between -10 to +160 °C are feasible with ammonia water as working fluid, and with system pressures below

20 bars. The ammonia/water mixture is a wide-boiling mixture and undergoes large temperature changes during the phase change processes. In that way large temperature lifts are feasible with the use of counter current flow in the absorber and desorber.

To ensure that the technology is feasible for the industry and economical comparable to other alternatives, the cost involved with the energy conserving technology must be competitive. To ensure a low installation cost, standard available components is often used. Then the energy price of the upgraded waste heat can be competitive with other energy sources. From energy conservation consideration, it is often advantageous to use thermally activated systems where thermal energy can be utilised, and pure exergy like electricity used only for lighting and mechanical purposes. Compact heat exchangers can help reducing the first cost and give better safety as the fluid inventory is smaller.

There are several possibilities for high temperature applications in e.g. process industries and district heating systems. The upgraded heat can either be utilized internally in the industrial process and thereby reduce the primary energy consumption, or it can be utilized for other high temperature purposes such as drying or evaporation located close to the waste heat source. Common waste water temperature is 20-50°C, and useful high temperature heat for industrial processes should be at least 90°C.

The recent interest of compression/absorption cycles is based on two requirements: the problem of finding compression heat pumps applicable for high temperature lifts and temperatures, and the wish to use low grade heat for sorption cooling. The theoretical work on compression/absorption heat pumps is extensive. The experimental interest is strong but has not led to applications beyond several pilot plants, mainly due to practically working fluid restrictions, for instance compatibility with lubricants.

1.2 Objectives

The main objective of this work is to study a combined compression/absorption heat pump using ammonia/water as working fluid. The objectives of the present work can be listed as follows:

- Develop a matemathical model for the system.
- Design and build a test rig.
- Verify experimentally that the system can be realized within practical ranges of operation.
- Compare the model with the experimental results.
- Determine the crucial parameters for the system to operate at high performance.

1.3 Outline of thesis

The outline of this thesis is as follows.

Chapter 2 describes some characteristic features of the compression/absorption cycle. A brief overview of previous work on compression/absorption heat pumps is given.

Chapter 3 gives a description of a steady state model of the compression/absorption heat pump. The steady state model is used to find the optimum design conditions for the laboratory scale heat pump. The component models are described in detail. A second law analysis of the heat pump cycle is performed and the different losses located.

Chapter 4 provides a description of the laboratory scale test unit applied in the experiments. A detailed description of the different components used in the compression/absorption heat pump is given. The instrumentation, the data acquisition, and data reduction system of the heat pump is described. The accuracy of the measurements is also given.

Chapter 5 gives the experimental results.

Chapter 6 discusses the experimental results.

Chapter 7 gives the conclusions, and suggestions are made for future work.

2 Compression/ Absorption Heat Pumps

2.1 Characteristic features of the compression/absorption cycle

A compression/absorption cycle is a vapour compression cycle that employ working fluid mixtures consisting of a refrigerant and an absorbent instead of pure components. The refrigerant and the absorbent are characterised by a wide-boiling mixture. The evaporation of the mixtures is not complete, so the fluid leaving the desorber (comparable to the evaporator in a compression cycle) is a vapour/ liquid mixture. Vapour and liquid are separated at the desorber outlet. While the vapour proceeds to the compressor, the liquid is re- circulated to the absorber (comparable to the condenser in a compression cycle) with a solution pump in a separate liquid line. A solution heat exhanger is used for internal heat recovery to improve the cycle performance. Figure 2–1 show a schematic of the simplest compression/absorption cycle, called the Osenbrück cycle after the inventor [2] .

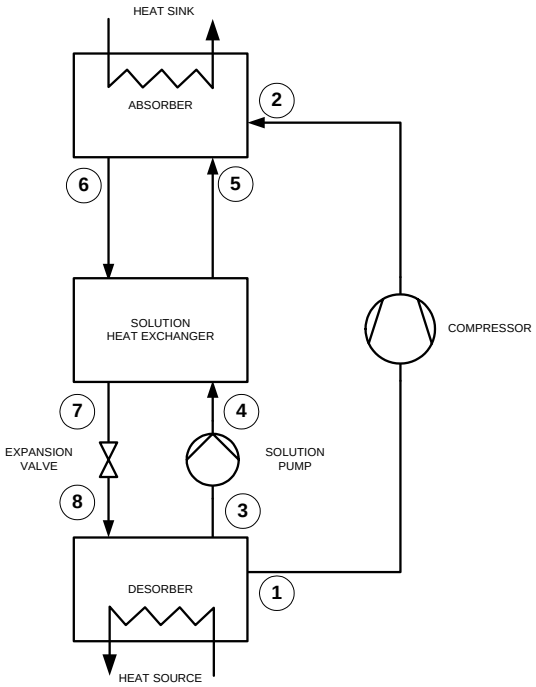

Figure 2–1: The Osenbrück cycle

The compression/absorption heat pumps provides a number of attractive advantages in comparison with conventional vapour compression heat pumps. Within given temperature limits of the heat source and heat sink there is considerable freedom of placing the solution field within the corresponding saturation pressures of the pure solute and pure solvent. This characteristic feature provides greater design flexibility than is possible for single fluid heat pumps. By a suitable choice of the concentration range external conditions can be matched to the properties of the working pair and the heat pump components. The non-isothermal behav-

iour of the desorbing and absorbing solution can be utilized to reduce heat transfer losses by counter-current heat exchange when non-isothermal heat sources and sinks are available. The compression/absorption cycle can be referenced to the Lorentz cycle, and this theoretically results in improved performance compared to the conventional vapour compression type heat pumps where the Carnot cycle is the theoretical reference cycle.

The compression/absorption heat pump exhibits some interesting possibilities when compared to conventional vapour compression type heat pumps. These can be listed as follows (Alefeld and Radermacher [1]):

1) High heat sink temperatures can be achieved.
   In ordinary vapour compression type heat pumps, the condensing pressure usually becomes higher than the design pressure of most standard refrigeration system components, even at temperatures below 100°C. Pure ammonia at 41bar pressure condenses at 79.6°C. If ammonia is absorbed into an ammonia/water solution with 10 weight-% of ammonia, the pressure is decreased to 20 bar due to the vapour pressure reduction, with a condensing temperature of 180°C. Figure 2–2 shows the solution field for the ammonia-water mixture in a log P-(-1/T) diagram. The solution circuits sketched on the diagram show how a change in the circulating concentration at constant desorber and absorber pressures can be used to achieve high heat sink temperatures. The numbers on Figure 2–2 refer to the positions indicated on Figure 2–1 .

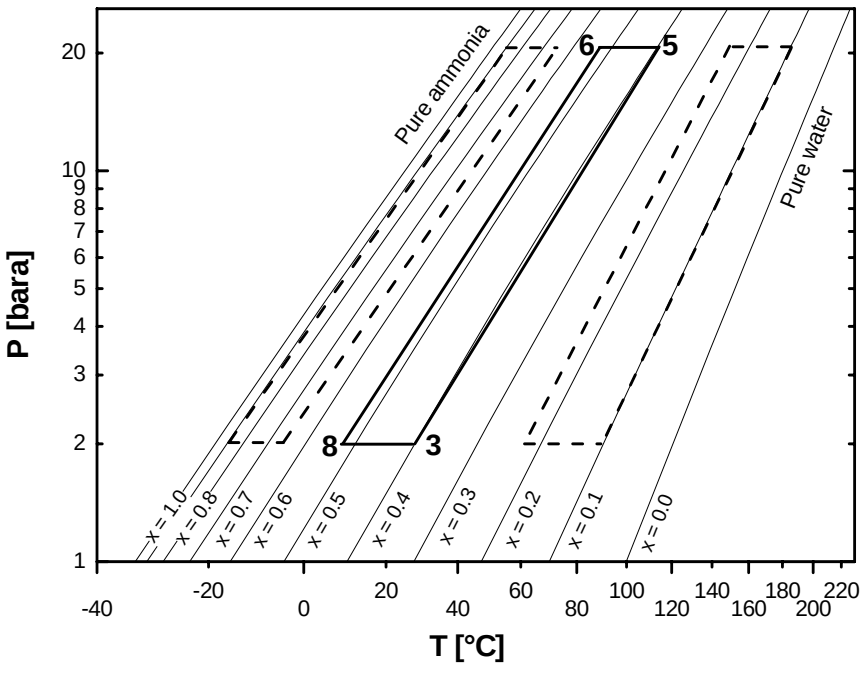

Figure 2–2: Large temperature variations and high heat sink temperatures achievable at 20 bar absorber pressure. X is the ammonia concentration of the saturated liquid solution. The numbers refer to Figure 2–1.

2) By changing the average composition of the solution circulating between the absorber and the desorber at constant temperatures, the saturation pressures can be altered. The compressor is supplied with lower or higher density vapour, resulting in a capacity change at a constant compressor rotary velocity. Figure 2–3 shows how changing the solution concentration in the solution circuit for fixed heat source and heat sink temperatures can vary the pressure at the compressor inlet.

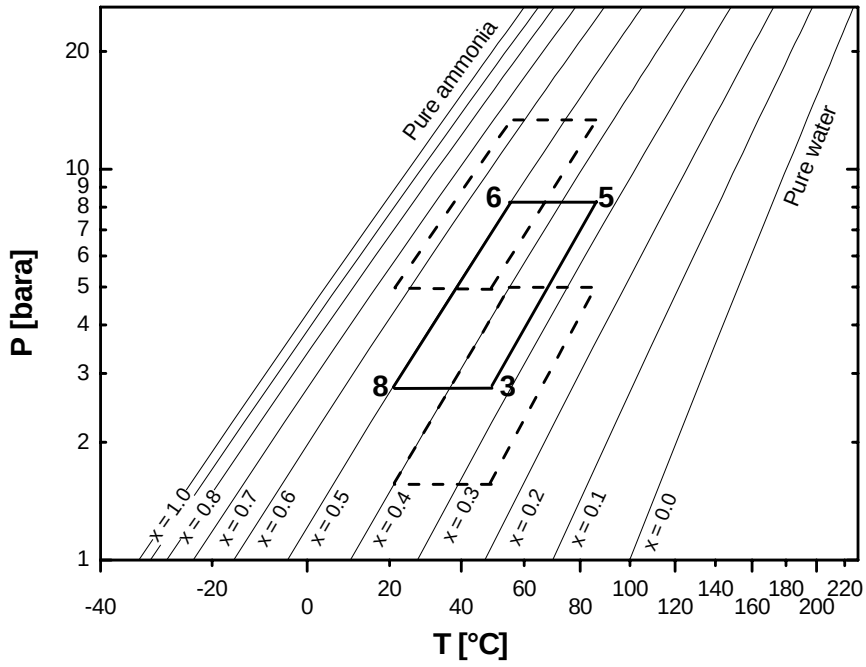

Figure 2–3: Capacity control by varying the circulating solution concentration within given temperature limits. X is the ammonia concentration of the saturated liquid solution. The numbers refer to Figure 2–1.

3) The phase change processes in the absorber and desorber are non-isothermal. The saturation temperatures vary with the composition changes of the liquid and vapour phases. The resulting temperature glides can be matched to the temperature glides of heat source and heat sink fluids, thereby reducing the losses by heat exchange. This may lead to significant improvements of the coefficient of performance of the heat pump cycle. Figure 2–4 shows how the temperature glide can be changed by a variation of the concentration change in the absorber and desorber.

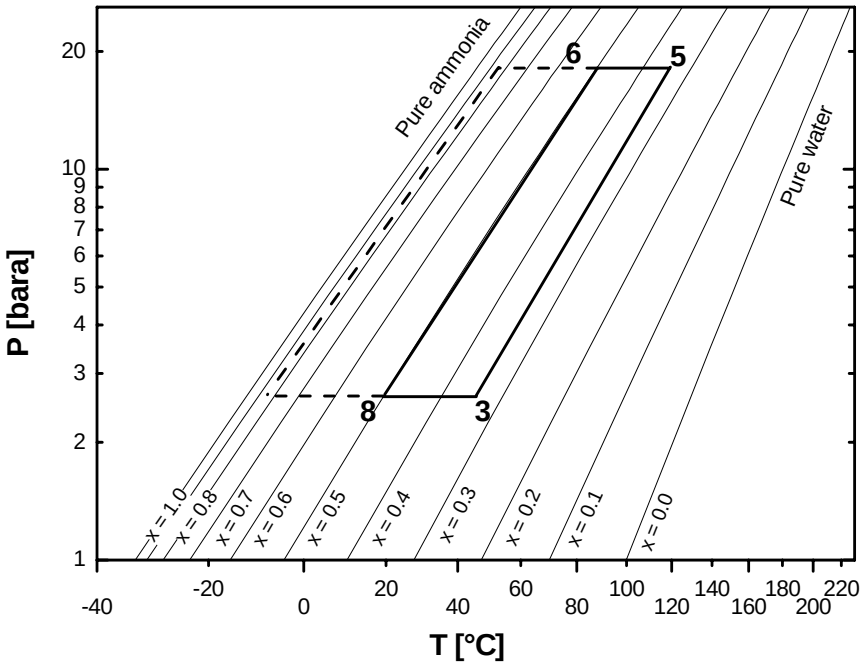

Figure 2–4: The temperature glide during the phase change processes in the desorber and absorber can be changed by alteration of the circulating solution concentration. X is the ammonia concentration of the saturated liquid solution. The numbers refer to Figure 2–1.

2.2 Previous Work

Osenbrück [2] proposed the first patent of a compression/absorption cycle in 1895. Figure 2–1 shows a schematic of the Osenbrück cycle. Then there was quiet about the subject until the early 1950s, when Altenkirch [3] [4] studied the process theoretically and indicated large energy saving potential. Apart from a few theoretical analyses no substantial effort was put into the studying of the system until 1970s when the energy crisis created renewed interest for the idea. Since then, and mainly in the recent past, these cycles have been discussed repeatedly in the literature. A historical review on this matter can be found in Morawetz [5] , Ziegler [6] , Åhlby [7] ,Groll [8] , Itard [9] and Brunin [10] .

The theoretical studies of the Osenbrück cycle made by Åhlby [7] has recently been extended by the work of Hulten [25] [26] [27] . Hulten incorporated detailed heat exhanger models for the absorber and desorber. The heat transfer coefficient on the mixture side was based on the experimental work of Berntsson [28] .

Table 2–1 show an overview of the experimental investigations on compression/absorption cycles using ammonia/water as working fluid. The table is an extension of a similar table provided by Groll [8] , and show some of the main parameters of the investigated cycles. Most of the plants were experimental laboratory plants and in addition there has been a few industrial prototypes. The experimental investigations include single-stage and two-stage cycle configurations. Both oil-lubricated and oil-free compressors have been used. Most experimenters use either vertical or horizontal shell-and-tube heat exchanger type for the absorber and desorber. Coaxial and spiral tube/tube heat exchangers are also tested. The

More recent are the works of Itard [9] and Brunin [10] . Itard studied the performance of a wet-compression type of compression/absorption heat pump, both theoretically and experimentally. The absorber and desorber were of plate-and -fin type, and a liquid-ring compressor was used. Ammonia/water was used as working fluid. The test unit heated a secondary water stream from 40°C to 53°C and cooled a secondary water stream from 44°C to 38°C. The heating coefficient of performance was reported to be 3.1. Brunin designed and built a compression/absorption heat pump utilising compact heat exchangers and an oil-cooled screw compressor. The heat sink fluid was heated from 81.7°C to 90.8°C, and the heat source fluid from 70.5°C to 63.6°C. The coefficient of performance was 2.6.

Hewitt et al [21] describes the outcome of a joint project funded by the European Commission JOULE III Non-Nuclear Energy Programme. The project looked at advanced cycles and replacement working fluids in heat pumps. PAG and PAO compressor oils were tested and found suitable for use with ammonia/water [22] . A test facility for a resorption heat pump was built [23] . The performance of the heat pump was found to be satisfactory across a pressure lift of 4.5-18bar. A max heating coefficient of performance of 3.7 was found at a circulation composition of approximately 70 weight-% ammonia, for a resorber water inlet temperature of 42°C. Modelling of the resorption cycle revealed that the relative heat exchanger area distribution between the desorber and resorber had little effect on system COP. The circulating composition was observed to change between 55 weight-% to 75 weight-% of ammonia.

Mongey et al [23] describes the test results of ammonia-water resorption cycle reported by Hewitt et al [21] in more detail. The test unit was built around a Bock AM3/233-4S semi-hermetic compressor. The compressor was lubricated with a polyglycol oil with a viscosity of 110 cSt at 40°C. Nickel-brazed plate heat exchangers were used as desorber and resorber. A thermostatic expansion valve regulated the fluid flow rate to the desorber. Mongey et al performed a series of tests to investigate the operational range of the test facility. They found a linear correlation between the vapour mass fraction at the desorber outlet and the ammonia concentration in the circulating strong solution. Significant differences were observed in the

overall heat transfer coefficient achieved in the resorber and desorber. Overall heat transfer coefficients from 5.5 to 8 kW/m^{2}K were observed in the desorber, while only 1.5kW/m^{2}K were observed in the resorber. The mixing of the vapour and liquid prior to the resorber is pointed out as the reason for the low overall heat transfer coefficient. They suggest using falling film heat exchangers to overcome this difficulty.

Ziegler [24] reviews the state of art in sorption heat pumping and cooling technologies. He states that the experimental interest in compression/absorption systems is strong but has not led to applications beyond several pilot plants, mainly due to working fluid restrictions, for instance compatibility with lubricants.

2.3 Conclusions and importance to the present work

The lubrication and sealing of the compressor seem to be the bottleneck of the compression/ absorption system. The design of the desorber and absorber is also important because the performances of the plants strongly depends on the heat transfer coefficients. Counter-current flow must be used, phase-equilibrium must be approached as closely as possible, and maldistribution of the working fluid must be avoided. The solution pump needs also careful attention as this component has to pump saturated liquid. Any pressure drop in the pump suction line would then induce cavitations.

Based on the previous work the present work then has to face the following design challenges:

- the selection of the compressor.
  For a laboratory sized test plant a reciprocating compressor would be the most suitable alternative. Both oil-lubricated and oil-free compressors has been previously tested. The oil-free compressors are expensive. For systems using an oil-lubricated compressors the proper choice of a lubrication oil and measures for oil recovery are crucial.
- the selection of the solution pump
  The working fluid is at equilibrium at the solution pump inlet giving potential problems with cavitations. The solution pump must be able to cope with small amounts of vapour in the solution.
- the design of the absorber and desorber.
  The preferred heat exchanger type for use as absorber and desorber in the experimental plants has been shell-and-tube heat exchangers, both horizontal and vertical. In the more recent publications use of compact heat exchangers are explored. Use of compact heat exchangers is favourable from economic and environmental reasons, but involves challenges with the selection of the heat transfer areas as the experience with compact heat exchangers with ammonia-water as working fluid is scarce.

Table 2–1: Experimental investigations of the compression/absorption cycle.

Author (location)	Heat Capacity [kW]	T_{source} [°C]	T_{sink} [°C]	COP_H, COP_C	Working pair	Compressor	Absorber design	Desorber design	Ref.
Bercesu et al. (Bucarest- Romania)	15	> 24	< 59	4.89 (H)	NH_3/H_2O	oil, recip, two-st	-	-	[11]
Mucic, Scheuermann (Mannheim - Germany)	160	60→50	23→78	11.3 (H)	NH_3/H_2O	oil, recip, s-st	shell/tube horisontal	shell/tube horisontal	[12]
Stokar, Trepp (Zürich - Swiss)	15	40→15	40→70	4.3 (H)	NH_3/H_2O	dry, recip, s-st	shell/tube vertical	shell/tube vertical	[13]
Malewski (Berlin - Germany)	500	35	60→80	200[1]	NH_3/H_2O	wet, screw, s-st	shell/tube horisontal	shell/tube horisontal	[14]
Mucic (Cologne - Germany)	1000	95 (const)	115 (const) steam gen.	9.1 (H)	NH_3/H_2O	dry, screw, s-st	shell/tube vertical	shell/tube vertical	[15]
Bergmann, Hivessy (Budapest - Hungary)	1000	25→5	15→85	4.35[2] (H)	NH_3/H_2O	wet, screw, s-st	shell/tube horisontal	shell/tube horisontal	[16]
Rane, Radermacher (College Park -USA)	4.2	4→-5	96→104	1.04 (C)	NH_3/H_2O	dry, recip, two-st	shell/tube vertical	shell/tube vertical	[17]
Torstensson, Nowacki (Nykoping -Sweden)	1.4	16→3	35→60	3.0 (C)	NH_3/H_2O	wet, scroll, s-st	tube/tube coaxial	tube/tube coaxial	[18]
Groll, Radermacher (College Park - USA)	2	0→-6	58→74	0.93 (C)	NH_3/H_2O	dry, recip, t-st	shell/tube vertical	shell/tube vertical	[19]
Itard (Delft-Netherlands)	13	44→38	40→53	3.1 (H)	NH_3/H_2O	wet, liquid ring, s-st	plate-fin	plate-fin	[9]

Explanations: oil = oil-lubricated, dry = oil-free, wet = lubrication done by solution, recip = reciprocating compressor, screw = screw compressor, scroll = scroll compressor, s-st = single stage, t-st = two-stage.

[1] The listed value corresponds to $COP_C \cdot \Delta T$ in Kelvin (ΔT = temperature lift)

[2] Theoretical value

Table 2–1: Experimental investigations of the compression/absorption cycle.

Author (location)	Heat Capacity [kW]	T_{source} [°C]	T_{sink} [°C]	COP_H, COP_C	Working pair	Compressor	Absorber design	Desorber design	Ref.
Brunin (Nancy - France)		70.5→63.6	81.7→90.8	2.6 (H)	NH_3/H_2O	oil, recip, s-st	compact	compact	[10]
Mongey et al. (Ulster - North Ireland)	13.5	42→57	42→27	3.7 (H)	NH_3/H_2O	oil, recip, s-st	corrugated PHE	corrugated PHE	[23]

Explanations: oil = oil-lubricated, dry = oil-free, wet = lubrication done by solution, recip = reciprocating compressor, screw = screw compressor, scroll = scroll compressor, s-st = single stage, t-st = two-stage.

[1] The listed value corresponds to $COP_C \cdot \Delta T$ in Kelvin (ΔT = temperature lift)

[2] Theoretical value

3 Design Model of the Compression/ Absorption Heat Pump

The objective of this study is to analyse the performance of a compression/ absorption heat pump. A computer model based on steady-state operation of the system has been developed. The steady-state model described by Sveine et al. [53] was used as a basis and further developed. The computer model is used as a design tool for the development of a laboratory scale compression/absorption heat pump (CAHP).

3.1 Schematic of the compression/absorption heat pump cycle

A schematic diagram of the CAHP is shown in Figure 3–1. The cycle consist of a two-stage compressor, an absorber, a desorber, a desuperheater, two solution heat exchangers, an expansion valve, a solution pump, a low-pressure liquid/vapour separator and a high-pressure liquid receiver. Heat from the heat source is transferred to the desorber, from which vapour containing the predominantly low boiling component of the working fluid mixture is generated and fed to the compressor, where it is compressed to a higher pressure in two stages. The remaining solution, weak in ammonia, is pumped to the high-pressure level and circulated into the absorber, where it absorbs the vapour delivered by the compressor. The heat of absorption is transferred to the heat sink while the resulting solution, strong in ammonia, leaving the absorber is brought into heat exchange with the weak solution in the solution heat exchanger 1 and is finally expanded down to the low pressure. At the intermediate pressure the vapour superheat is transferred to the weak ammonia solution in the solution heat exchanger 2. After the high-pressure stage the vapour superheat is transferred to the heat sink in the desuperheater. The two-phase mixture at the desorber outlet is separated in the liquid/ vapour separator.

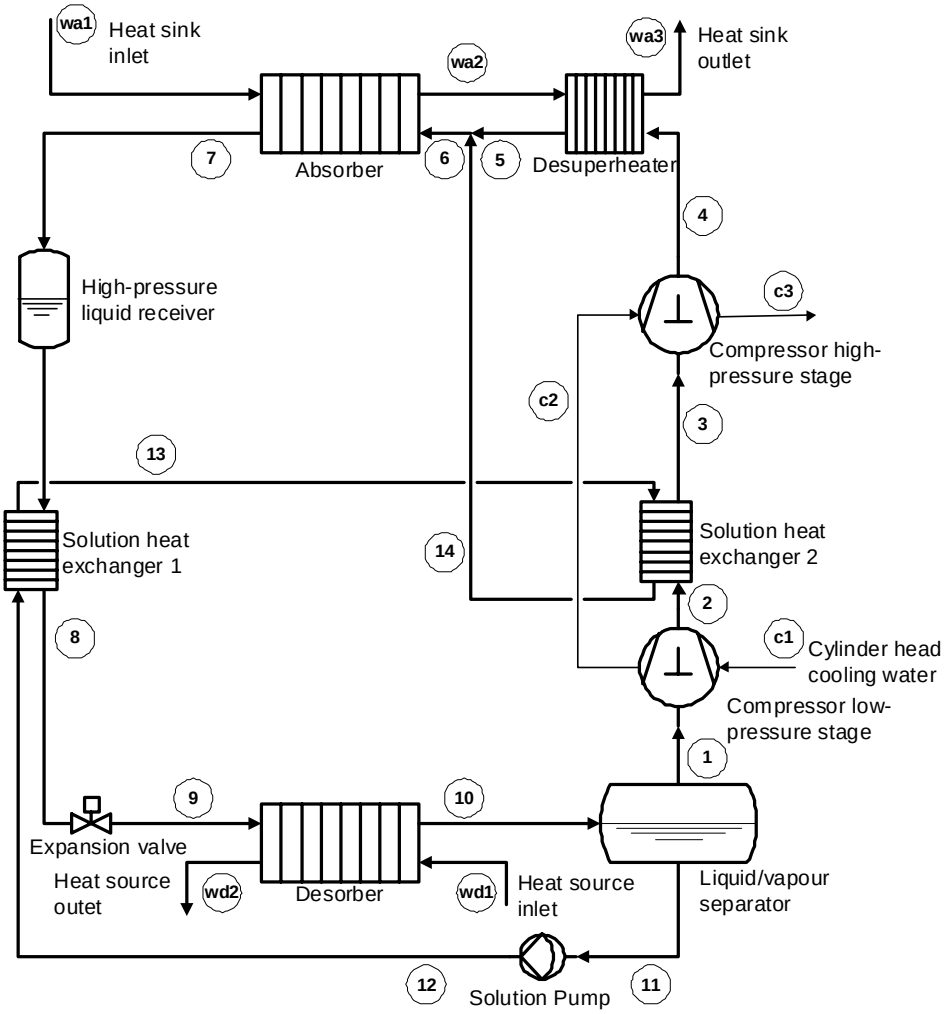

Figure 3–1: Schematic diagram of the compression/absorption heat pump cycle

3.2 Considerations when modelling compression/absorption cycles

The heat exchange processes in absorption machines are complicated by the coupled heat and mass transfer and by the properties of the binary mixture working fluids. Itard and Machielsen [20] studied the compression/absorption heat pump cycle using ammonia/water as working fluid and stress the importance of considering the non-linearity of the temperature profiles in the absorber and desorber during design. Figure 3–2 shows a normalised temperature-enthalpy diagram for ammonia/water. The diagram shows the non-linearity in the saturation temperature-enthalpy profiles for different ammonia/water mixtures. The non-linearity increases with the ammonia concentration of the circulating working fluid mixture. The solid straight line between the origin (0,0) and the coordinate point (1,1) represents a medium with constant specific heat capacity. The location of the minimum temperature difference between the working

fluid mixture and the heat sink and heat source medium is dependent of the ammonia concentration in the circulating working fluid mixture and the temperature levels.

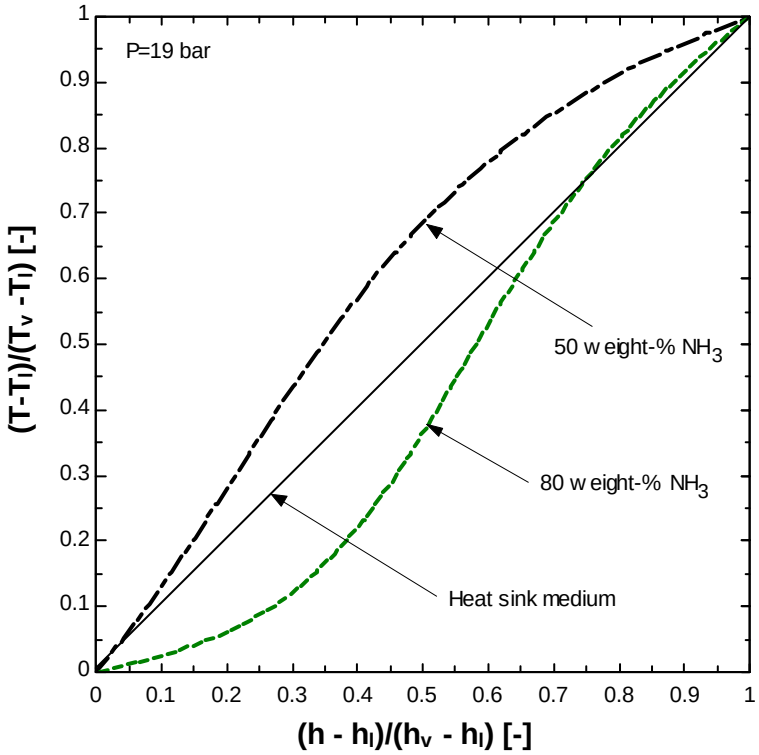

Figure 3–2: Normalised temperature-enthalpy diagram for ammonia-water showing the non-linearity of ammonia-water solutions of 50 and 80 weight-% ammonia. (T and h is the temperature and the enthalpy of the ammonia/water mixture. h_v and T_v is the enthalpy and temperature at dewpoint, h_l and T_l is the enthalpy and temperature at bubble point. The thermodynamic properties of water are predicted by the routines of Harr, Gallagher and Kell[32] . The ammonia-water properties are based on a fundamental equation of state described by Tillner-Roth and Friend [31])

The pinch point is defined as the location in the heat exchanger where the smallest temperature difference between the heat exchanging media occurs. The pinch point in the absorber is located somewhere in the middle of the heat exchange for ammonia-water mixtures with a high concentration of ammonia. In the desorber the pinch point is located at the inlet or outlet of the heat exchanger. Figure 3–3 shows the temperature versus cumulative heat transfer load characteristics for the absorber and desorber for absorption and desorption of an ammonia-water mixture of 73 weight-% of ammonia.

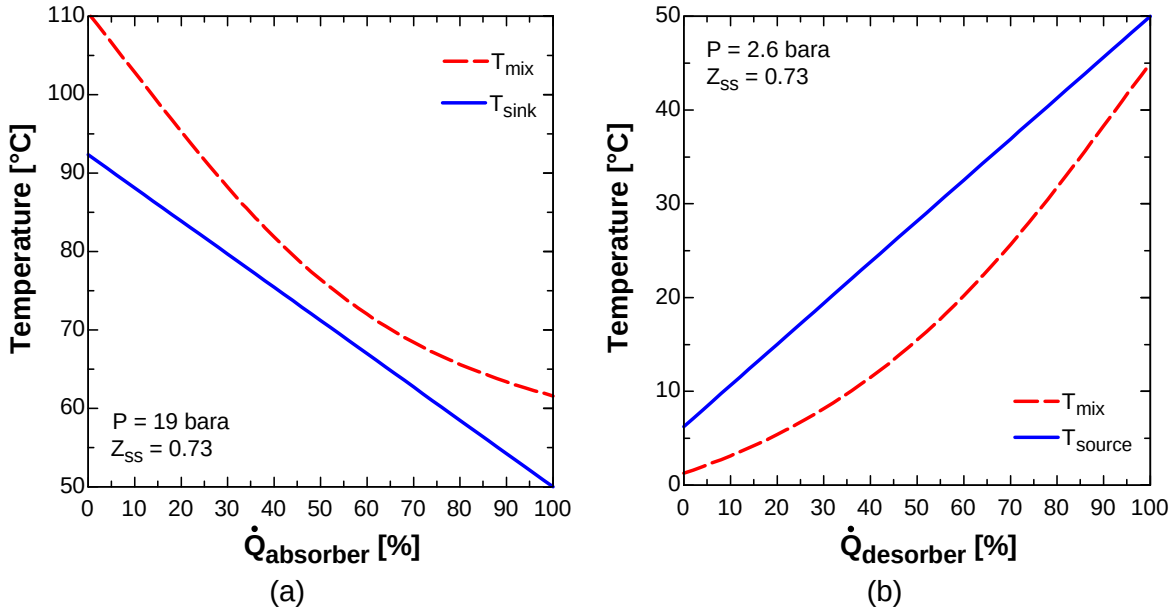

Figure 3–3: Temperature versus cumulative heat load for (a) the absorber and (b) the desorber

3.3 Design Model Description

3.3.1 General

The computer simulation model is based on fundamental physical laws such as energy and mass balances and heat transfer relations. In order to study the thermodynamic performance of the heat pump and simplify the model the following assumptions were made:

1. Pressure drops due to friction in the system are negligible.
2. The solution and the heat sink and heat source fluid flow counter-currently in the absorber and desorber. At the solution side the vapour and liquid are assumed to be in equilibrium.
3. Heat losses to the surroundings are negligible.
4. The strong solution leaving the absorber is saturated.
5. The mixing of the weak solution and vapour at the absorber inlet is adiabatic.
6. The vapour at the compressor inlet is assumed to be in thermodynamic equilibrium with the liquid in the liquid/vapour separator.
7. The solution pump efficiency is 100%.

The following balance equations can be written to each of the units in the system.

Energy balance:

$$\sum(\dot{m} \cdot h)_{in} - \sum(\dot{m} \cdot h)_{out} = 0 \tag{3.1}$$

$$\sum(\dot{m} \cdot h)_{in} + W - \sum(\dot{m} \cdot h)_{out} = 0 \tag{3.2}$$

where Equation 3.1 is for the heat exchangers and Equation 3.2 for the compressor and the solution pump.

Working fluid mass balance:

$$\sum(\dot{m} \cdot Z)_{in} - \sum(\dot{m} \cdot Z)_{out} = 0 \tag{3.3}$$

Overall mass balance:

$$\sum(\dot{m})_{in} - \sum(\dot{m})_{out} = 0 \tag{3.4}$$

where $\dot{m}$ = mass flow rate; h = enthalpy; Z= ammonia concentration by mass; W = pump or compressor work.

Heat transfer in single-phase units (desuperheater, solution heat exchanger 1 and 2):

$$\dot{Q} = \varepsilon \cdot C_{min} \cdot (T_{hot,\,in} - T_{cold,\,in}) \tag{3.5}$$

where ε is the thermal efficiency of the heat exchanger, C_{min} is the minimum heat capacity rate and $T_{hot,\,in}$, $T_{cold,\,in}$ is the inlet temperature of the hot and cold stream.

The heat transfer in the absorber and desorber are determined by specification of a minimum allowable temperature difference between the working fluid mixture and the heat sink and heat source fluid. The mass flow rate of the heat sink and heat source fluid is changed in order to fulfil the minimum temperature difference requirement.

The model inputs and outputs are summarized in Table 3–1.

Table 3–1: Model inputs and outputs

Inputs	Outputs
Solution pump mass flow rate	Refrigerant and solution loop mass flow rates
Heat sink and heat source inlet temperatures	Heat sink and heat source mass flow rates
Compressor rotational velocity	Heat transfer rates
Low and high pressure in the working fluid circuit	Thermodynamic state points
The thermal efficiencies of the solution heat exchanger 1, solution heat exchanger 2 and the desuperheater	System performance
The minimum temperature difference in the absorber and the desorber	

3.3.2 Compressor Model

The compressor to be used in the experimental plant was chosen before the model was developed. It is an oil-lubricated two-stage reciprocating type, with water-cooled cylinder heads.

The operational boundaries for the compressor are given in Table 3–2.

Table 3–2: Operational boundaries for the Sabroe TCMO 28 compressor

Parameter	Value
Minimum low-pressure side displacement volume at 900 rpm (at 33% capacity)[m^3/h]	29.2
Maximum low-pressure side displacement volume at 1460 rpm [m^3/h]	141.9
Design pressure [bara]	26

Based on discussions with the compressor manufacturer and the lubrication oil manufacturer, the maximum allowable water content in the suction side inlet was set to 2.5 weight-% and the maximum discharge temperature was set to 160°C.

The compressor characteristics can be described by the isentropic efficiency and the volumetric efficiency. The isentropic and volumetric efficiencies are obtained by polynomial functions fitted to data provided by the compressor manufacturer. The efficiencies are correlated against the pressure ratio across the compressor. The data are representative for the TCMO 28 compressor at a rotational velocity of 1460 rpm.

The isentropic efficiency is described in a polynomial form as follows:

$$\eta_{isen} = C_0 + C_1 \cdot PR \tag{3.6}$$

For the volumetric efficiency, the expression is:

$$\eta_{vol} = C_0 + C_1 \cdot PR \tag{3.7}$$

The constants C_0 and C_1 in Equation 3.6 and 3.7 was found by fitting of data provided by the compressor manufacturer by the least square method. Table 3–3 contains the constants for both efficiency functions.

Table 3–3: Constants for isentropic and volumetric efficiency functions

Constant	η_{vol}	η_{isen}
C_0	1.0539	0.9051
C_1	-0.0788	-0.0422

The vapour at the inlet of the compressor is assumed to be in thermodynamic equilibrium with the liquid in the liquid/vapour separator. The compressor inlet condition is found when the heat source temperature of a possible industrial application and the approach temperature difference at the desorber inlet is known, Equation 3.8.

$$T_{10} = T_{wd1} - \Delta T_{approach,\,desorber} \qquad (= T_1 = T_{11}) \tag{3.8}$$

When the maximum acceptable water content in the vapour at compressor inlet is given, the pressure is known and the compressors inlet condition can be found.

The compressor displacement volume, the volumetric efficiency and the vapour specific volume as showed in Equation 3.9 give the mass flow rate at the compressor inlet.

$$\dot{m}_1 = \frac{V_{disp,\,LP} \cdot \eta_{vol}}{v_1} \tag{3.9}$$

The intermediate pressure can be calculated when the temperature at the outlet of the solution heat exchanger 2 (T_3) is found. Then, the compressors isentropic outlet condition at intermediate pressure, and the real outlet condition can be decided. The internal losses in the compressor coming from the isentropic and the volumetric efficiency for both pressure stages are taken into account. Furthermore, the external cooling of the cylinder heads, $\dot{Q}_{head}$, is included.

$$h_2 - h_1 = \frac{h_{2,\,isen} - h_1}{\eta_{isen}} - \frac{\dot{Q}_{head,\,LP}}{\dot{m}_2} \tag{3.10}$$

When h_2 is known, all the other parameters at condition 2 can be calculated. The same method is used for the second stage.

3.3.3 Single-phase Heat Exchanger Models

The single-phase heat exchangers are arranged for counter-current flow. The heat exchangers are modelled based on the heat exchanger thermal efficiency. The thermal efficiency is defined as the ratio of the actual heat transfer to the maximum possible heat transfer for the given inlet conditions.

$$\varepsilon = \frac{\dot{Q}}{\dot{Q}_{max}} = \frac{\dot{Q}}{min(C_{Hot}, C_{Cold}) \cdot (T_{Hot,\,in} - T_{Cold,\,in})} \tag{3.11}$$

Equation 3.12, 3.13 and 3.14, gives the thermal efficiencies for the single-phase heat exchangers in the CAHP.

$$\varepsilon_{shx1} = \frac{\dot{Q}_{shx1}}{min(C_7, C_{12}) \cdot (T_7 - T_{12})} \tag{3.12}$$

$$\varepsilon_{shx2} = \frac{\dot{Q}_{shx2}}{min(C_2, C_{12}) \cdot (T_2 - T_{13})} \tag{3.13}$$

$$\varepsilon_{desuperheater} = \frac{\dot{Q}_{desuperheater}}{min(C_4, C_{wd2}) \cdot (T_4 - T_{wa2})} \tag{3.14}$$

where C is the product of the mass flow and the specific heat capacity of the fluid. The specific heat capacities on the mixture side are predicted as $c_p = \Delta h / (\Delta T)$.

By utilising this method the heat exchangers most critical for the cycle coefficient of performance can be found and by this make sure that they will obtain high efficiency.

3.3.4 Absorber

To avoid the problems leading to unfeasible temperature profiles in the absorber a minimum allowable temperature difference between the ammonia-water mixture and the heat sink fluid is specified. The absorber heat load is determined from the assumption of saturated liquid at the outlet. The absorber heat load is divided into 50 segments and the UA-LMTD method employed at each segment. The heat sink fluid mass flow rate is confined by the minimum allowable temperature difference requirement.

3.3.5 Desorber

The ammonia-water mixture temperature profile in the desorber will show a different trend in the concentration range investigated as indicated in Figure 3–3. The minimum temperature difference will occur at either the inlet or outlet of the heat exchanger. The approach temperature,

i.e. the temperature difference at the desorber outlet $(T_{wd1} - T_{10})$, is specified as $5°\,\mathrm{C}$. The temperature glide of heat source fluid and the ammonia-water mixture is set to be equal:

$$T_{10} - T_9 = T_{wd1} - T_{wd2} \tag{3.15}$$

The heat source fluid mass flow rate will adjust to this requirement. This implies that the minimum temperature difference will occur both at the inlet and outlet of the heat exchanger, resulting in an overall logarithmic mean temperature difference of $5°\,\mathrm{C}$. The difference between the thermodynamic average temperatures of the heat source fluid and the ammonia/water mixture will vary as the composition varies.

A separate routine calculates the temperature profiles on both sides.

3.3.6 Expansion Valve and Solution Pump Model

The expansion process is assumed to be isenthalpic. At the outlet of the expansion valve, the vapour created by flashing is in thermodynamic equilibrium with the liquid.

The solution pump is assumed to be isentropic.

3.4 Simulations

The steady-state simulation model were programmed using the Engineering Equation Solver (EES) [29] program from F-Chart Software with the thermodynamic property library for the ammonia-water mixture developed by Tillner-Roth [30] . The property library is based on a fundamental equation of state described by Tillner-Roth and Friend [31] . EES also have thermodynamic property libraries for water and for glycol/water mixtures. The properties for water from Harr, Gallagher and Kell[32] are used. The glycol/water property function is based on data from the IIR handbook on secondary refrigerants [55] .

The effect of the cylinder head water cooling is set to 5% of the shaft power based on information from York Refrigeration.

The simulations are performed with the objective of obtaining maximum heating coefficient of performance at maximum temperature lift. The temperature lift is defined as the difference between the heat sink outlet temperature (T_{wa3}) and the heat source outlet temperature (T_{wd2}). The maximum temperature lift is limited by the compressors operational boundaries.

3.4.1 Pressure Levels

The minimum advisable rotational velocity of the compressor is specified as 900 rpm to keep a sufficient lubrication oil pressure. In order to keep the size of the test plant down the rotational velocity was set to 1000 rpm and the inlet pressure was minimised. With a maximum

allowable water content in the vapour at the compressor inlet of 2.5 weight-%, a heat source inlet temperature of 50°C, and an approach temperature difference of 5°C at the desorber outlet, the compressor inlet pressure was found to be 2.6 bars.

The normal setting of the pressure safety valve is 90% of the design pressure of the system components. The maximum allowable operating pressure in the heat pump is then 23.4 bars. By varying the pressure on the high pressure side as shown in Figure 3–4, the maximum pressure was set in order not to exceed the discharge temperature limitations of the compressor, i.e. 160° C. The maximum allowable pressure was found to be 19 bars when the low-pressure is 2.6 bars.

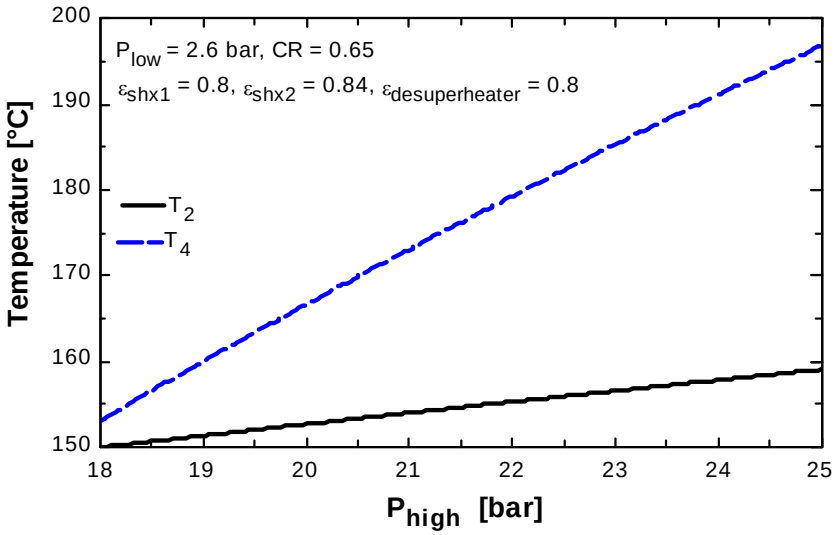

Figure 3–4: Compressor discharge temperatures versus the pressure after the high-pressure stage

3.4.2 Optimum circulation ratio

The next step is to maximise the $COP_{heating}$. The $COP_{heating}$ is defined as:

$$COP_{heating} = \frac{\dot{Q}_{absorber} + \dot{Q}_{desuperheater}}{\dot{W}_{motor} + \dot{W}_{pump}} \tag{3.16}$$

The pressure and temperature of the working fluid mixture at the desorber outlet fixes the state at the compressor inlet (1) and the solution pump inlet (11) as the vapour and liquid in the low-pressure separator is assumed to be in equilibrium. Given a temperature at the desorber outlet of 45° C, and a pressure of 2.6 bars, the ammonia concentration in the vapour and liquid in the low-pressure separator is calculated to be 98 and 34-weight-% respectively. The ammonia concentration in the working fluid mixture circulating through the absorber and desorber can be changed by varying the ratio between the mass flow of solution weak in ammonia $(\dot{m}_{11})$ and the mass flow of vapour going through the compressor $(\dot{m}_1)$.

$$CR = \frac{\dot{m}_{11}}{\dot{m}_1} \tag{3.17}$$

The mass flow of vapour going through the compressor is a function of the compressor displacement volume, the compressor volumetric efficiency, and the mixture vapour density. The mixture vapour density and the compressor displacement volume are constant. The volumetric efficiency of the low-pressure stage do not vary significantly in the calculations, hence the mass flow of vapour going through the compressor is almost constant.

The circulation ratio was varied by changing the mass flow of weak solution going through the solution pump. Figure 3–5 shows that the ammonia concentration in the circulating working fluid mixture varies from 80 weight-% to 60 weight-% as the circulation ratio is increased from 0.4 to 1.5.

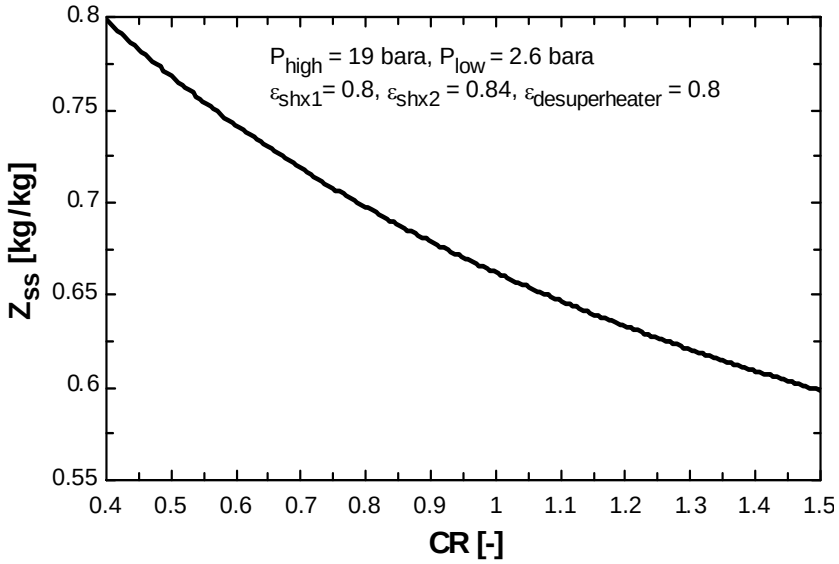

Figure 3–5: Ammonia concentration in the circulating working fluid mixture as a function of the circulation ratio.

The effect of changing the circulation ratio on the heating coefficient of performance is shown in Figure 3–6. A maximum of the $COP_{heating}$ is achieved at a circulation ratio of 0.65. The reason for this maximum of the $COP_{heating}$ can be explained by studying the heat sink load and the compressor motor effect as a function of the circulation ratio, shown in Figure 3–7. The heat sink load has a maximum at a circulation ratio of 0.82, while the motor effect decreases linearly with decreasing circulation ratio. The heat sink load is the sum of the heat loads in the absorber and the desuperheater. The absorber heat load is a function of the enthalpy difference of the mixture across the absorber and the mass flow of mixture. The enthalpy difference increases at lower circulation ratios, while the mixture mass flow decreases. The decreasing mixture mass flow causes the drop in the absorber heat load at lower circulation ratios. The maximum absorber heat load appears at a circulation ratio of 0.95. The heat load in the desuperheater increases at lower circulation ratios as the heat sink fluid mass flow rate increases and the thermal efficiency of the desuperheater is assumed con-

stant. The compressor work decreases at lower circulation ratios. The combined effect of decreased compressor work at lower circulation ratio and increased heat load in the desuperheater makes the maximum in the heating COP to occur at a circulation ratio of 0.65.

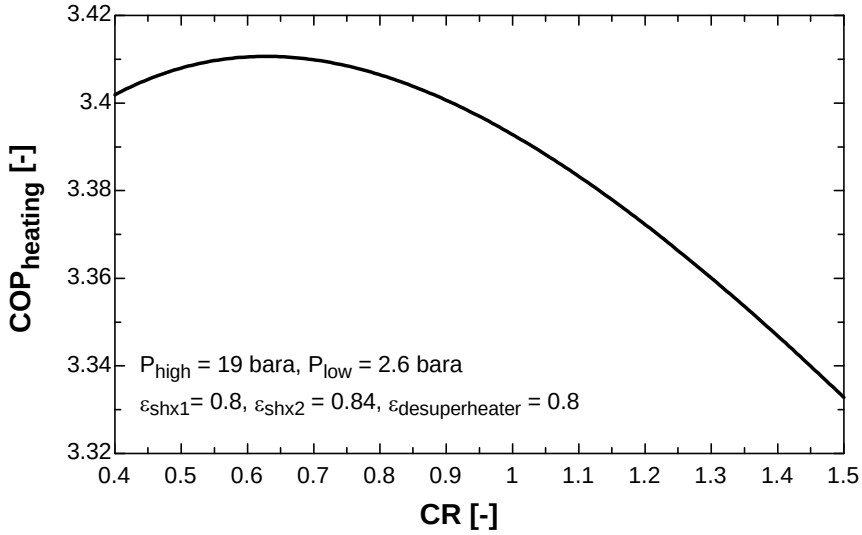

Figure 3–6: $COP_{heating}$ as a function of the circulation ratio

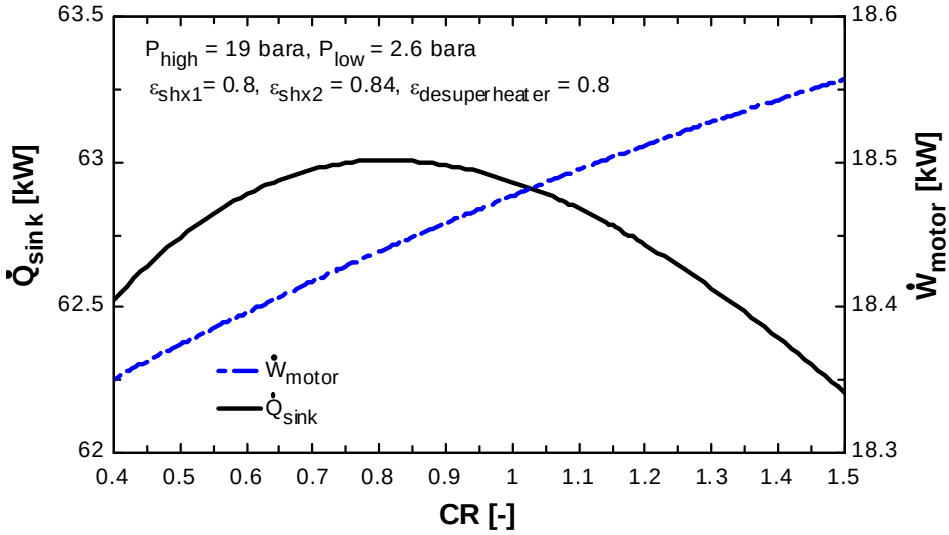

Figure 3–7: Heat sink load and compressor motor effect as a function of the circulation ratio

The maximum temperature lift is not found at the same circulation ratio as the maximum $COP_{heating}$ as shown in Figure 3–8. The maximum temperature lift is achieved at a circulation ratio of 0.95. The heat source outlet temperature is then 12°C and the heat sink outlet temperature is 108°C, giving a temperature lift of 96°C. The heat sink temperature reaches 110°C at a circulation ratio of 1.1, and remains constant at larger circulation ratios. The heat source

outlet temperature (T_{wd2}) increases linearly from 0.8° C at a circulation ratio of 0.4 to 20.8° C at a circulation ratio of 1.5.

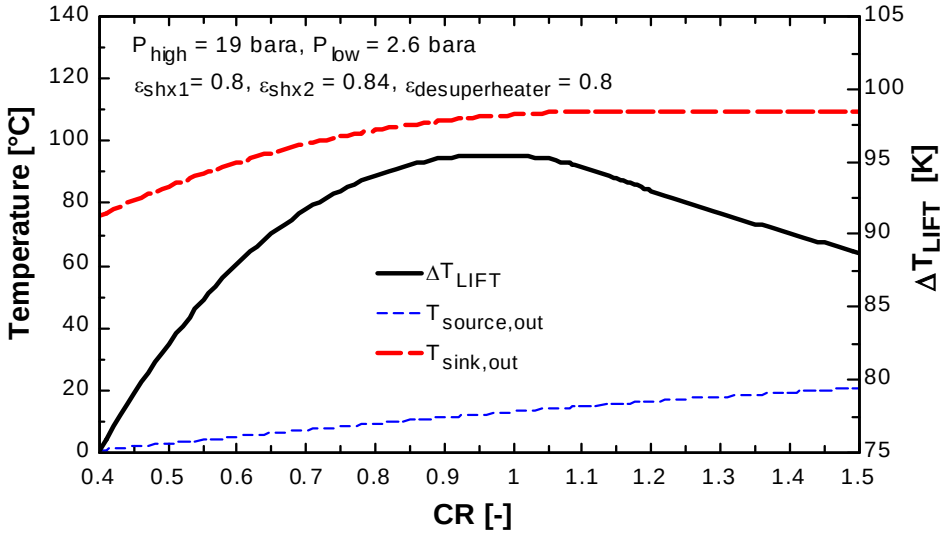

Figure 3–8: Heat sink, heat source outlet temperatures and temperature lift as a function of the circulation ratio.

3.4.3 Effect of internal heat exchange

The internal heat recovery decreases the strong solution temperature at the desorber inlet, and raises the weak solution temperature at the absorber inlet. Figure 3–9 shows the heat loads in solution heat exchanger 1 and 2 as a function of the circulation ratio.The heat load in solution heat exchanger 1 increases from 0.7kW at circulation ratio of 0.4 to 6.0kW at a circulation ratio of 1.5. The heat load in solution heat exchanger 2 decreases from 7.38kW at a circulation ratio of 0.4, to 6.5kW at a circulation ratio of 1.5.

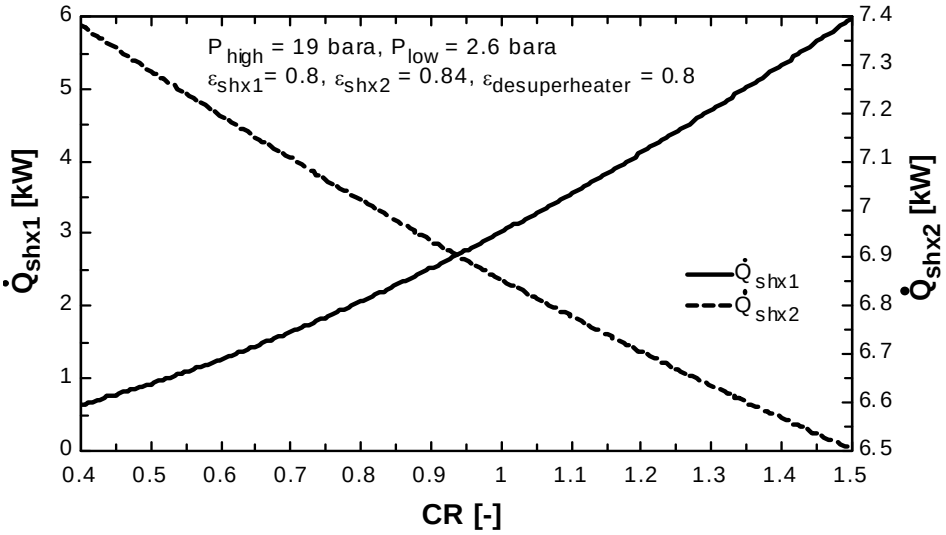

Figure 3–9: Heat loads in solution heat exchanger 1 and 2 as a function of the circulation ratio

Solution heat exchanger 2 is the most important of the internal heat exchangers. In the case of two-stage compression, it lowers the suction temperature at the high-pressure stage thereby decreasing the compressor work, and at the same time it raises the weak solution temperature near to saturation. Figure 3–10 shows the heating COP and the vapour discharge temperatures at the compressor low-pressure and high-pressure stage as a function of the thermal efficiency of solution heat exchanger 2. As the thermal efficiency of the solution heat exchanger 2 increases, the compressor discharge temperatures decrease substantially. The thermal efficiency of solution heat exchanger 1 and the circulation ratio was kept constant at 0.80 and 0.65 respectively during the calculations. The compressed gas is cooled down to the dew point temperature at a thermal efficiency of solution heat exchanger 2 of 0.87.

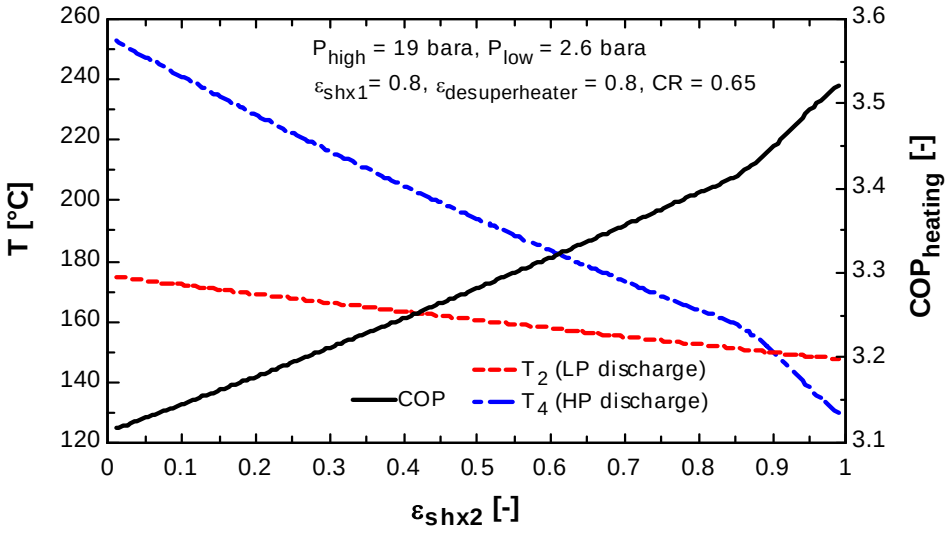

Figure 3–10: The effect of the thermal efficiency of solution heat exchanger 2 on the heating COP and compressor vapour discharge temperatures.

The importance of solution heat exchanger 1 is less than solution heat exchanger 2. Solution heat exchanger 1 affects the inlet state at the desorber; thereby it has the possibility to increase the desorber heat load. The effect of solution exchanger 1 increase at higher circulation ratios, but it is of less importance at low circulation ratios.

3.5 Second Law Analysis of the cycle

The second law analysis helps to understand and locate the irreversibilities associated with inefficient processes. Using the concept of entropy generation, the entropy losses during a process can be expressed as Equation 3.18.

$$S_{gen} = S_2 - S_1 - \int_1^2 \frac{\delta Q}{T} \tag{3.18}$$

S_{gen} is positive for real processes and zero for reversible ones, but never negative.

A generalization of the second law can be written for a control volume (open system) as:

$$S_{gen} = \frac{dS}{dt} + \sum \dot{m}_{exit} \cdot s_{exit} - \sum \dot{m}_{inlet} \cdot s_{inlet} - \sum_i \frac{\dot{Q}_i}{T_i} \geq 0 \qquad (3.19)$$

where the temperature T_i of the heat reservoir at the portion i of the control volume is either uniform for isothermal heat transfer processes or is the thermodynamic average temperature for variable temperature heat transfer processes.

The control volume used in the analysis is shown in Figure 3–11.

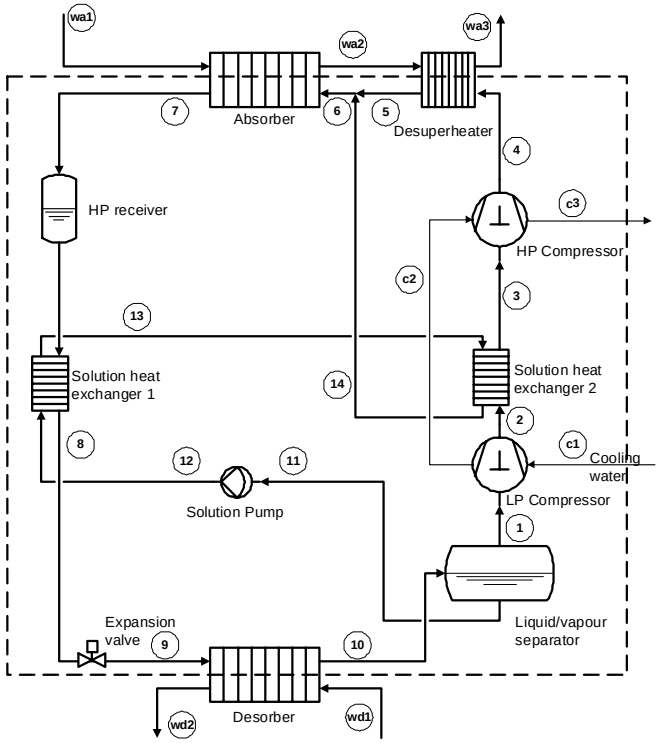

Figure 3–11: Control volume for 2.law analysis

The total entropy production of the heat pump system is the sum of the entropy production at the heat sink, the entropy production at the compressor cooling water jacket and the entropy production at the heat source.

$$S_{gen} = \frac{\dot{Q}_{absorber}}{T_{avg,\,absorber}} + \frac{\dot{Q}_{desuperheater}}{T_{avg,\,desuperheater}} + \frac{\dot{Q}_{cooling}}{T_{avg,\,cooling}} - \frac{\dot{Q}_{desorber}}{T_{avg,\,des}} \qquad (3.20)$$

The total entropy production of the heat pump is the sum of the entropy production at the internal processes:

$$S_{gen} = \sum_{i=1}^{8} S_{gen,\,i} \tag{3.21}$$

where $\sum S_{gen,\,i}$ represents the following irreversible processes:

Compression between 1 and 4:

$$S_{gen,\,1} = \dot{m}_1 \cdot (s_2 - s_1) + \dot{m}_3 \cdot (s_4 - s_3) + \frac{\dot{Q}_{cooling}}{T_{avg,\,cooling}} \tag{3.22}$$

Heat transfer in the desuperheater:

$$S_{gen,\,2} = \dot{m}_4 \cdot (s_5 - s_4) + \frac{\dot{Q}_{desuperheater}}{T_{avg,\,desuperheater}} \tag{3.23}$$

Mixing of streams 5 and 14:

$$S_{gen,\,3} = \dot{m}_6 \cdot s_6 - \dot{m}_5 \cdot s_5 - \dot{m}_{14} \cdot s_{14} \tag{3.24}$$

Heat transfer in the absorber:

$$S_{gen,\,4} = \dot{m}_6 \cdot (s_7 - s_6) + \frac{\dot{Q}_{absorber}}{T_{avg,\,abs}} \tag{3.25}$$

Heat transfer in the solution heat exchanger 1:

$$S_{gen,\,5} = \dot{m}_7 \cdot (s_8 - s_7) + \dot{m}_{12} \cdot (s_{13} - s_{12}) \tag{3.26}$$

Throttling between 8 and 9:

$$S_{gen,\,6} = \dot{m}_8 \cdot (s_9 - s_8) \tag{3.27}$$

Heat transfer in the desorber:

$$S_{gen,\,7} = \dot{m}_9 \cdot (s_{10} - s_9) - \frac{\dot{Q}_{desorber}}{T_{avg,\,des}} \tag{3.28}$$

Heat transfer in the solution heat exchanger 2:

$$S_{gen,\,8} = \dot{m}_2 \cdot (s_3 - s_2) + \dot{m}_{13} \cdot (s_{14} - s_{13}) \tag{3.29}$$

Figure 3–12 shows the irreversibility distribution in the compression/absorption heat pump cycle. The main contributor to the losses in the heat pump cycle is the compressor, which

accounts for 28% to 30% of the total system loss. The compressor losses decreases towards lower circulation ratios. Also important is the irreversibility associated with the expansion process contributing with 19% to 24% of the total system loss. The irreversibility in the expansion valve is caused by two main reasons: the pressure drop across the valve and the degree of subcooling of the solution at the inlet of the valve. The lower the pressure drop and the larger the degree of subcooling, the lower the irreversibilities will be. The pressure drop is constant here, so the variations in the irreversibilities caused by the expansion valve are due to changing degree of subcooling of the ammonia-water mixture at the valve inlet. The losses associated with the heat transferred in the absorber and desorber is dependant on the mean temperature difference between the ammonia-water mixture and the heat sink and heat source fluid. The heat transfer losses in the absorber have a minimum at a circulation ratio of 0.85. The desorber losses decrease with increasing circulation ratio as the difference in the thermodynamic average temperatures of the solution and heat source fluid decrease with increasing circulation ratio. The losses in the mixing process and in the solution heat exchanger 1 are minor compared to the other losses, but become larger with increasing circulation ratio. The losses in solution heat exchanger 2 decreases when the circulation ratio decreases. The irreversibility in the desuperheater increases when the circulation ratio decreases as the heat sink fluid mass flow increases, causing a larger driving temperature difference

.

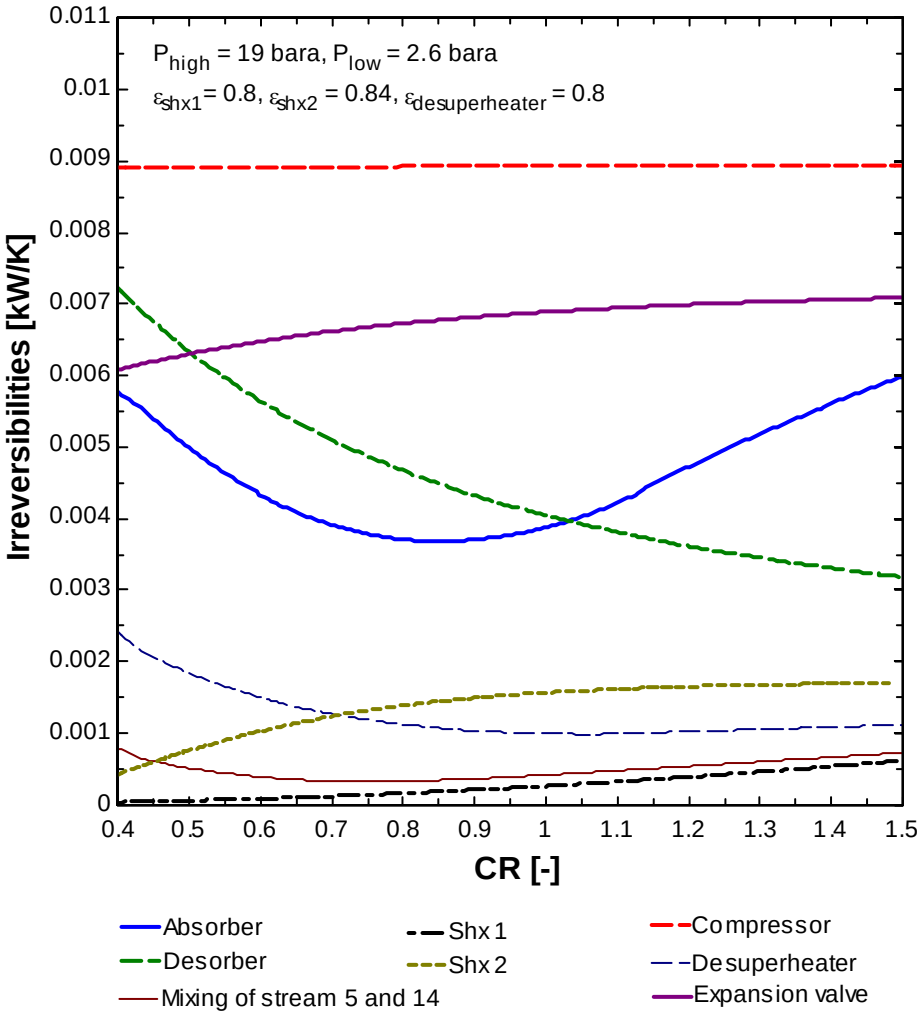

Figure 3–12: Irreversibility distribution as a function of the circulation ratio

The second law efficiency for the compression/absorption heat pump is calculated according to Equation 3.30.

$$\eta_{II} = \frac{COP}{COP_{rev}} \tag{3.30}$$

where

$$COP_{rev} = \frac{T_{avg,\,sink}}{T_{avg,\,sink} - T_{avg,\,source}} \tag{3.31}$$

where $T_{avg,\,sink}$ and $T_{avg,\,source}$ are the thermodynamic average temperature for the heat sink and heat source fluid respectively.

The thermodynamic average temperature for a system can be found from the following $T \cdot dS$ equation [33] .

$$T \cdot ds = dh - v \cdot dp \tag{3.32}$$

For a process at constant pressure this reduces to:

$$T = \frac{dh}{ds} \tag{3.33}$$

This can be written as:

$$T = \frac{\int_1^2 c_p dT}{\int_1^2 \frac{c_p dT}{T}} \tag{3.34}$$

If constant specific heat is assumed for the fluid, Equation 3.34 can be written as:

$$T = \frac{T_2 - T_1}{\ln\left(\frac{T_2}{T_1}\right)} \tag{3.35}$$

The thermodynamic average temperature of the heat sink and of the heat source fluid can then be calculated as:

$$T_{avg,\,\mathrm{sin}k} = \frac{T_{wa3} - T_{wa1}}{\ln\left(\frac{T_{wa3}}{T_{wa1}}\right)} \tag{3.36}$$

and

$$T_{avg,\,source} = \frac{T_{wd2} - T_{wd1}}{\ln\left(\frac{T_{wd2}}{T_{wd1}}\right)} \tag{3.37}$$

The variations of the $COP_{heating}$ and second law efficiency with the circulation ratio are plotted in Figure 3–13. A maximum second law efficiency of 0.46 is seen at a circulation ratio of 0.91, while a maximum $COP_{heating}$ occurs at a circulation ratio of 0.65. The curves have different shapes because the heat sink and heat source fluid thermodynamic average temperature

is constantly changing. The compression/absorption heat pump uses energy more efficiently at a circulation ratio of 0.91

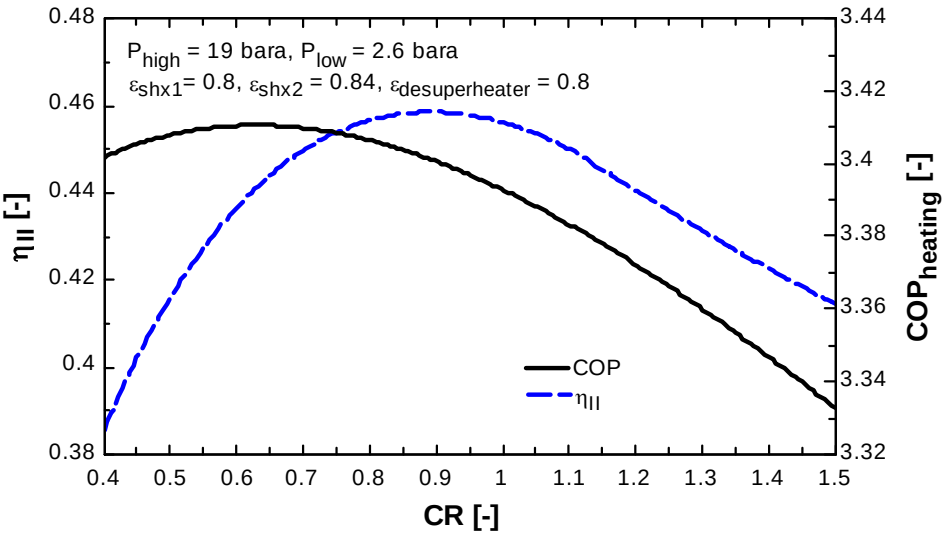

Figure 3–13: Variations in the second-law efficiency and $COP_{heating}$ with circulation ratio

Table 3–4 show the irreversibility distribution in the compressor/absorption heat pump components at a circulation ratio of 0.65.

Table 3–4: Irreversibility distribution in the cycle components at a circulation ratio of 0.65.

Component	Irreversibility [%]
Compressor	32.0
Desorber	19.2
Absorber	14.7
Expansion valve	23.5
Solution heat exchanger 1	0.4
Solution heat exchanger 2	4.1
Solution pump	0
Mixing 5-14	1.3
η_{II}	0.444

3.6 Design data

The laboratory compression/absorption heat pump design data are obtained from the simulation model. Table 3–5 shows the input data to the model:

Table 3–5: Input data to the model

Parameter	Value
Heat sink inlet temperature, T_{wa1} [^{o}C]	50
Heat source inlet temperature, T_{wd1} [^{o}C]	50
Approach temperature difference at desorber inlet, [^{o}C]	5
Minimum temperature difference in absorber, [^{o}C]	5
Thermal efficiency of solution heat exchanger 1 [-]	0.8
Thermal efficiency of solution heat exchanger 2 [-]	0.84
Thermal efficiency of desuperheater [-]	0.8
Pressure in working fluid cycle high-pressure side[bara]	19
Pressure in working fluid cycle low-pressure side[bara]	2.6
Solution pump mass flow rate [kg/s]	0.0246
Compressor rotational velocity [rpm]	1000

Table 3–6 show the resulting operating conditions of the heat pump at design point. The state points refer to Figure 3–1.

Table 3–6: Operating conditions at design point

State point	m [i] [kg/s]	T[i] [^{o}C]	P[i] [bara]	Qu[i] [kg/kg]	Z[i] [kg/kg]	h[i] [kJ/kg]
1	0.0378	45	2.6	1	0.98	1741.4
2	0.0378	151.3	7.82	1	0.98	1972.0
3	0.0378	73.1	7.82	1	0.98	1783.3
4	0.0378	160.0	19.0	1	0.98	1969.0
5	0.0378	105.9	19.0	1	0.98	1826.3
6	0.0624	110.4	19.0	0.603	0.73	1281.1
7	0.0624	61.6	19.0	0	0.73	358.8
8	0.0624	56.9	19.0	0	0.73	335.6
9	0.0624	1.3	2.6	0.200	0.73	335.6
10	0.0624	45.0	2.6	0.606	0.73	1091.0
11	0.0246	45.0	2.6	0	0.344	90.4
12	0.0246	45.1	19.0	0	0.344	92.4

Table 3–6: Operating conditions at design point

State point	m [i] [kg/s]	T[i] [^oC]	P[i] [bara]	Qu[i] [kg/kg]	Z[i] [kg/kg]	h[i] [kJ/kg]
13	0.0246	58.2	19.0	0	0.344	151.3
14	0.0246	120.2	19.0	0	0.344	442.3
wa1	0.3244	50.0	3	0	-	209.6
wa2	0.3244	92.3	3	0	-	386.9
wa3	0.3244	96.3	3	0	-	403.6
wd1	0.2639	50.0	-	0	-	-
wd2	0.2639	6.3	-	0	-	-

$COP_{heating}$ = 3.41	$Q_{absorber}$ = 57.5 kW	Q_{shx1} = 1.45 kW
$W_{compressor}$ =16.6 kW	$Q_{desorber}$ = 47.1 kW	Q_{Shx2} =7.15 kW
W_{motor} = 18.4 kW	$Q_{desuperheater}$ = 5.4 kW	V_{pump}= 1.7 l/min
W_{pump} = 0.047 kW	$RPM_{compressor}$ = 1000	UA_{shx1} = 0.215 kW/K
$UA_{absorber}$ = 7.563 kW/K	$UA_{desorber}$ = 5.097 kW/K	UA_{shx2} = 0.298 kW/K
$UA_{desuperheater}$ = 0.161 kW/K		

3.7 Models for the design of absorber and desorber

Two general methods are often used as basis for prediction of the heat transfer coefficients in binary mixtures, the method from Colburn and Drew [45] , and the method from Silver [34] . The method from Colburn and Drew is complex and requires more information than the simpler method from Silver. The latter is used here, and is explained in detail in Appendix B. Sardesai et al [39] studied the application of the Silver method on both condensation and boiling, and suggested to use the Silver method for both condensation and boiling.

Using the Silver method the heat transfer coefficient for condensation on the ammonia-water mixture side can be predicted with Equation 3.38:

$$\alpha_{eff,\,cond} = \left[\frac{1}{\alpha_{film,\,cond}} + \frac{Z_S}{\alpha_g \cdot C_f \cdot \theta}\right]^{-1} \tag{3.38}$$

where $\alpha_{film,\,cond}$ is the two-phase film heat transfer coefficient, Z_S is a factor that considers the sensible heat of the condensing vapour, C_f is a correction factor for two-phase enhancement at the liquid-vapour interface, and θ is a correction factor for the effect of condensation mass flux on the vapour-phase heat transfer coefficient.

The condensation two-phase film heat transfer coefficient, $\alpha_{film,\,cond}$, can be predicted using the Boyko and Kruzhilin [37] correlation. Panchal [38] used the Boyko and Kruzhilin correlation to predict the overall condensation heat transfer coefficient in a plate heat exchanger with ammonia as working fluid. The overall heat transfer coefficient was predicted with an average uncertainty of about 10%. The test plate heat exchanger had a corrugation angle of 60° and an equivalent diameter of 7.6mm. The Boyko and Kruzhilin correlation is given in Equation 3.39. Refer to Appendix C for a description of the correlation.

$$\alpha_{film,\,cond} = \alpha_{lo} \cdot \left[1 + \left(\frac{\rho_l - \rho_g}{\rho_g}\right) \cdot Qu_g\right]^{\frac{1}{2}} \tag{3.39}$$

where α_{lo} is the single-phase heat transfer coefficient assuming all fluid flowing as liquid, Qu_g is the vapour mass fraction and ρ_l and ρ_g is the density of the liquid and vapour phase respectively.

The Z factor is given as the ratio between the sensible heat flux to the vapour-liquid interface to the total heat flux through the condensate liquid film.

$$Z = \frac{\dot{q}_g}{\dot{q}} = Qu_g \cdot c_{p,\,g} \cdot \frac{dT}{dh} \tag{3.40}$$

where Qu_g is the vapour mass fraction, $c_{p,\,g}$ is the vapour specific heat capacity, and $\frac{dT}{dh}$ is the gradient of the equilibrium condensation curve.

The effect of the condensation mass flux is to distort the temperature profile in such a way that the sensible heat flux, $\dot{q}_g$, is reduced. θ is given by Equation 3.41:

$$\theta = \frac{A_a}{e^{A_a} - 1} \tag{3.41}$$

where the parameter, A_a, is calculated from the condensation mass flux at the vapour-liquid interface:

$$A_a = \frac{M_{cond} \cdot c_{p,\,g}}{\alpha_g} \tag{3.42}$$

θ has a value between 0 and 1. A value of 1 means that there is no mass transfer resistance in the vapour-phase.

The C_f factor is calculated using the method suggested by Price and Bell [36] . They calculated the enhancement of the vapour-phase heat transfer coefficient using Equation 3.43.

$$C_f = \left[\frac{(dP/dL)_{f,\,tp}}{(dP/dL)_{f,\,v}}\right]^{0.445} \tag{3.43}$$

C_f has a minimum value of 1.0 for a smooth interface.

The frictional pressure drop gradient for two-phase flow is calculated by the Lockhart-Martinelli correlation outlined in Appendix D. The frictional pressure drop gradient in the vapour phase is calculated using single-phase frictional pressure drop correlations provided by Alfa-Laval AS, given in Equation 3.51.

The heat transfer coefficient in the liquid phase α_{lo}, and in the vapour phase, α_g, is predicted with correlations for single-phase heat transfer provided by Alfa-Laval Thermal AB. The single-phase heat transfer correlations are empirical Nusselt number correlations with the following form:

$$Nu = f(Re) \cdot f(Pr) \cdot \left(\frac{\mu_{bulk}}{\mu_{wall}}\right)^{N_1} \tag{3.44}$$

where *Re* is the Reynolds number, *Pr* is the Prandtl number, μ_{bulk} and μ_{wall} are the fluid bulk viscosity and the fluid viscosity near the wall. The Reynolds number function *f(Re),* the Prandtl number function *f(Pr)* and the exponent N_1 are proprietary to Alfa-Laval AS.

The boiling heat transfer coefficient can be predicted using an adapted Silver method as shown in Equation 3.45.

$$\alpha_{eff,\,boiling} = \left[\frac{1}{\alpha_{film,\,boiling}} + \frac{Z_S}{\alpha_g \cdot C_f}\right]^{-1} \tag{3.45}$$

Predictive methods for boiling of single component fluids form the basis for development of methods for mixtures. Thome [40] and Stephan [41] review the state of the art for boiling of new refrigerants and refrigerant mixtures. For zeotropic mixtures Thome recommends using an accurate, general type of pure refrigerant correlation that is modified to include the mixture mass diffusion effect. Stephan recommends the correlation developed by Steiner and Taborek[43] for mixtures. He shows that it applies to mixtures by comparison of predicted values from the correlation to the experimental values from Jung and Radermacher [42] .

Steiner and Taborek[43] developed a new correlation for flow boiling heat transfer in vertical tubes. The correlation was tested on the University of Karlsruhe data bank containing 13000 data points, and results superior to previous correlations was demonstrated. The two-phase

heat transfer coefficient is calculated with an asymptotic addition of the nucleate boiling and convective boiling components as shown in Equation 3.46.

$$\alpha_{film,\,boiling} = [(\alpha_{nb,\,o} \cdot F_{nbf} \cdot S_{mix})^n + (\alpha_{lo} \cdot F_{tp})^n]^{\frac{1}{n}} \tag{3.46}$$

where $\alpha_{nb,\,o}$ is the local nucleate flow boiling coefficient at a normalised conditions of heat flux and reduced pressure, F_{nbf} is a correction factor to $\alpha_{nb,\,o}$ which compensates for the difference between pool and flow boiling, α_{lo} is the local liquid-phase forced convection coefficient based on the total flow as liquid (The correlation given by Alfa Laval AS is used), and F_{tp} is a two-phase multiplier that accounts for the enhancement of convection during two-phase flow. A value of the exponent, n, equal to 3 is recommended by Steiner and Taborek.

As the model is developed for single-component boiling, a suppression factor S_{mix} is added to the nucleate boiling term. S_{mix} accounts for the reduction in nucleate boiling heat transfer when using mixtures. The suppression factor given by Thome and Shakir [46] is used:

$$S_{mix} = \left[1 + \frac{\alpha_i}{\dot{q}} \cdot (T_{dew} - T_{bub}) \cdot \left(1 - \exp\left(\frac{-B_0 \cdot \dot{q}}{\rho_l \cdot \Delta h_{lg} \cdot \beta_f}\right)\right)\right]^{-1} \tag{3.47}$$

where α_i is the ideal heat transfer coefficient calculated with an appropriate pure refrigerant correlation utilizing the mixture physical properties, B_0 is a scaling factor assumed to be 1.0 (i.e. assuming all heat transferred to the bubble interface is converted to latent heat) and β_f is the liquid-phase mass transfer coefficient and is assumed to be 0.0003 m/s as recommended by Thome and Shakir.

The nucleate boiling term is significant only if the actual heat flux is larger than the heat flux for onset of nucleate boiling. Steiner and Taborek [43] recommends the following equation for the calculation of the heat flux for onset of nucleate boiling:

$$\dot{q}_{onb} = \frac{2 \cdot \sigma \cdot T_{sat} \cdot \alpha_{lo}}{r_{cr} \cdot \rho_g \cdot \Delta h_{lg}} \tag{3.48}$$

where σ is the surface tension, T_{sat} is the saturation temperature in Kelvin, r_{cr} is the critical radius (a value of 0.3×10^{-6} m is recommended for usual drawn tube material), ρ_g is vapour density, and Δh_{lg} is the latent heat of evaporation.

It is important to take the pressure drop into consideration during design of plate heat exchangers, particularly for two-phase flow applications. The narrow channel spacing in the plate heat exchangers gives high frictional pressure drops. The total pressure drop in a plate heat exchanger can be divided into the following components:

- pressure losses in the inlet/outlet manifold including the losses in the channel entrance and exit,
- pressure loss in the connecting pipe,
- frictional pressure loss in the corrugated channels,
- gravitational pressure drop, and
- accelerational pressure drop.

The total pressure loss can then be expressed as:

$$\Delta P_{total} = \Delta P_{fric} + \Delta P_{grav} + \Delta P_{acc} + \Delta P_{manifold} + \Delta P_{piping} \tag{3.49}$$

The single-phase frictional pressure drop is calculated by:

$$\Delta P_{fric} = 2 \cdot f \cdot \frac{\Delta L}{D_h} \cdot \frac{\dot{G}^2}{\rho} \cdot \left(\frac{\mu_{wall}}{\mu_{bulk}}\right)^{N_2} \tag{3.50}$$

where f is the Fanning friction factor, $\dot{G}$ is the mass velocity, ΔL is the incremental length, D_h is the channel hydraulic diameter, and ρ is the fluid density. The Fanning friction factor is predicted with a frictional pressure drop correlation provided by Alfa-Laval Thermal AB, given as:

$$f = c_1 \cdot Re^{c_2} \tag{3.51}$$

where the parameters c_1 and c_2 depend on the local Reynolds number. The exponent N_2 depend on the local Reynolds number of the flow. c_1, c_2 and are N_2 proprietary to Alfa-Laval AS.

The two-phase frictional pressure drop is predicted using the Lockhart-Martinelli method with a Chisholm parameter C_c equal to 8 as suggested by Thonon et al [47] . The Lockhart-Martinelli method is described in Appendix D

The gravitational pressure drop is calculated by:

$$\Delta P_{grav} = \pm \rho_{tp} \cdot g \cdot \Delta L \tag{3.52}$$

where ρ_{tp} is the two-phase density assuming homogenous flow and g is the gravitational acceleration. The gravitational pressure drop is positive or negative dependent on the flow direction (upwards or downwards).

The acceleration pressure drop is calculated by:

$$\Delta P_{acc} = \frac{1}{2} \cdot \left(\frac{1}{\rho_{tp,\,out}} - \frac{1}{\rho_{tp,\,in}} \right) \cdot \dot{G}^2 \tag{3.53}$$

where $\rho_{tp,\,in}$ and $\rho_{tp,\,out}$ is two-phase density of the mixture at the inlet and outlet of the segment assuming homogenous flow.

The losses in the connecting piping and the manifolds are not significant relative to the frictional pressure drop and have been excluded in the calculations.

The described methods for calculation of the heat transfer and pressure drop on the mixture side are implemented into a mathematical design model. The heat transfer on the water side of the heat exchangers is calculated using the single-phase correlations for heat transfer given by Alfa Laval AS. The pressure drop on the water side of the heat exchangers is neglected. The absorber and desorber heat loads are divided into 50 segments and the UA-LMTD method were used at each segment. The design parameters for the absorber and desorber are listed in Table 3–6.

4 Laboratory Scale Prototype of Compression/Absorption Heat Pump

The purpose of erecting a prototype is to study experimentally the characteristics of the combined compression/absorption heat pump (CAHP) cycle using ammonia/water as working fluid. The laboratory compression/absorption heat pump test rig is described in this chapter. First the choice of the design characteristics will be explained and then the different components of the heat pump will be described, particular attention being paid to the absorber and desorber units. The measurement and control system will also be presented.

4.1 Process description

Figure 4–1 shows the layout of the laboratory compression/absorption heat pump test rig. The test rig comprises three loops:

- a glycol/water circuit as heat source,
- a working fluid circuit, and
- a water circuit as heat sink.

The glycol/water circuit consists of a liquid receiver heated by two electric heaters, an expansion tank and a circulation pump. Hot glycol/water is pumped from the receiver through the desorber were heat is dissipated to the ammonia/water mixture. The glycol/water mixture then goes through the shunt heat exchanger were heat is re-circulated from the water circuit, and back into the receiver.

The water circuit consists of a circulation pump, a shunt coupling, and a water chiller. The water circuit and the glycol/water circuit are interlinked through the shunt heat exchanger. The excess heat is dissipated in the water chiller to mains water.

The working fluid circuit consists of a two-stage compressor, two absorbers, two desorbers, two solution heat exchangers, a desuperheater, a booster pump, a solution pump, an expansion valve, a high-pressure receiver and a low-pressure liquid/vapour separator. The principle operation of the CAHP can be explained as follows. Starting from the compressor, ammonia with approximately 2% water at suction pressure and temperature enters the compressor and is compressed in two-stages with intermediate cooling to the discharge pressure. The vapour is then cooled in the desuperheater where most of the vapour superheat is transferred to the heat sink. Then the gas is mixed with the solution weak in ammonia before entering the absorber where the condensation and solution heat is transferred to the heat sink. The solution strong in ammonia is then further cooled in the solution heat exchanger 1 before it is expanded in the expansion valve to low pressure. The resulting two-phase ammonia/water mixture then enters the desorber where ammonia is desorbed out of the mixture. The out coming vapour and liquid is separated in the liquid/vapour separator. The compressor draw the vapour away, and the solution weak in ammonia is pumped to high pressure in the booster

and solution pump. The solution weak in ammonia is heated in the solution heat exchanger 1 and 2.

Most of the working fluid charge will be in the low-pressure liquid/vapour separator. The high-pressure receiver stores the remainder of the charge. The content of the high-pressure receiver is of the same composition as the solution strong in ammonia circulating through the system.

An electronically adjustable circulation pump regulates the water flow to the compressor cylinder heads. The heat dissipated from the cylinder heads is delivered into the water circuit, thus preheating the water to the absorber 2.

.

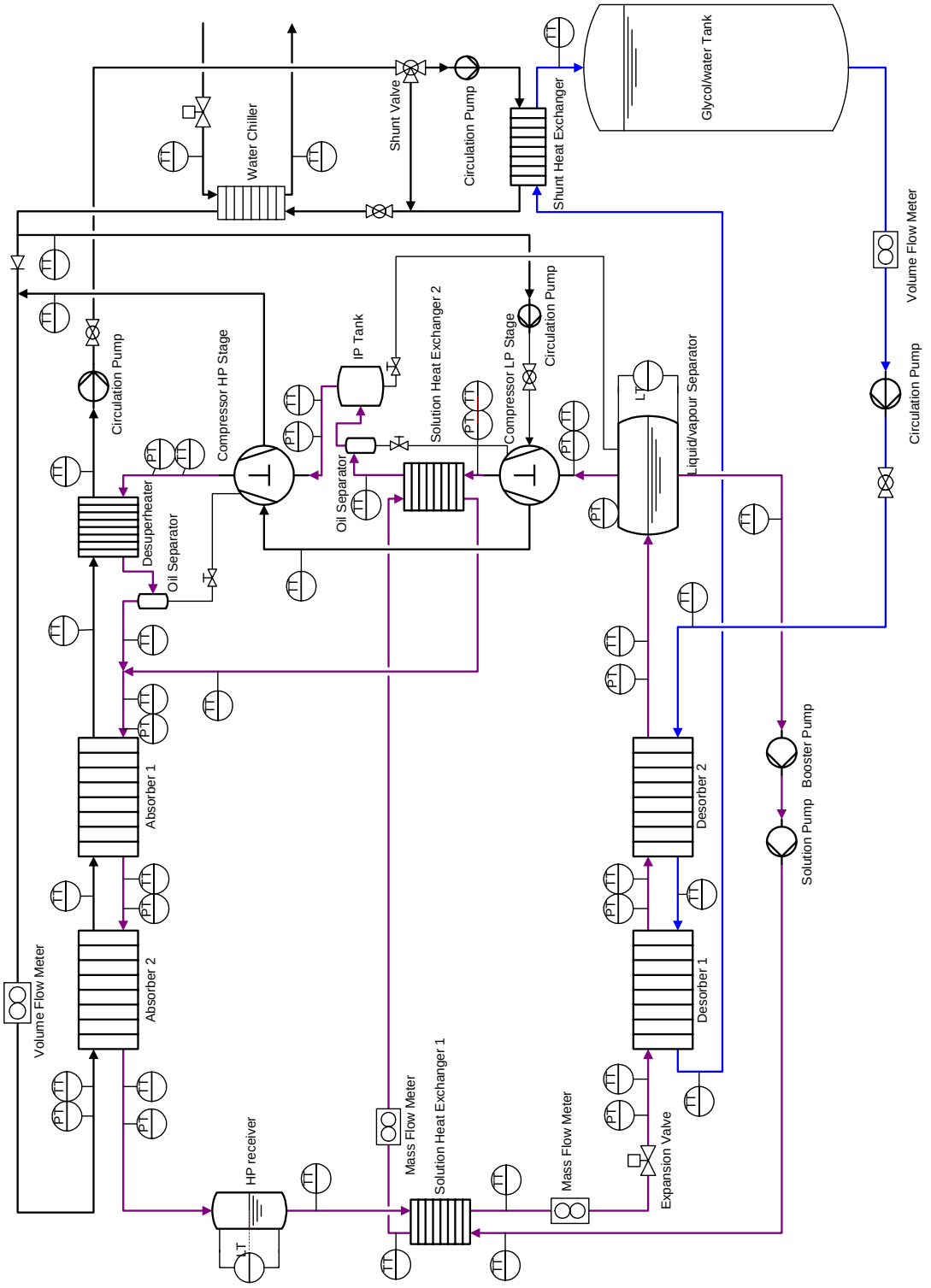

Figure 4–1: Flow diagram and measurement points of the laboratory compression/absorption heat pump

4.2 Component Description

4.2.1 Compressor

The compressor is an oil lubricated 8-cylinder York TCMO 28 reciprocating ammonia compressor, with water-cooled cylinder heads. A reciprocating compressor is chosen since a small size laboratory plant is desired. The compressor capacity can be adjusted in steps to 33%, 50%, 67% and 100%. A frequency converter is coupled to the electrical motor to regulate the rotational speed continuously. The compressor is delivered with two oil separators as standard. The compressor manufacturer recommended that two additional oil separators were installed to ensure sufficient oil separation, as the discharge temperatures are high. One is installed after solution heat exchanger 2 at the intermediate pressure, and the other is installed after the desuperheater at high pressure. The oil separators are connected to the compressor oil sump via steel pipes. Magnetic valves control the oil return. Table 4–1 shows the technical data for the compressor.

One of the main challenges using ammonia/water is to make sure that properly lubrication of the compressor is obtained during long-term operation. Synthetic polyalfaolifin type lubrication oil has been chosen. This oil is recommended by the oil manufacturer as the best oil for the combination of water and high temperature. The oil has a viscosity of 208 cSt at 40°C and 24.7 cSt at 100°C. This oil can be mixed with some water, and still maintain its lubrication properties. Due to the return of the lubrication oil from the heat pump components and back to the compressor it is important to use a non-soluble oil in the compressor.

Table 4–1: Technical data for the compressor

Manufacturer	York Refrigeration
Type	Reciprocating, oil lubricated, water- cooled cylinder heads
Number of cylinders	8 (6 low-pressure stage, 2 high-pressure stage)
Cylinder bore diameter	70 mm
Piston stroke	70 mm
Rotational speed	900-1460 rpm
Swept volume	141.9 m^3/h at 1460 rpm
Design pressure	26 bara

4.2.2 Solution and Booster Pump

The ammonia/water mixture in the liquid/vapour separator is saturated. To deal with eventually problems with cavitations in the pump suction line a booster pump capable to pump two-phase fluids is installed upstream the solution pump.

The solution pump is a diaphragm pump linked to a frequency converter controlled motor. The booster pump is a seal less magnetically coupled turbine pump suitable for very low net

positive suction head (NPSH) values. Table 4–2 and 4–3 shows the technical data for the solution and booster pump.

Table 4–2: Technical data for the solution pump

Manufacturer	Hydra-Cell
Type	Membrane pump F-20 with S cam
Capacity	0-0.035 l/s
Pressure	up to 103 bar
Temperature (max)	120°C

Table 4–3: Technical data for the booster pump

Manufacturer	Caster
Type	Regenerative turbine pump MTA 25
Capacity	0.111 l/s at 0.5 bar back pressure
Pressure	max 0.7 bar
NPSH	min 0.5 m

4.2.3 Heat exchangers

All heat exchangers in the laboratory heat pump are plate heat exchangers manufactured by Alfa Laval AS. In the main circuit nickel-brazed plate heat exchangers are used, and in the secondary circuits copper-brazed plate heat exchangers. Plate heat exchangers are utilised in order to reduce the physical dimensions of the laboratory heat pump.

A plate heat exchanger has very complicated flow geometry with sudden contractions and changes in flow direction. This may keep the two phases of the working fluid mixture well mixed.

The heat exchangers with single-phase heat exchange, i.e. the solution heat exchangers, the desuperheater, the shunt heat exchanger and the water chiller, were designed using Alfa Laval's heat exchanger design program, CAS2000[61] . The design parameters are listed in Table 3–5.

Care must be taken when designing the desorber and absorber due to the non-linear properties of the ammonia/water mixture during phase change processes. An ammonia-water mixture with an ammonia concentration of 73 weight-% has a temperature glide of approximately 95K during total condensation and total evaporation as shown in Figure 4–2 and 4–3. At the design conditions the mixture inlet temperature to the absorber is 110° C, and the mixture inlet temperature to the desorber is 1.3° C. This corresponds to a mixture temperature glide of 49 K in the absorber, and 44 K in the desorber.

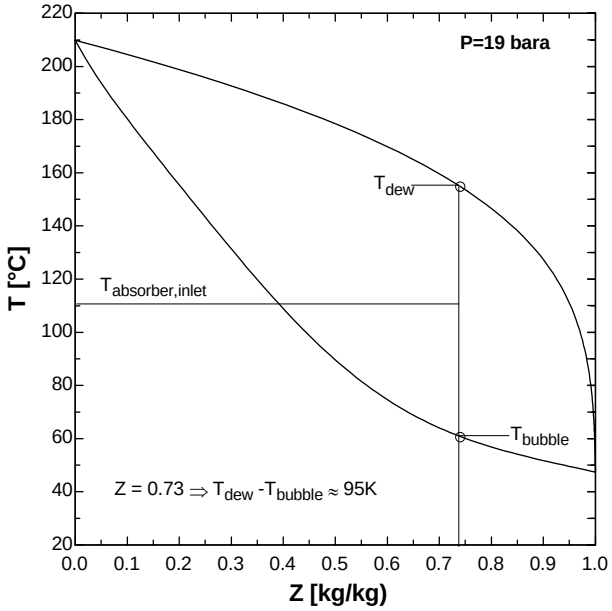

Figure 4–2: Dewpoint temperatures and bubble point temperatures for the ammonia-water mixture as a function of ammonia mass fraction at absorber pressure.

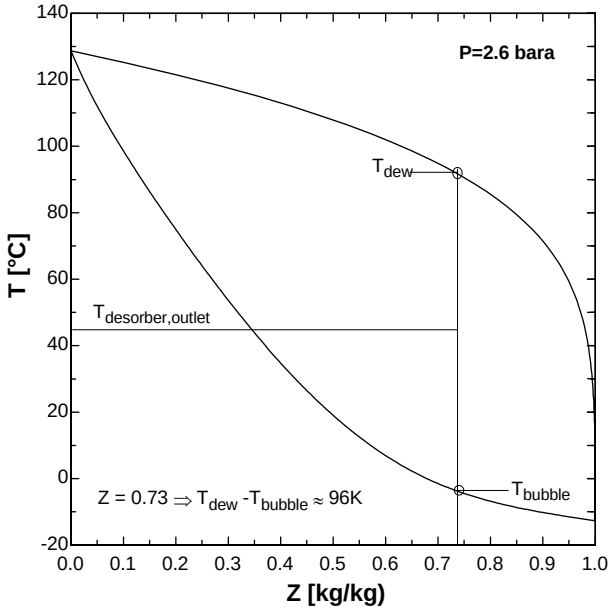

Figure 4–3: Dewpoint temperatures and bubble point temperatures for the ammonia-water mixture as a function of ammonia mass fraction at desorber pressure.

4.2.3.1 Absorber

One of the major challenges when dealing with plate heat exchangers for two-phase applications is to ensure good liquid/vapour mixing and distribution in the heat exchanger inlet manifold. Improper distribution of the two-phase flow will result in poor distribution of the working fluid and only parts of the heat exchanger area will be effective. The ammonia-water

mixture can flow downwards as in a falling film type of absorber or upwards as in a bubble type absorber. Kang et al [51] evaluated the two different flow modes analytically, and reported that the bubble type absorber has better characteristics and can be made more compact. Falling film absorbers provide high heat transfer coefficients and low pressure drop along the absorber. The liquid film is however sensitive to instabilities, which results in incomplete wetting and reduced areas for heat and mass transfer. Falling film absorbers therefore need liquid distributors at the liquid inlet. Bubble type absorbers provide high heat- and mass transfer coefficients and good mixing between liquid and vapour but have higher pressure drop. Bubble absorbers require vapour distribution and vapour distribution is generally easier to accomplish than liquid distribution.

Figure 4–4 and Table 4–4 shows the plate characteristics of the plates in the chosen heat exchanger type. A high corrugation angle plate type was chosen to promote the distribution of the ammonia-water mixture in the absorber.

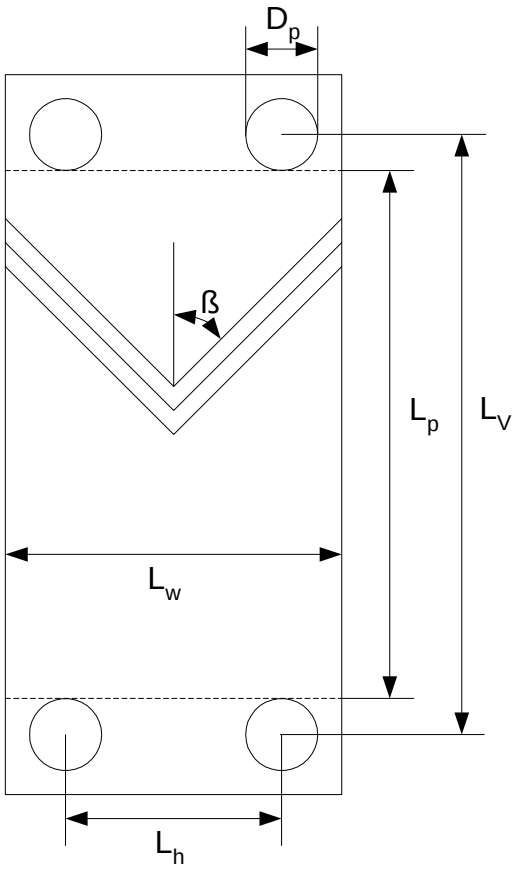

Figure 4–4: Main dimensions of a chevron plate

Table 4–4: Plate characteristics for absorber plates

Parameter	Value
Heat transfer area per plate [m^2]	0.1
Corrugation angle (β) [°]	60
L_v [m]	0.518
L_p [m]	0.465
L_h [m]	0.092
L_w [m]	0.178
Port diameter (D_p) [m]	0.053
Channel hydraulic diameter [m]	0.003

Initially a falling film absorber with 36 channels was installed in the heat pump. The liquid was distributed in a nozzle at the absorber inlet. Experiments revealed problems with the distribution of two-phase flows resulting in poor absorber performance (Baksaas et al.[52]). The detailed model described in chapter 4.2.3 was developed to make a new design of the absorber.

A series of calculations were performed to check the influence of the number of channels on the mixture side of the heat exchanger on the heat transfer and pressure drop. Figure 4–5 shows the absorber total area, UA value and length as a function of the number of channels on the mixture side. The UA value remains almost unchanged, but the area decrease with decreasing number of channels. Figure 4–6 shows the pressure loss and the mean overall heat transfer coefficient in the absorber. The pressure losses increase quickly when the number of channels is below 20, but the losses are not large.

It was decided to install two heat exchangers mounted in series to improve the working fluid distribution. In absorber 1 the ammonia vapour and the weak ammonia solution are mixed at the bottom, thus operating as a bubble absorber. Absorber 2 is operated as a falling film device. Specially designed inserts were installed in the inlet ports of both heat exchangers to improve the distribution of the ammonia-water mixture. The absorbers are equal, with 9

channels on the mixture side giving a total heat exchange area of 3.6 m^2. Table 4–5 show the technical data for absorber 1 and 2.

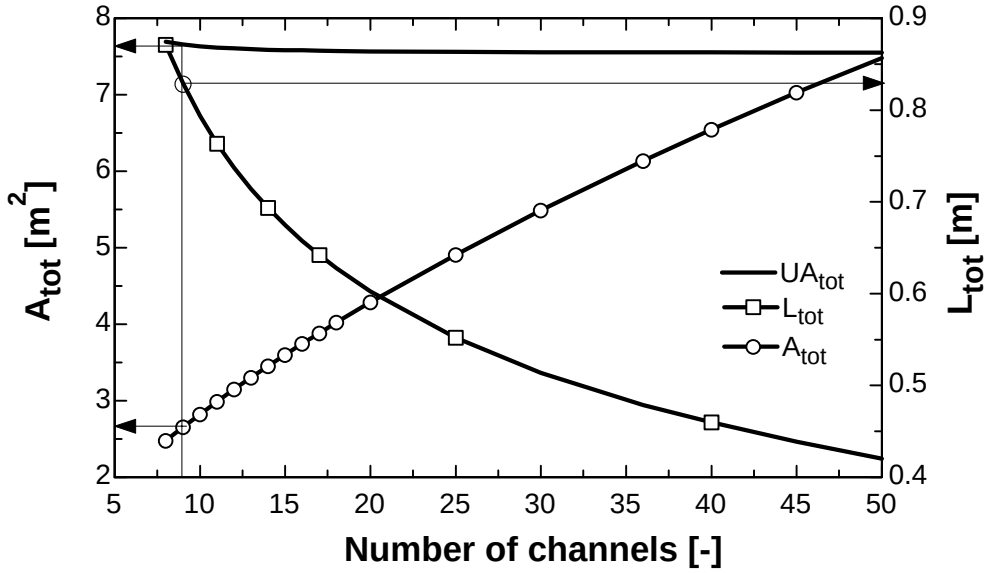

Figure 4–5: Absorber total heat exchange area, UA value and length as a function of number of channel on the mixture side

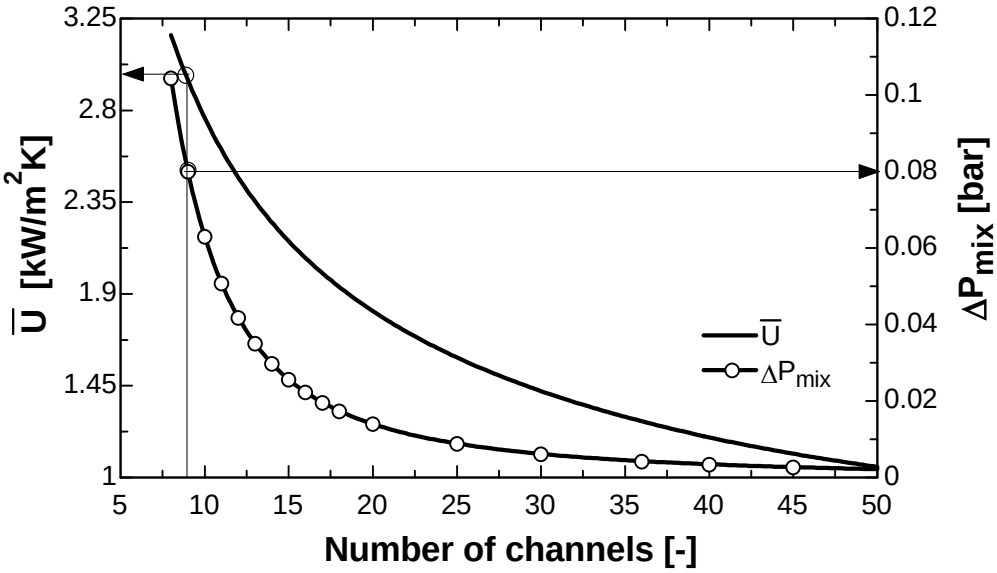

Figure 4–6: Pressure drop and overall heat transfer coefficient as a function of number of channels on the mixture side

Table 4–5: Technical data for the absorber 1 and 2

Manufacturer	Alfa Laval AS
Type	Nickel-brazed plate heat exchanger NB76-20E
Material	Stainless steel

Table 4–5: Technical data for the absorber 1 and 2

Design pressure	26 bara
Heat Transfer Area	1.8 m^2

Figure 4–7 and 4–8 show the predicted local heat transfer coefficients as a function of the local vapour mass fraction for the chosen heat exchanger with 9 channels on the mixture side. The main resistance to heat transfer is on the mixture side. The effects of the Silver correction for vapour sensible heat, the effects of the condensation mass flux, and the interface roughness are shown in Figure 4–8. The local values of the condensation mass flux correction factor (θ) and the interface roughness correction factor (C_f) are shown in Figure 4–9. The effects of the correction factors are significant when the vapour mass fraction is larger than 20%. The effect of the condensation mass flux and the interface roughness are small compared to Silver correction. The condensation mass flux effect is of minor importance compared to the interface roughness effect.

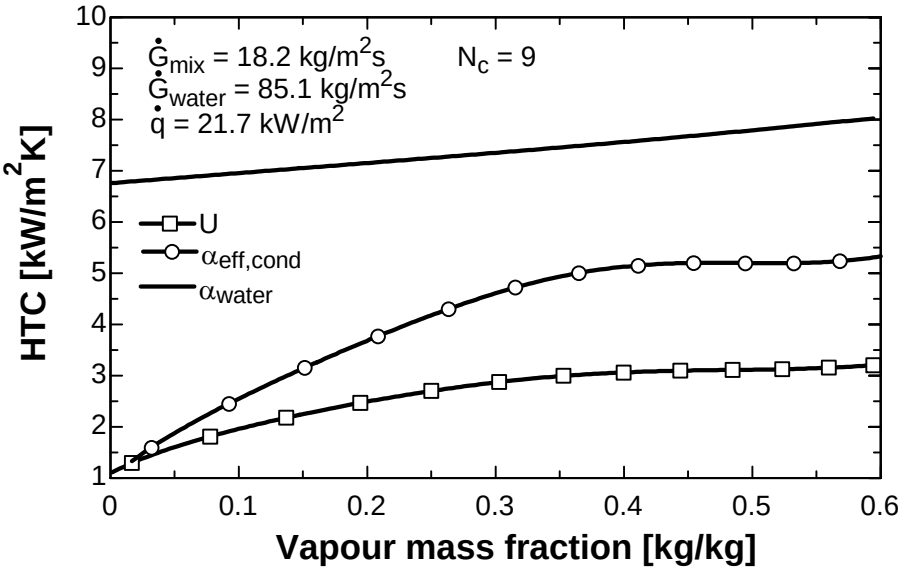

Figure 4–7: Calculated local heat transfer coefficients as function of vapour mass fraction in the absorber

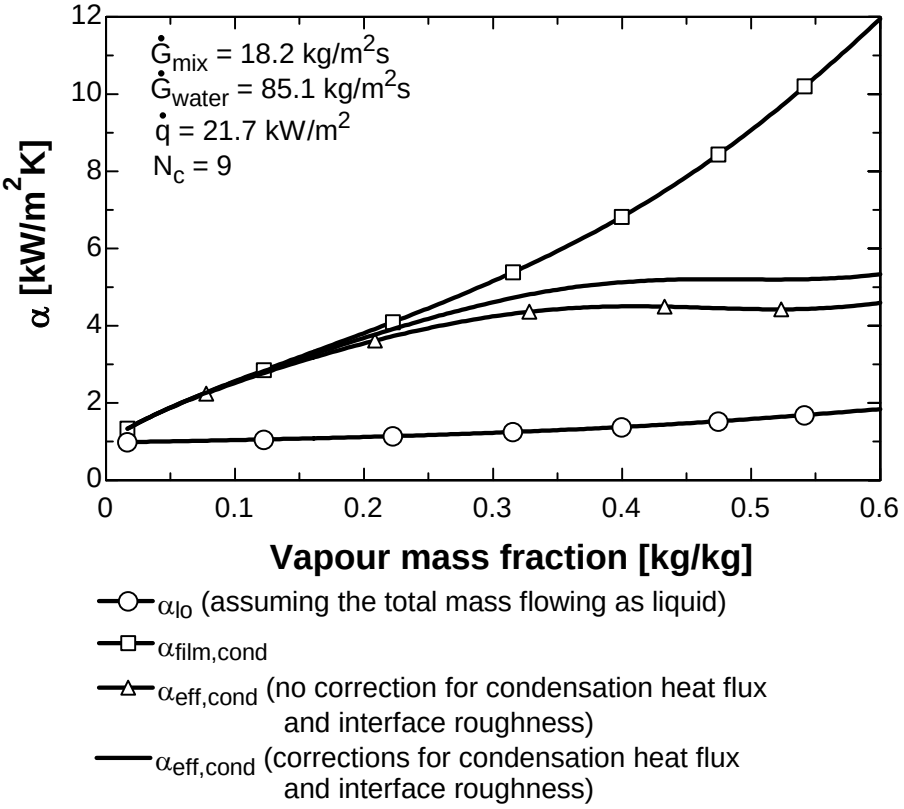

Figure 4–8: Calculated local heat transfer coefficients on the mixture side as function of the vapour mass fraction in the absorber

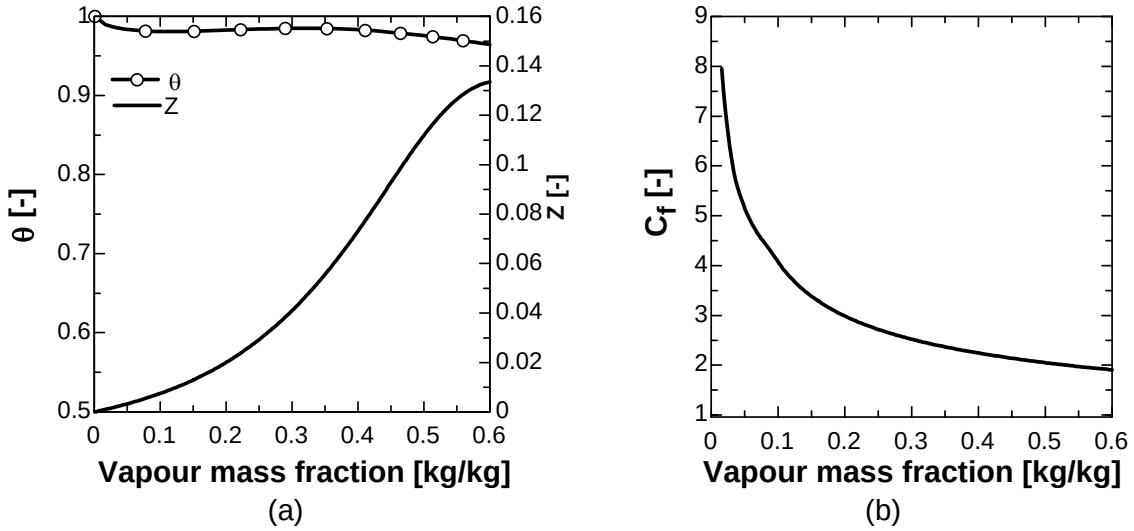

Figure 4–9: Correction factors as a function of vapour mass fraction

4.2.3.2 Desorber

The same challenges with the distribution of the two-phase mixture in the inlet manifold arise in the desorber as with the absorber. The vapour mass fraction at the desorber inlet is about 20%, compared to about 60% in the absorber, making the distribution easier in the desorber.

Initially a desorber with 17 channels on the mixture side was installed. The heat exchange area was 3.6m^2. Experiments revealed problems meeting the design requirements, so it was decided to replace the desorber. The new desorber consists of two plate heat exchangers mounted in series. Each desorber unit have 8 channels on the mixture side in order to maintain the heat exchange area. Table 4–7 shows the technical data for the desorber units.

The characteristics of the plates in the chosen plate heat exchanger are listed in Table 4–6.

Table 4–6: Plate characteristics for the desorber plates

Parameter	Value
Heat transfer area per plate [m^2]	0.1
Corrugation angle (β) [°]	60
L_v [m]	0.518
L_p [m]	0.465
L_h [m]	0.092
L_w [m]	0.178
Port diameter (D_p) [m]	0.053
Channel hydraulic diameter [m]	0.0044

As for the absorber, as series of calculations were performed to check the influence of the number of channels on the mixture side on the heat transfer and pressure drop. Figure 4–10 shows the desorber total heat exchange area, UA value and length as a function of the number of channels on the mixture side. Figure 4–11 shows the pressure drop and mean overall heat transfer coefficient as a function of the number of channels on the mixture side.

The new desorber is to large according to Figure 4–10, as one heat exchanger with 8 channels on the mixture side is enough. However based on practical tests in the laboratory, it was decided to keep the original heat transfer area using to heat exchangers in series. The design model will be validated against the experimental results in chapter 5.4.

.

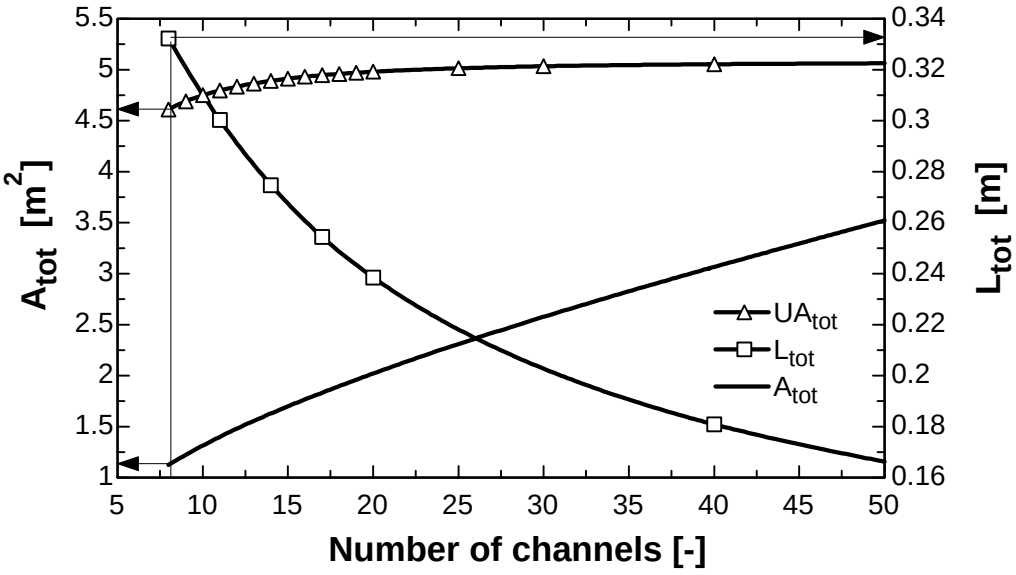

Figure 4–10: Desorber total heat exchange area, UA value and length as a function of number of channel on the mixture side

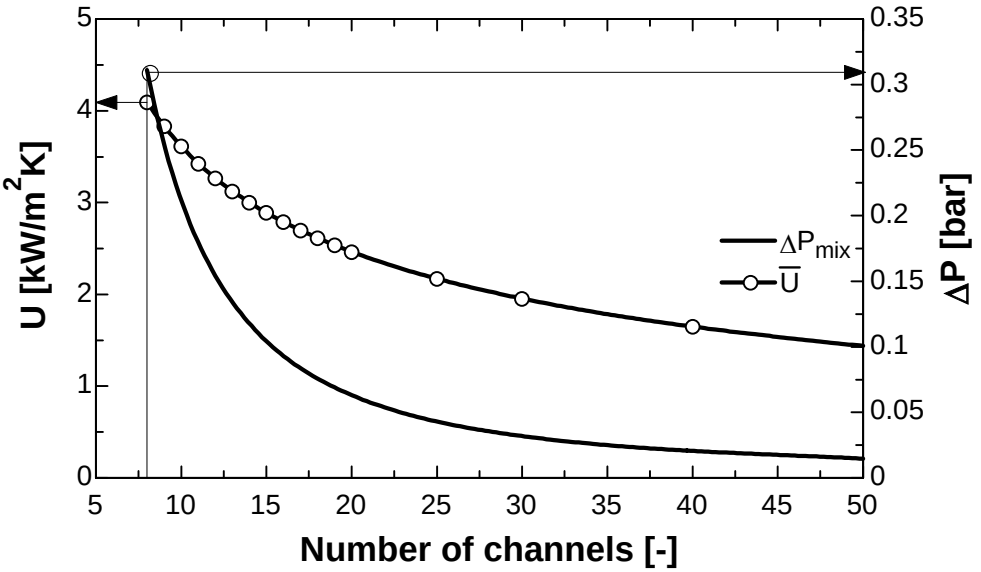

Figure 4–11: Pressure drop and overall heat transfer coefficient as a function of number of channels on the mixture side

Table 4–7: Technical data for desorber 1 and 2

Manufacturer	Alfa Laval AS
Type	Nickel-brazed plate heat exchanger NB76-18H
Material	Stainless steel

Table 4–7: Technical data for desorber 1 and 2

Design pressure	26 bara
Heat Transfer Area	1.6 m^2

Figure 4–12 and 4–13 show the predicted local heat transfer coefficients as a function of the local vapour mass fraction for a heat exchanger with 8 channels on the mixture side. The dominating resistance to heat transfer is on the water side. The effects of the Silver correction and the interface roughness are shown in Figure 4–13. The local values of the interface roughness correction factor (C_f) are shown in Figure 4–14. As with the absorber the effect of the interface roughness correction factor is small compared to the Silver correction for vapour sensible heat. The nucleate boiling component of the boiling film heat transfer coefficient is insignificant.

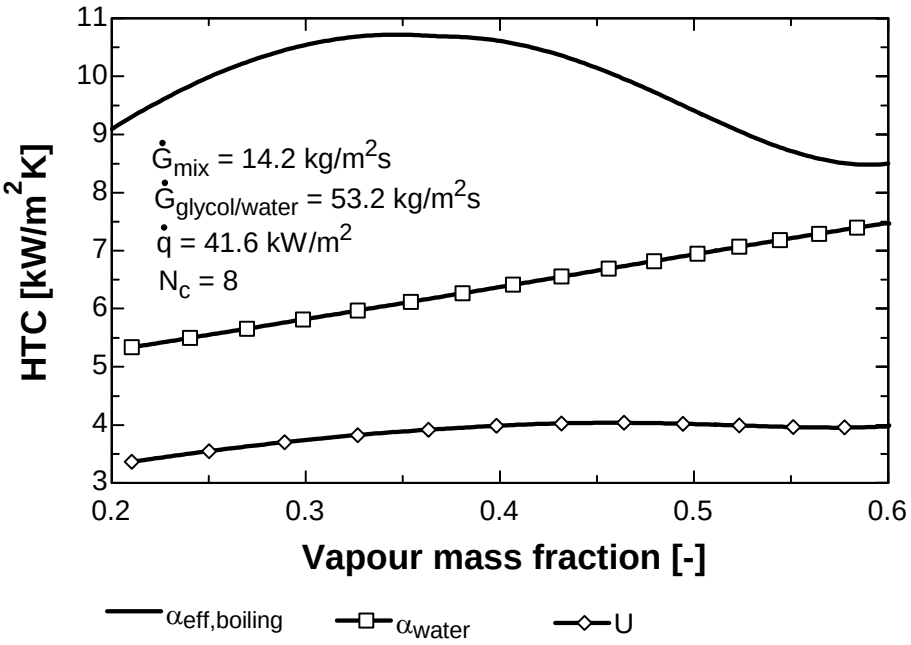

Figure 4–12: Calculated local heat transfer coefficients as function of vapour mass fraction in the desorber

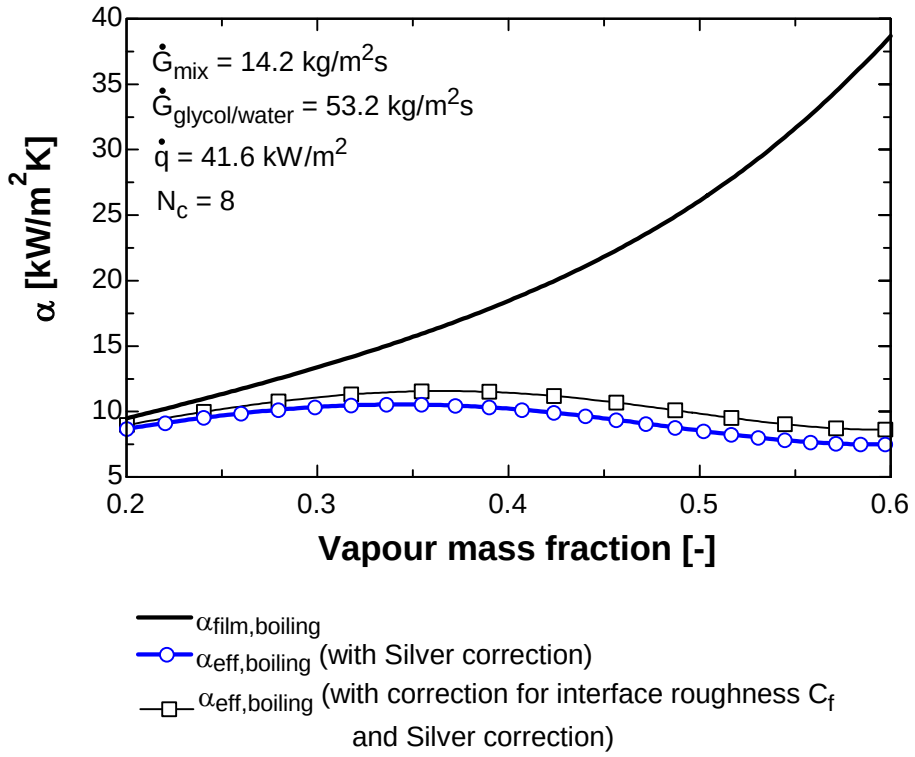

Figure 4–13: Calculated local heat transfer coefficients on the mixture side as function of the vapour mass fraction in the desorber

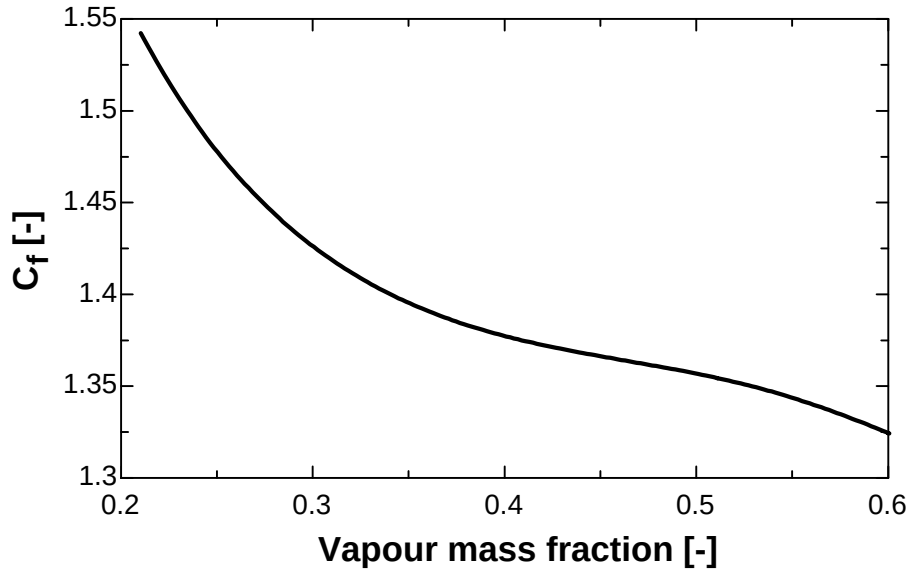

Figure 4–14: Correction factor for surface roughness as a function of the vapour mass fraction in the desorber

4.2.3.3 Solution Heat Exchangers

Table 4–8 and 4–9 shows the technical data for the solution heat exchanger 1 and 2 respectively.

Table 4–8: Technical data for solution heat exchanger 1

Manufacturer	Alfa Laval AS
Type	Nickel-brazed plate heat exchanger NB14-5H
Material	Stainless steel
Design pressure	26 bara
Heat Transfer Area	0.1 m^2
Number of plates	5

Table 4–9: Technical data for solution heat exchanger 2

Manufacturer	Alfa Laval AS
Type	Nickel-brazed plate heat exchanger NB26-30H
Material	Stainless steel
Design pressure	26 bara
Heat Transfer Area	0.8 m^2
Number of plates	30

4.2.3.4 Desuperheater

Table 4–10 shows the technical data for the desuperheater.

Table 4–10: Technical data for the desuperheater

Manufacturer	Alfa Laval AS
Type	Nickel-brazed plate heat exchanger NB26-6L
Material	Stainless steel
Design pressure	26 bara
Heat Transfer Area	0.2 m^2
Number of plates	6

4.2.3.5 Secondary System

Table 4–11 and 4–12 shows the technical data for the shunt heat exchanger and the external water chiller.

Table 4–11: Technical data for the shunt heat exchanger

Manufacturer	Alfa Laval AS
Type	Copper-brazed plate heat exchanger NB26-20H
Material	Stainless steel
Design pressure	6 bara
Heat Transfer Area	0.3m^2
Number of plates	20

Table 4–12: Technical data for the external water chiller

Manufacturer	Alfa Laval AS
Type	Copper-brazed plate heat exchanger CB26-50H
Material	Stainless steel
Design pressure	6 bara
Heat Transfer Area	1.3 m^2
Number of plates	50

4.2.4 Expansion valve

An electromechanical expansion valve of type Sauter V6S15F355 with a linear characteristic is used.

4.3 Instrumentation and Measurement Accuracy

4.3.1 Data Acquisition

A data acquisition system is installed to enable on-line measurement and control of the heat pump system. The data acquisition system consists of three 24-channel Intab data loggers coupled to a computer. All measurements are measured every second and mean values for every 20 seconds are logged. The measurement system acquires data and processes it on-line. After acquiring data, the performance of the heat pump and its components are evaluated instantaneously and displayed on the screen.

4.3.2 Temperature measurement

All temperature measurements were carried out by type-T thermocouples with an accuracy of ±0.5 °C. The thermocouples were placed into small diameter stainless steel wells, and they were connected to a data logger which have an electronic zero point compensation. The measurement chain from logger to the thermocouples was calibrated on-site against a LAUDA thermostats type RK 8 KS with an absolute accuracy of 0.2% of reading $\pm 0.2K$.The measurement chain (logger to thermocouple) was calibrated at $0°C$ and $80°C$.

4.3.3 Pressure measurement

The pressures were measured with Druck PTX1400 pressure transmitters. The measurement points were installed vertically on the pipe surface. The accuracy of the pressure transmitters is ±0.25 % of the measured value. To avoid errors due to temperature effects the pressure transmitters were mounted with impulse lines. The measurement chain from logger to the pressure transmitters were calibrated on-site against a DRUCK UNOMAT model TRX II using a PDCR IS-1745/A pressure sensor with range from 0 to 40 bar and an accuracy of ±0.05 % of full scale. The measurement chain was calibrated at two pressures.

4.3.4 Mass flow and concentration measurement

Coriolis mass flow meters from Krohne (type CORIMASS MFM3081K-1.5E and CORIMASS MFM3081-10E) were installed in the weak and strong ammonia solution circuits to measure the mass flow and density. The coriolis meters were calibrated with water against a high precision weight scale at Krohne. The certified accuracy of the Coriolis meter in the weak solution line is ±0.02 % for mass flow, and ±0.002 kg/m^3 for density. The certified accuracy of the Coriolis meter in the strong solution line is ±0.04 % for mass flow, and ±0.002 kg/m^3 for density. The pressure drop through the flow meter in the weak ammonia solution line is about 0.7bar, and the pressure drop through the flow meter in the strong ammonia solution line is about 0.3bar.

The ammonia concentration in the mixture is estimated from equilibrium calculation at the desorber 2 outlet. The ammonia concentration can be estimated using the coriolis density measurements or from assuming equilibrium at the desorber 2 outlet. The results from the two methods has been compared with ammonia concentrations determined by titration in Appendix E

4.3.5 Volume flow measurement

The water and water/glycol volume flows on the heat source and heat sink side were measured with Aquametro PMK-RH20 flow meters. The accuracy of the flow meters is ±2 % of the measured value.

4.3.6 Power measurement

The power consumption of the electric motor were measured with a HIOKI 3165 clamp-on power meter with an accuracy of ±0.5 % of the measured value plus ±0.3 % of full load. The full load is 40kW. The rotational speed of the compressor shaft was measured with an inductive rotation meter with an accuracy of ±1 RPM.

4.3.7 Data reduction and uncertainty of the calculated values

The heat loads of the absorbers, desorbers and the desuperheater were determined with the following energy balances on the heat sink and heat source side.

$$\dot{Q}_{abs1} = \dot{m}_{wa} \cdot (h_{wa3} - h_{wa2}) \tag{4.1}$$

$$\dot{Q}_{abs2} = \dot{m}_{wa} \cdot (h_{wa2} - h_{wa1}) \tag{4.2}$$

$$\dot{Q}_{desuperheater} = \dot{m}_{wa} \cdot (h_{wa4} - h_{wa3}) \tag{4.3}$$

$$\dot{Q}_{des1} = \dot{m}_{wd} \cdot c_{pwd2} \cdot (T_{wd2} - T_{wd3}) \tag{4.4}$$

$$\dot{Q}_{des2} = \dot{m}_{wd} \cdot c_{pwd1} \cdot (T_{wd1} - T_{wd2}) \tag{4.5}$$

were h is enthalpy, m is mass flow, c_p is specific heat capacity and T is temperature in $C°$.

The coefficient of performance for heating is defined as the ratio between the heat delivered to the heat sink to the sum of the compressor electric motor power and the pump work.

$$COP_{Heating} = \frac{\dot{Q}_{abs1} + \dot{Q}_{abs2} + \dot{Q}_{desuperheater}}{\dot{W}_{motor} + \dot{W}_{pumps}} \tag{4.6}$$

The pump work is the sum of the solution pump work and the booster pump work. The solution pump work is calculated using a correlation given by the pump manufacturer:

$$W_{\text{solution pump}} = \frac{2 \cdot RPM_{pump}}{84428} + \frac{\dot{V}_{pump} \cdot \Delta p}{511} \tag{4.7}$$

where the RPM_{pump} is the rotational velocity, Δp is the pressure lift, and $\dot{V}_{pump}$ is the volume flow of solution given by:

$$\dot{V}_{pump} = \frac{\dot{m}_{13}}{\rho_{13}} \cdot 1000 \cdot 60 \qquad \left[\frac{dm^3}{min}\right] \tag{4.8}$$

The booster pump work is calculated assuming a linear correlation with the flow rate:

$$W_{\text{booster pump}} = 0.125 \cdot \frac{\dot{V}_{pump}}{\dot{V}_{max}} \tag{4.9}$$

where $\dot{V}_{max}$ is the maximum flow rate of the pump, given as:

$$\dot{V}_{max} = 2.08 \cdot \frac{1460}{1750} \tag{4.10}$$

The heat efficiency is used to check for heat losses. The heat efficiency is defined as the ratio between the heats delivered to the heat sink to the combined heat and work input from the heat source and the compressor shaft power.

$$\text{Heat efficiency} = \frac{\dot{Q}_{abs1} + \dot{Q}_{abs2} + \dot{Q}_{desuperheater} + \dot{Q}_{coolingLP} + \dot{Q}_{coolingHP}}{\dot{Q}_{des1} + \dot{Q}_{des2} + \dot{W}_{shaft}} \tag{4.11}$$

The compressor shaft power were calculated as:

$$\dot{W}_{shaft} = \dot{W}_{motor} \cdot \eta_{motor} \tag{4.12}$$

with a motor efficiency, η_{motor}, of 0.81.

The compressor volumetric efficiency is defined as the ratio of the actual mass flow rate to the theoretical mass flow rate. The volumetric efficiency for low-pressure stage and the high-pressure stage was calculated with the following equations.

$$\eta_{volLP} = \frac{\dot{m}_1 \cdot v_1}{\dot{V}_{dispLP}} \tag{4.13}$$

$$\eta_{volHP} = \frac{\dot{m}_3 \cdot v_3}{\dot{V}_{dispHP}} \tag{4.14}$$

where the high-pressure stage displacement volume is given by:

$$\dot{V}_{dispHP} = \dot{V}_{dispLP} \cdot \frac{2}{6} \tag{4.15}$$

The displacement volume is a function of the compressor rotational velocity:

$$\dot{V}_{dispLP} = V_{dispLP} \cdot \frac{RPM}{RPM_{max}} \tag{4.16}$$

where RPM is the measured rotational velocity during the tests and RPM_{max} is 1800 rpm.

The compressor isentropic efficiency is defined as the ratio between the compressor isentropic work at the low-pressure and high-pressure stage to the calculated actual work:

$$\eta_{isen} = \frac{\dot{m}_1 \cdot (h_{2isen} - h_1) + \dot{m}_3 \cdot (h_{4isen} - h_3)}{W_{shaft}} \tag{4.17}$$

where the shaft work, W_{shaft}, is calculated as in Equation 4.12.

The overall heat transfer coefficient in the heat exchangers is calculated as:

$$U = \frac{\dot{Q}}{A_{HT} \cdot LMTD} \tag{4.18}$$

where A_{HT} is the heat transfer area and $LMTD$ is the logarithmic mean temperature difference calculated as:

$$LMTD = \frac{(T_{hot,\,in} - T_{cold,\,out}) - (T_{hot,\,out} - T_{cold,\,in})}{\ln \langle (T_{hot,\,in} - T_{cold,\,out}) / (T_{hot,\,out} - T_{cold,\,in}) \rangle} \tag{4.19}$$

Since there is no temperature measurement point after mixing of the vapour coming from the desuperheater and the weak solution coming from the solution heat exchanger 2, the temperature at the absorber 1 inlet is calculated assuming adiabatic mixing of the two flows.

The relative uncertainty in the calculated values is estimated using the theory of propagation of errors as outlined in Appendix F. Table 4–13 shows the resulting relative uncertainties for the calculated values.

Table 4–13: Resulting relative uncertainties for the calculated values.

Parameter	Relative uncertainty [%]
$COP_{Heating}$	2.9-3.4
Heat sink load	2.6-3.2
Heat source load	2.9-3.5
Compressor isentropic efficiency	1.2-1.3
Compressor LP stage volumetric efficiency	0.33-0.44
Compressor HP stage volumetric efficiency	0.33-0.50
Overall heat transfer coefficient absorber 1	4.9-5.6
Overall heat transfer coefficient absorber 2	7.2-11.6
Overall heat transfer coefficient desorber 1	4.4-6.8
Overall heat transfer coefficient desorber 2	7.9-18.5
Overall heat transfer coefficient solution heat exchanger 1	10.5-19.5
Overall heat transfer coefficient solution heat exchanger 1	3.2-7.6
Overall heat transfer coefficient desuperheater	10.6-29.1
Overall heat transfer coefficient absorber (1+2)	3.1-4.1
Overall heat transfer coefficient desorber (1+2)	6.0-12.8
Ammonia concentration in strong solution	0.2-0.3
Ammonia concentration in weak solution	0.8-1.0

4.4 System Charging

The design specification is for a 73/37 weight-% of ammonia-water mixture as the circulating composition. The system charge concentration was determined to be 0.45 weight-% of ammonia with a total system charge of 28.5 kg. Prior to charging the system was evacuated to remove the nitrogen introduced while leakage testing the system. Firstly distilled water was added to the low-pressure reservoir. Then the ammonia vapour was added slowly to the system with ammonia dissolving into the water.

4.5 Test Procedure

The test rig is equipped with a control system connected to a computer. The compressor, the booster pump, the solution pump, the expansion valve, and the mains water control valve can

be controlled from the computer. The circulation pumps in the secondary circuits have to be manually set. The circulation pumps have three flow rate settings. Manual valves installed in the circulation pump outlet lines achieve additional flow rate adjustments. The heat source inlet temperature is set by two resistance heating elements in the glycol/water storage tank. A PID regulator controlling the mains water flow rate sets the heat sink inlet temperature.

Test procedure:

1) The circulation pumps in the water and brine circuits were switched on.
2) The flow regulation valves in the water and brine circuits were set fully open.
3) The expansion valve was set to fully open.
4) The compressor, the booster pump and the solution pump was started. The compressor was set to 33% capacity at start-up.
5) When the suction pressure was stabilised the expansion valve opening was gradually decreased until complete absorption is achieved in the absorber. The compressor was then adjusted to the specified capacity.
6) The mass flows in the water and brine circuit were set to their specified values.
7) The heat pump was operated until steady state conditions were obtained.
8) All measuring point were logged.

5 Experimental Results

A series of tests were carried out to investigate the operational range of the test facility. The aim of the tests was to establish the basic characteristics of the compression/absorption heat pump (CAHP) and its components.

The advantages with the CAHP over the single fluid vapour compression heat pump are related to the possibility of controlling the heating capacity by adjusting the composition of the working fluid mixture, and of matching the temperature glide of the working fluid to that of the source/sink.

The composition of the working fluid mixture in the solution circuit can be changed by variation of the amount of liquid working fluid stored in the high-pressure receiver. A decrease in the concentration in the solution circuit reduces the pressure at constant temperatures. A reduction of the pressure at the compressor inlet reduces the mass flow rate through the compressor at constant volume flow rate.

The temperature glide of the working fluid can be changed by variation of the flow ratio between the mass flow of solution weak in ammonia going through the solution pump, and the mass flow of ammonia vapour going through the compressor.

The experimental results are used to validate the computer model used to design the compression/absorption heat pump system. The compressor, the absorber and the desorber are validated with respect to their characteristics. The compressor was represented by the isentropic and volumetric efficiency. The absorber and desorber model was examined by a study of the overall heat transfer coefficient and the pressure drop.

5.1 System Performance

The tests were performed with constant mass flow and inlet temperature of the heat sink and heat source medium. The heat sink and heat source mass flow was 0.258kg/s and the inlet temperatures were 50 ° C. The compressor was operated at 100% capacity and at a rotational velocity of approximately 1000rpm.

Figure 5–1 shows the measured heat load in the desorber and absorber of the test plant as a function of the composition of the weak solution. The composition of the weak solution was altered by variation of the amount of working fluid stored in the high-pressure receiver. The heat load in the absorber varied from 30 to 47kW corresponding to concentrations in the weak solution between 26 and 34% by mass. The heat load in the desorber varied between 25 to 35kW.

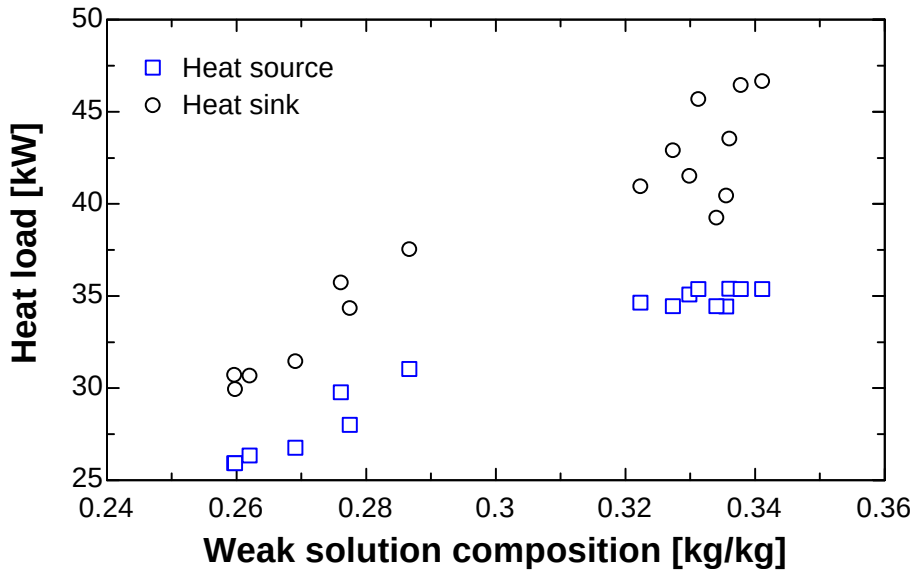

Figure 5–1: Heat load in absorber and desorber as a function of the weak solution composition

The volumetric flow rate through the compressor is fixed, as the rotational velocity was kept constant, therefore the mass flow is proportional to the suction vapour density. The major influence on the mass flow rate through the compressor is the desorber pressure, since the vapour temperature and composition do not vary significantly. Increasing the vapour mass flow increases the amount of ammonia in the strong solution. With increasing composition in the strong solution a larger part of the fluid flowing through the desorber is vapourised and the ratio of vapour to the overall flow rate increases, as seen in Figure 5–2. The mass fraction of vapour at the absorber inlet is smaller than the vapour mass fraction at the desorber outlet, as the weak solution is subcooled prior to the mixing with the ammonia vapour at the absorber inlet. Some of the vapour heat is then used to heat the weak solution to the saturation temperature, thus reducing the maximum available equilibrium temperature. The composition of the strong solution is a function of the circulation ratio $(\dot{m}_{ws}/\dot{m}_{vapour})$, hence there exists a close relationship between the vapour mass fraction and the circulation ratio.

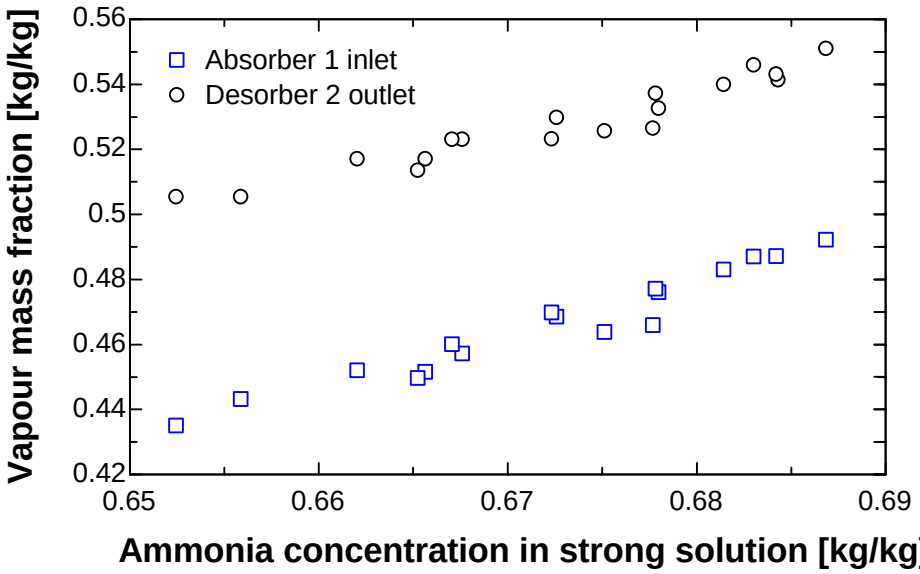

Figure 5–2: Vapour mass fraction at the absorber 1 inlet and desorber 2 outlets as a function of the ammonia concentration in the strong solution

The pressure ratio across the compressor and the specific compressor displacement are shown in Figure 5–3 as a function of the ammonia concentration in the weak solution. Both the pressure ratio and the specific compressor displacement decreased when the ammonia concentration of the weak solution increased. The specific compressor displacement decreases as a consequence of the higher equilibrium vapour pressure at the compressor inlet at higher ammonia concentration. The mass flow of ammonia vapour going through the compressor at constant rotational velocity is directly coupled to the inlet pressure, thereby increasing the heating capacity in the absorber. The lower pressure ratio at higher ammonia concentrations can be explained by a better 'match' of the heat exchanging medias in the absorber and desorber thereby decreasing the driving temperature differences, and by the lower gradient of the lines of constant liquid mass fraction in the logP-(1/T)-diagram. The scatter in the data at the lower concentrations (26-28%) occurs as a result of the rotational velocity of the solution pump not being held constant thus affecting the heat transfer in the absorber and desorber.

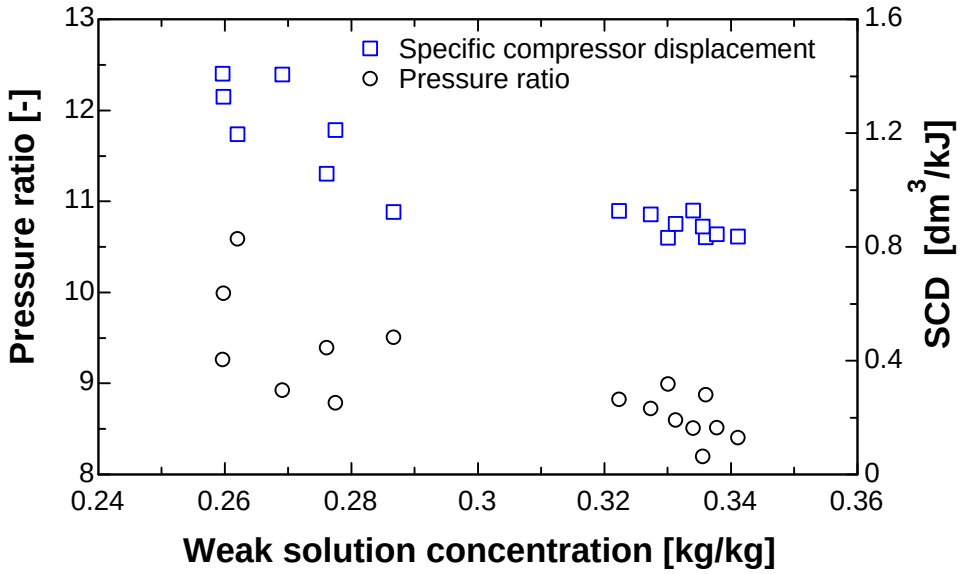

Figure 5–3: Specific compressor displacement and pressure ratio as function of the weak solution concentration

The heat transfer losses in the absorber and desorber are related to the temperature differences of the heat exchanging medias. Figure 5–4 and 5–5 shows the difference between the thermodynamic average temperatures of the solution and the heat transfer fluid in the absorber ($\Delta T_{m,\,absorber}$) and the desorber ($\Delta T_{m,\,desorber}$) as a function of the ratio of the temperature glide of the solution to the temperature glide of the heat sink/source fluid. Both $\Delta T_{m,\,absorber}$ and $\Delta T_{m,\,desorber}$ decreases when the ratio of the temperature glide on the solution side to the temperature glide on the source/sink side goes towards 1. Figure 5–4 and 5–5 also show that the absorber and desorber heat loads increases as the temperature glide ratio decreases.

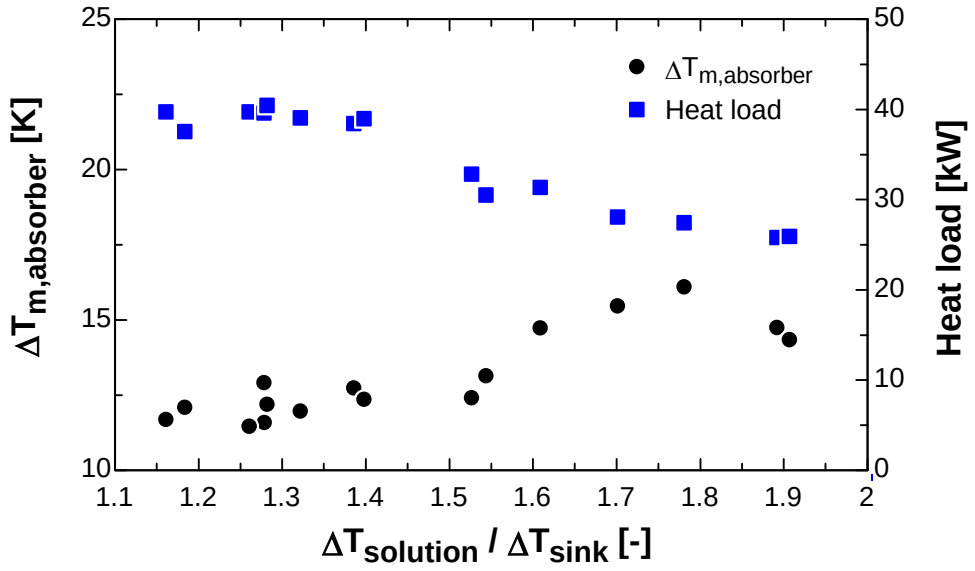

Figure 5–4: Difference in thermodynamic average temperature of the solution and the heat sink fluid and heat load in absorber as a function of the ratio of the temperature glide of solution to the temperature glide of the sink

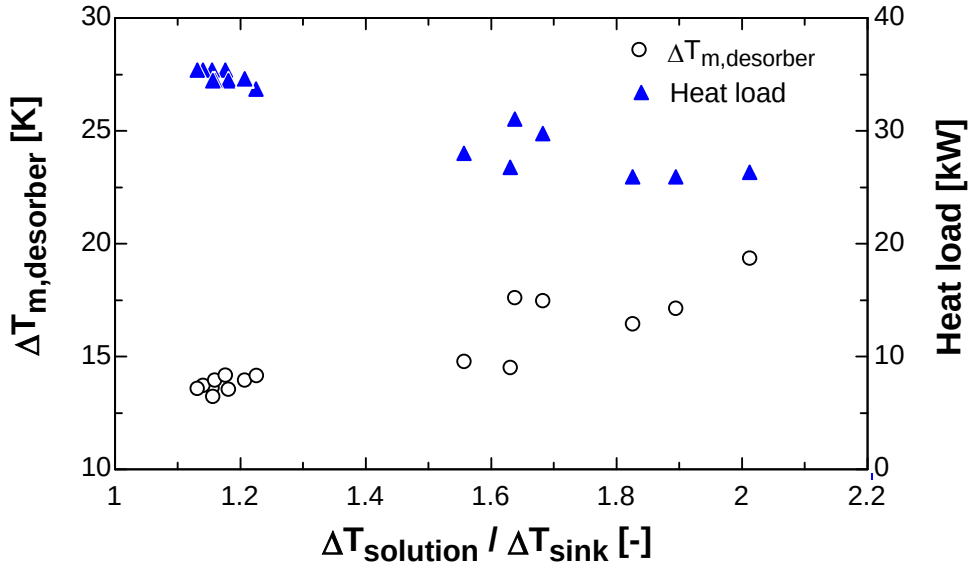

Figure 5–5: Difference in thermodynamic average temperature of the solution and the heat source fluid and heat load in desorber as a function of the ratio of the temperature glide of solution to the temperature glide of the source

The sum of the booster and solution pump work as a function of the weak solution mass flow is examined in Figure 5–6. The pump work increases linearly with the mass flow of weak solution, and is only 0.75% to 1.3% relative to the power consumed by the compressor.

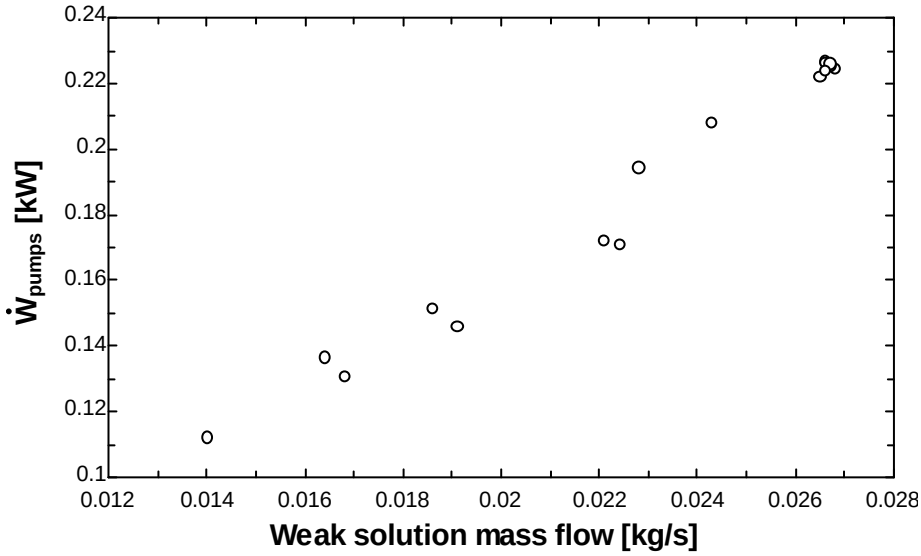

Figure 5–6: Sum of booster pump and solution pump work as a function of the weak solution mass flow.

The measured heating COP of the test plant is shown in Figure 5–7 as a function of the arithmetic mean of the differences between the thermodynamic average temperature of the solution and the heat sink and heat source fluid in the absorber and desorber respectively. The heating COP increases as the temperature differences between the solution and the heat sink/source media decreases. The best heating COP is 2.47. The measured heat load transferred to the sink is 47.5 kW, and the heat sink and heat source outlet temperature was 93° C and 17° C respectively.

The scatter in the data in Figure 5–7 are caused by (1) the mass flow of heat sink and heat source fluid being held constant (2) the rotational velocity of the solution pump varies and (3) the liquid level in the high-pressure receiver varies.

The solution liquid level in the high-pressure receiver affects the heat load transferred to the heat sink. The constant mass flow of heat sink and heat source fluid then influence the temperature lift the heat pump has to work against. The rotational velocity of the solution pump changes the ammonia concentration of the strong solution and the mass flow. The heat transfer coefficient in the absorber and desorber increases as the mass flow of solution increases, ref. Figure 5–8 and 5–10.

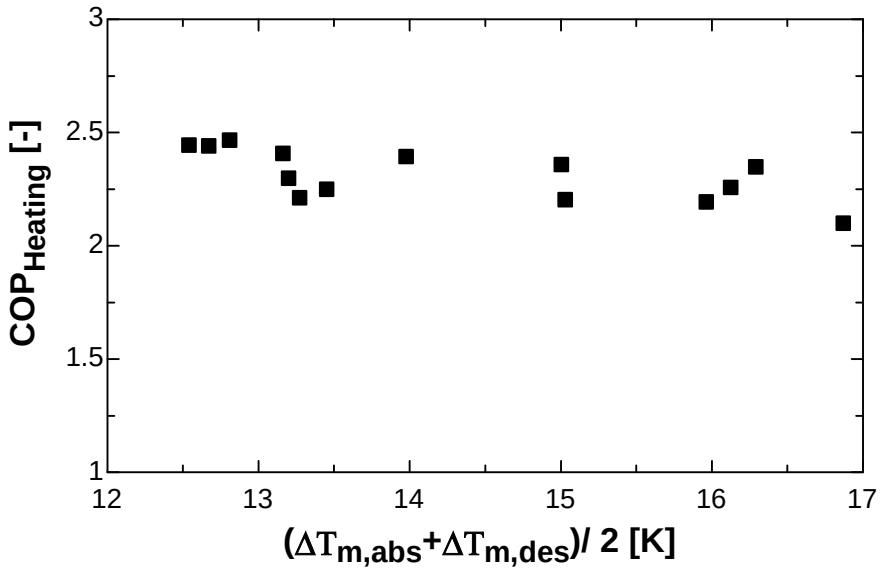

Figure 5–7: $COP_{heating}$ as a function of the arithmetic mean of the differences between the thermodynamic average temperatures in the absorber and desorber

5.2 Component performance

5.2.1 Heat exchangers

Minimization of the irreversibility involved with the heat transfer processes are of primary concern in absorption heat pumps. The advantages of the compression/ absorption heat pump depend greatly on being able to make the driving temperature difference in the absorber and desorber small.

5.2.1.1 Absorber

Figure 5–8 shows the overall heat transfer coefficient measured in absorber 1 and absorber 2 as a function of the strong solution mass flux. The heat sink mass flux was constant at 66.9kg/ m^2s in both heat exchangers. The heat flux varies when the solution composition varies. The

overall heat transfer coefficient of both absorber 1 and absorber 2 increases with increasing solution mass flux, absorber 2 more than absorber 1.

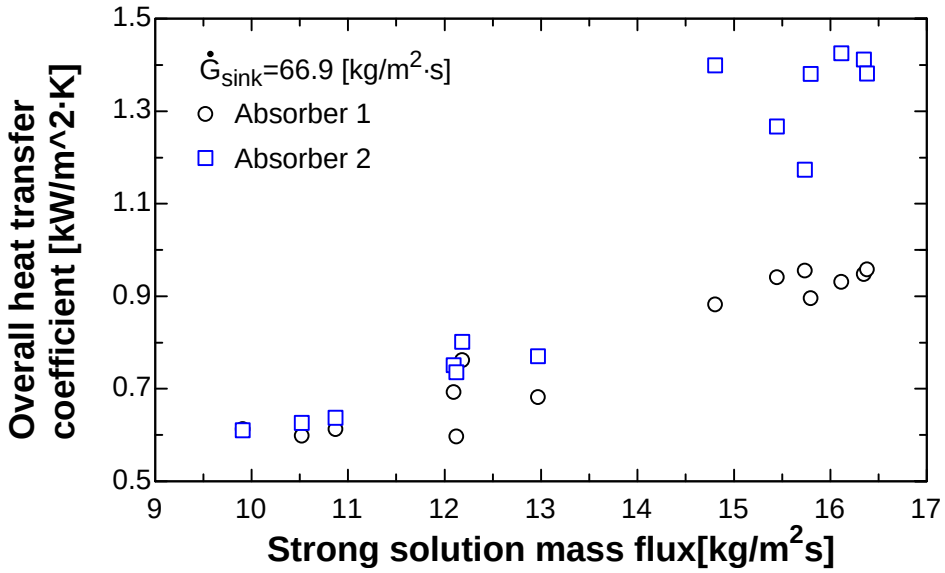

Figure 5–8: Overall heat transfer coefficient in absorber 1 and 2 as function of the strong solution mass flux

The overall heat transfer coefficient in the absorber 1 and absorber 2 as function of the heat flux is shown in Figure 5–9. The overall heat transfer coefficient of absorber 1 and absorber 2 show a linear increase as the heat flux increases. The heat flux in absorber 1 is larger than in absorber 2 at small mass fluxes as a larger part of the total absorber heat is transferred in absorber 1. As the mass flux increases more of the heat load is transferred in absorber 2.

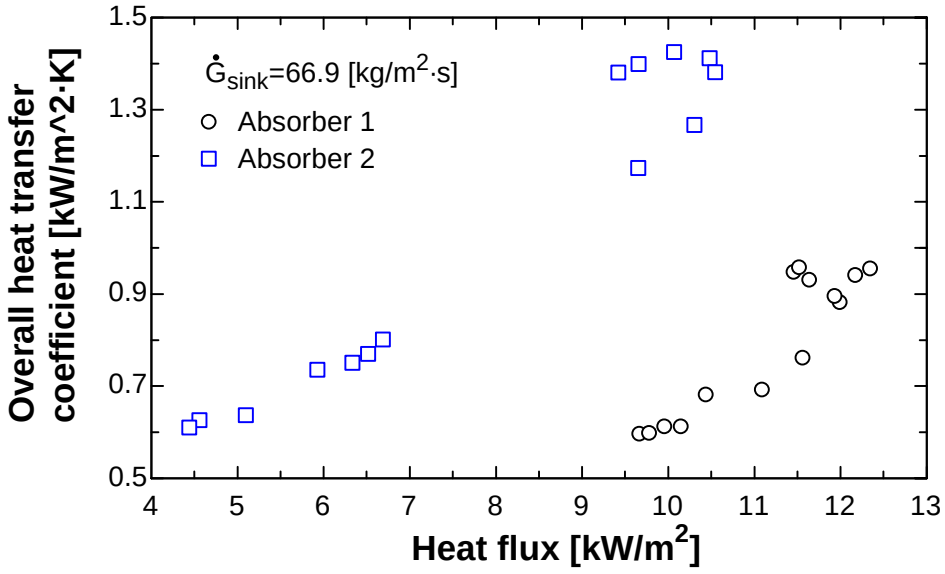

Figure 5–9: Overall heat transfer coefficient of absorber 1 and 2 as a function of heat flux

5.2.1.2 Desorber

The overall heat transfer coefficients in desorber 1 and desorber 2 are plotted a function of the strong solution mass flux in Figure 5–10, and as a function of the heat flux in Figure 5–11. The heat source mass flux was constant at 54 kg/m^{2}s. The heat flux varies in Figure 5–10 and the solution mass flux varies in Figure 5–11. The overall heat transfer coefficient in desorber 1 is larger than in desorber 2 at solution mass fluxes between 8 to 10.5 kg/m^{2}s. At solution mass fluxes larger than 12kg/m^{2}s is the overall heat transfer coefficient in desorber 2 largest.

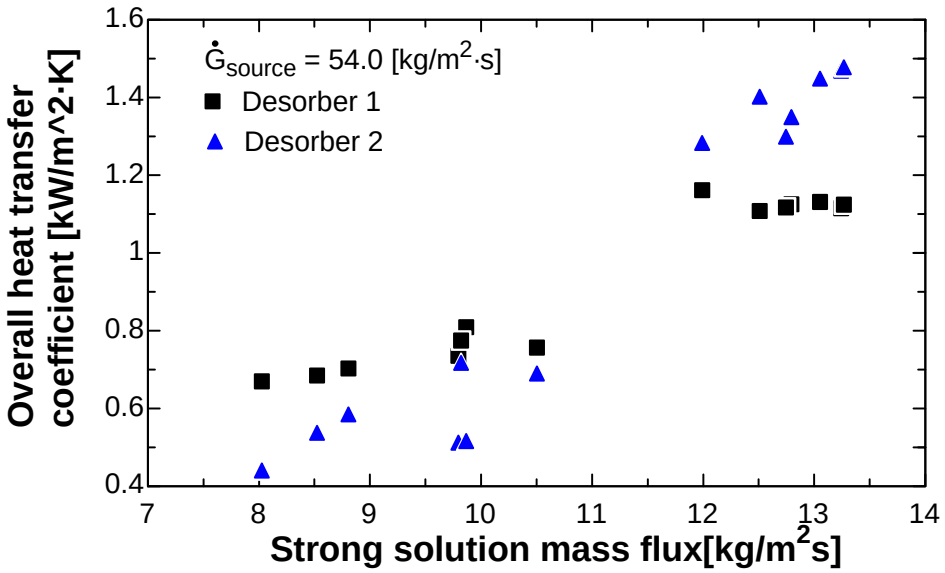

Figure 5–10: Overall heat transfer coefficient in desorber 1 and 2 as function of the strong solution mass flux

More heat is transferred in desorber 1 than desorber 2, especially at solution mass fluxes between 8 to 10.5kg/m^{2}s. The heat load in desorber 2 increases when the solution mass flux increases.

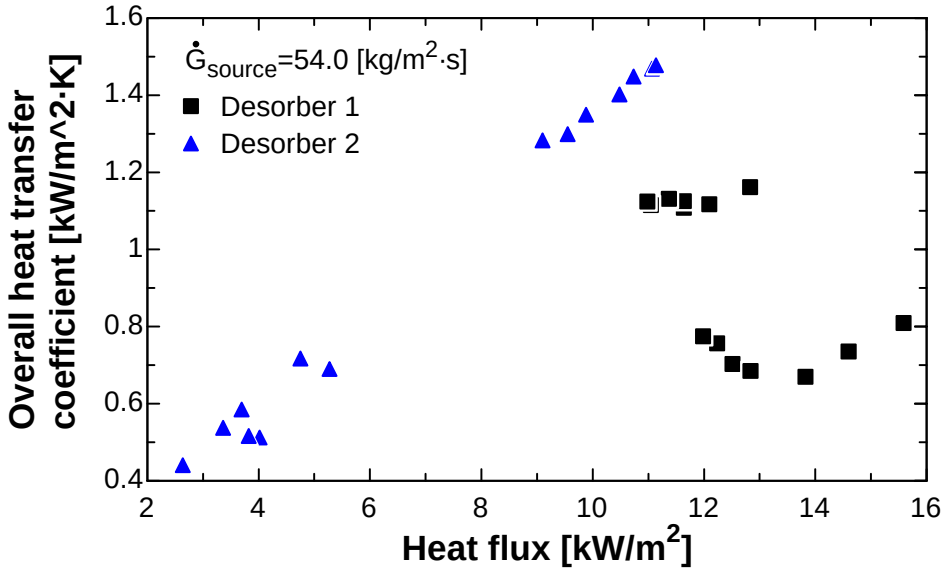

Figure 5–11: Overall heat transfer coefficient in desorber 1 and 2 as function of the strong solution mass flux

5.2.1.3 Solution heat exchangers

The overall heat transfer coefficient in solution heat exchanger 1 correlate best with the Reynolds number of the strong solution, see Figure 5–12. The measured heat transfer coefficients are between 2.7 and 3.1 kW/m^{2}K. The approach temperature on the hot side of the heat exchanger was between 5 and 7 ° C.

The overall heat transfer coefficient in solution heat exchanger 2 is shown as a function of the weak solution Reynolds number in Figure 5–13. The measured heat transfer coefficient was between 0.15 and 0.28 kW/m^{2}K. The approach temperature on the cold side of the heat exchanger was between 5 and 11 ° C.

.

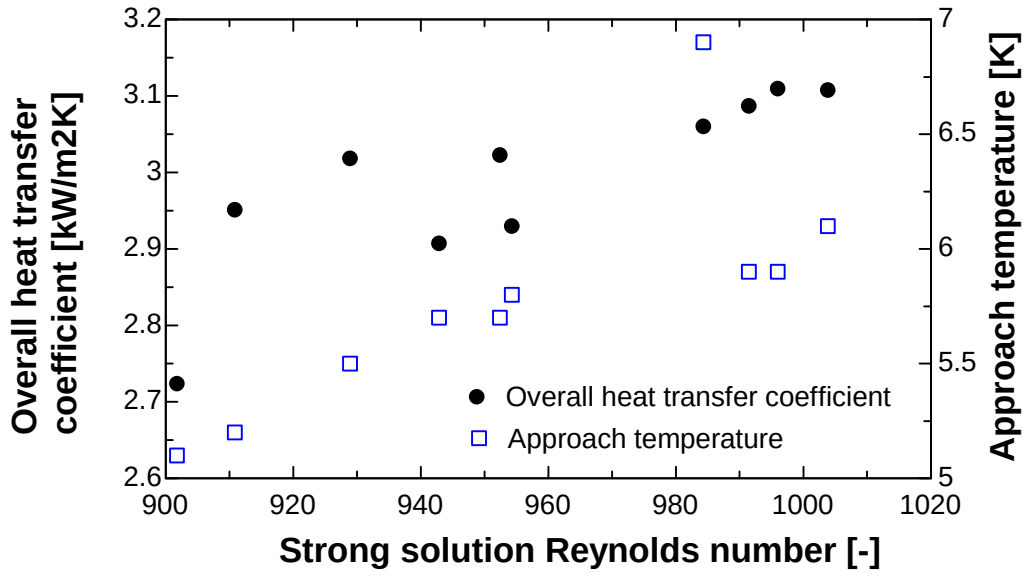

Figure 5–12: Overall heat transfer coefficient and approach temperature in solution heat exchanger 1 as a function of the strong solution Reynolds number

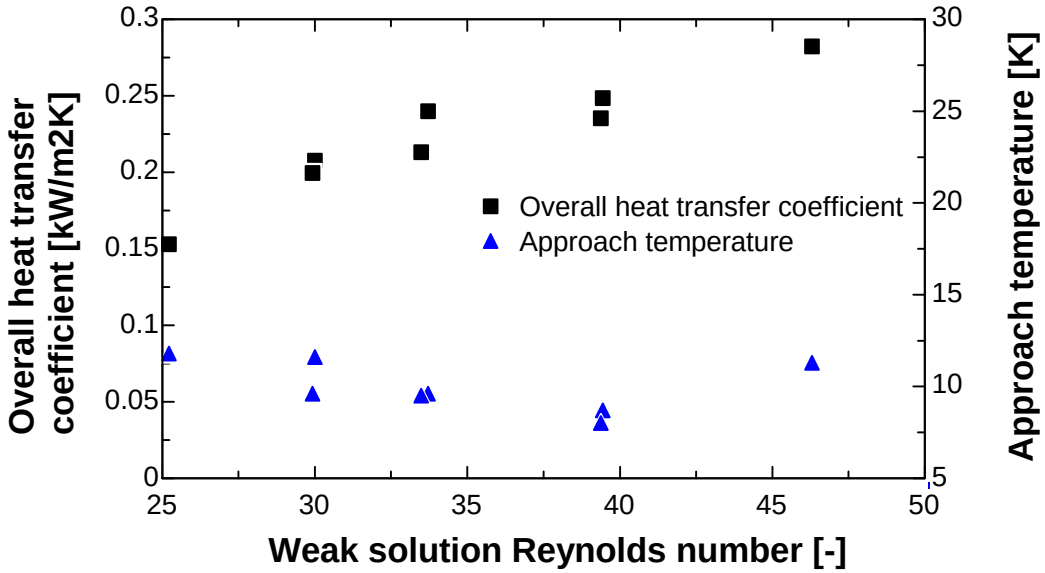

Figure 5–13: Overall heat transfer coefficient and approach temperature in solution heat exchanger 2 as a function of the weak solution Reynolds number

5.2.1.4 Desuperheater

Figure 5–14 shows the overall heat transfer coefficient in the desuperheater as a function of the vapour Reynolds number. The mass flow of heat sink fluid is constant. The measured heat transfer coefficient varies between 1 to 1.75 kW/m^{2}K. The approach temperature at the cold side of the heat exchanger was between 7 and 12 ° C.

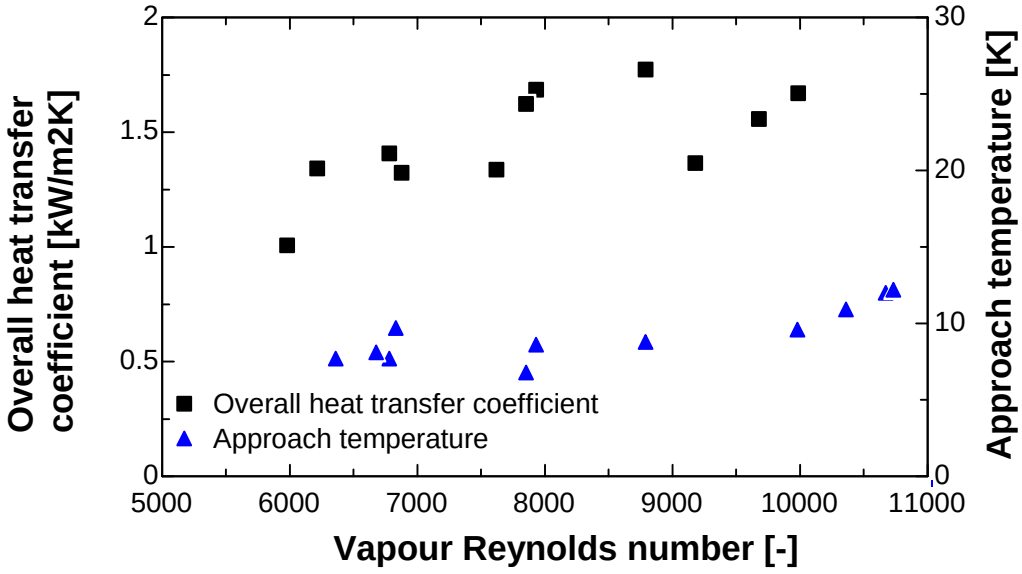

Figure 5–14: Overall heat transfer coefficient and approach temperature in the desuperheater as a function of the vapour Reynolds number

5.2.2 Compressor

5.2.2.1 Lubrication

During the initial experiments large amounts of liquid solution was observed in the oil separator after the solution heat exchanger 2 and in the oil separator after the desuperheater after a few hours of operation. The magnetic valves in the oil return lines from the oil separators at the compressor intermediate and high -pressure outlet was then kept closed during the experiments. This was done to prevent ammonia/water mixture coming into the oil sump of the compressors, as this may cause the oil pump to cavitate with the risk of compressor failure.

Samples from the oil sump have been taken, and no alarming amount of water was found. The water content was below 100ppm.

The oil temperature in the compressor oil sump during operation of the CAHP was held at 80 °C to reduce the amount of dissolved ammonia in the oil in the oil sump.

5.2.2.2 Cylinder head cooling

The compressor cylinder head cooling inlet temperature varied from 45 °C to 50 °C. This relatively high inlet temperature was chosen to produce useful heat and to limit the chance of condensation of water in the compressor. The outlet temperature was 60 °C to 65 °C. The mass flow of cooling water was adjusted to limit the compressor discharge temperature. The ratio between the compressor cylinder cooling heat load and the compressor shaft work is shown in Figure 5–15 (a) as a function of the pressure ratio across the compressor. The cooling heat load

was 20% to 35% of the compressor shaft work dependent of the pressure ratio across the compressor.

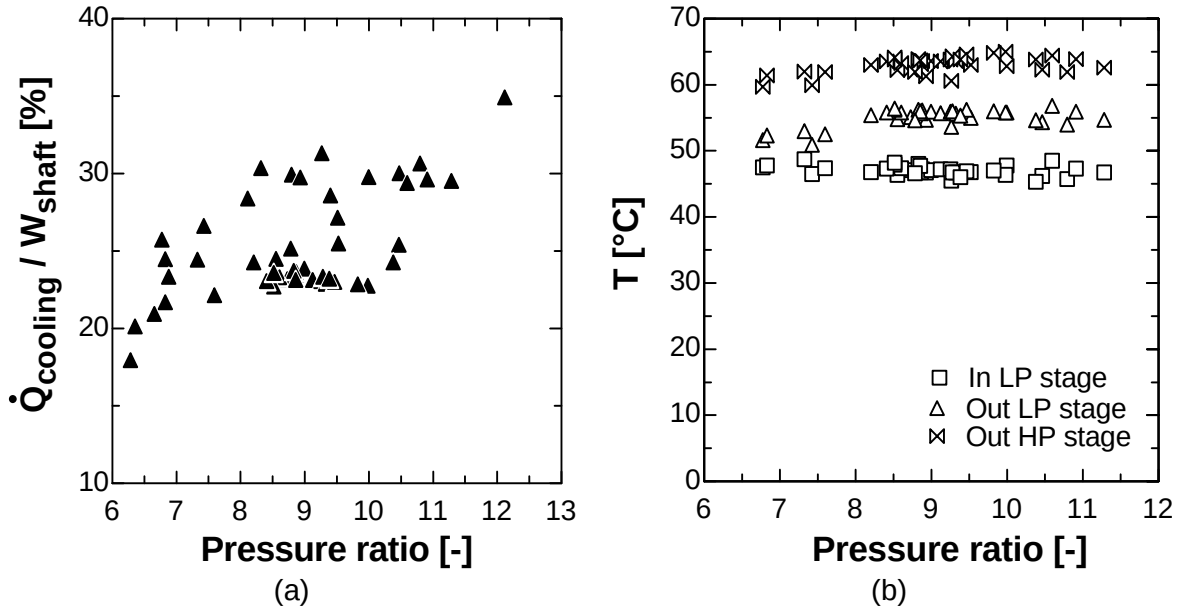

Figure 5–15: Compressor cylinder head cooling as a function of the pressure ratio across the compressor

5.2.2.3 Volumetric and isentropic efficiency

The volumetric efficiency of the low-pressure and high-pressure stage of the compressor is shown in Figure 5–16. The volumetric efficiency of the low-pressure stage was constant at a value of 72% for a pressure ratio ranging from 2.63 to 2.76. The volumetric efficiency at the high-pressure stage decreased from 84% to 80% as the pressure ratio increased from 3.1 to 3.9.

Figure 5–17 shows the compressor isentropic efficiency found in the experiments. The measured isentropic efficiency decreases from 74% to 71% when the pressure ratio increases from 8.2 to 10.6.

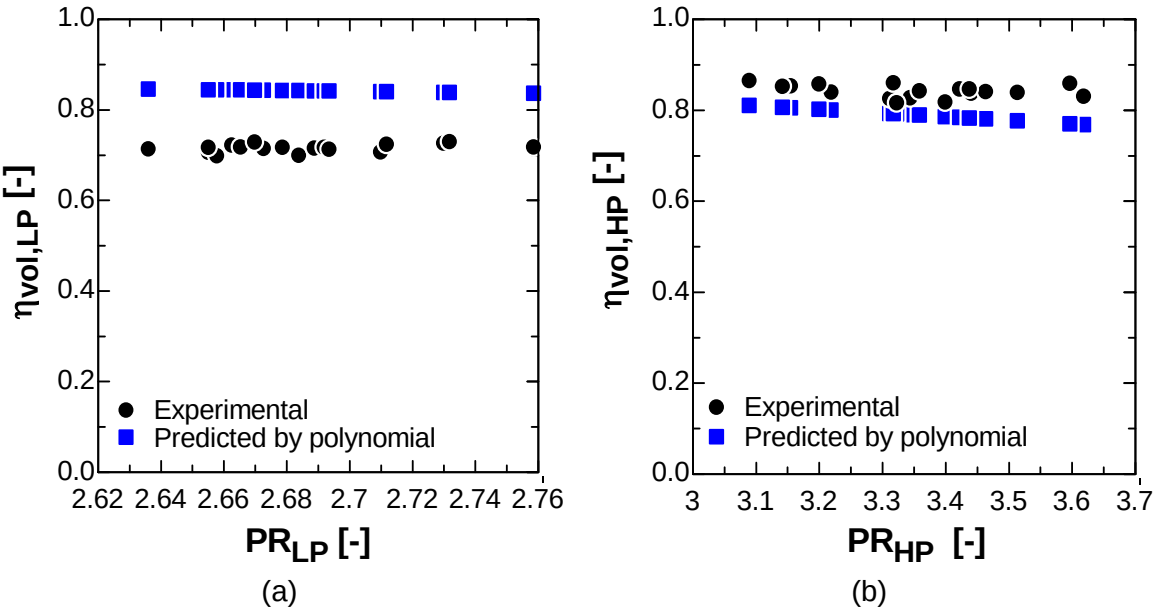

Figure 5–16: Predicted and experimental volumetric efficiency as a function of the pressure ratio across the low-pressure stage and the high-pressure stage of the compressor

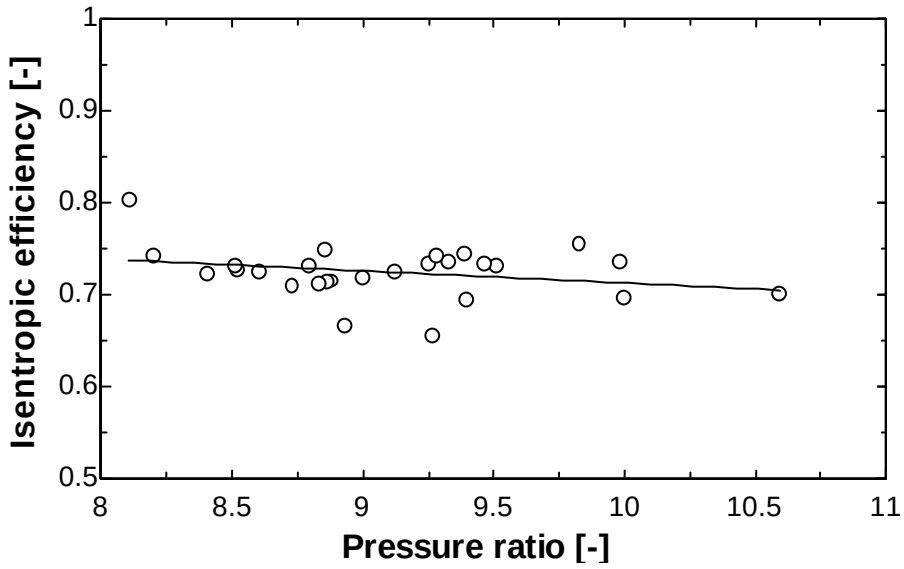

Figure 5–17: Experimental isentropic efficiency as a function of the pressure ratio across the compressor

5.3 Losses

5.3.1 Heat losses

It could be anticipated that the high discharge temperatures at the high-pressure stage during the experimental tests would lead to significant heat losses to the environment, thus reducing the potential for heat transfer to the heat sink. In Figure 5–18 the level of heat losses are examined. The heat delivered to the heat sink was 0.85 to 0.99 of the combined heat and work inputs in the desorber and compressor.

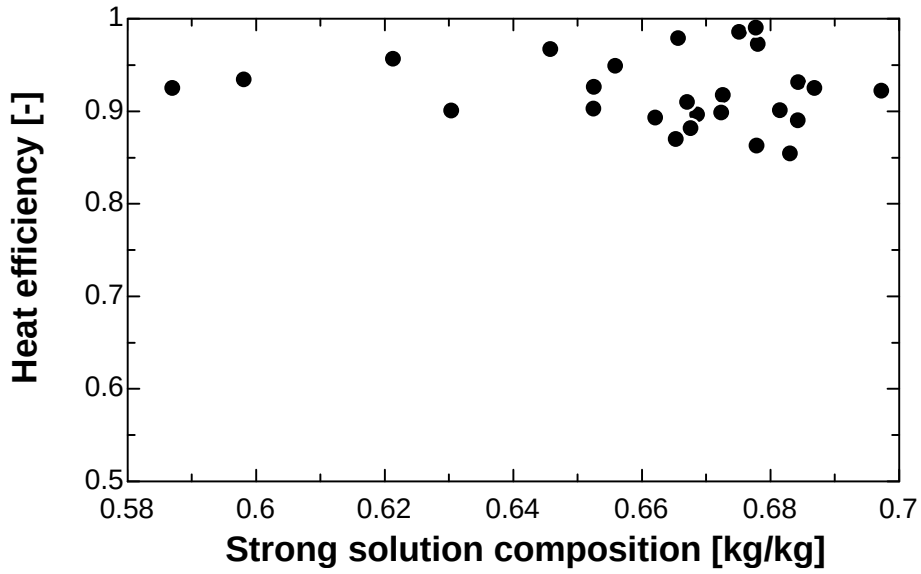

Figure 5–18: Heat efficiency as function of the ammonia concentration in the strong solution

5.3.2 Pressure losses

The pressure losses in the system reveal a potential for improvements in the heat pump design. The pressure losses in the absorber and desorber as a function of the mixture mass flow are shown in Figure 5–19 (a) and (b). The pressure losses in the absorber and desorber are of the same magnitude, i.e. the pressure loss increased from 0.05 to 0.23 bar when the mixture mass flow increased from 0.04 to 0.06 kg/s. Figure 5–19 (c) shows the pressure loss from the compressor high-pressure stage outlet to the absorber 1 inlet, i.e. the sum of the pressure losses in the desuperheater and vapour distributor. The sum of the pressure loss in the desuperheater and the vapour distributor increased from 0.28bar to 0.6bar when the vapour mass flow increased from 0.016kg/s to 0.032 kg/s.

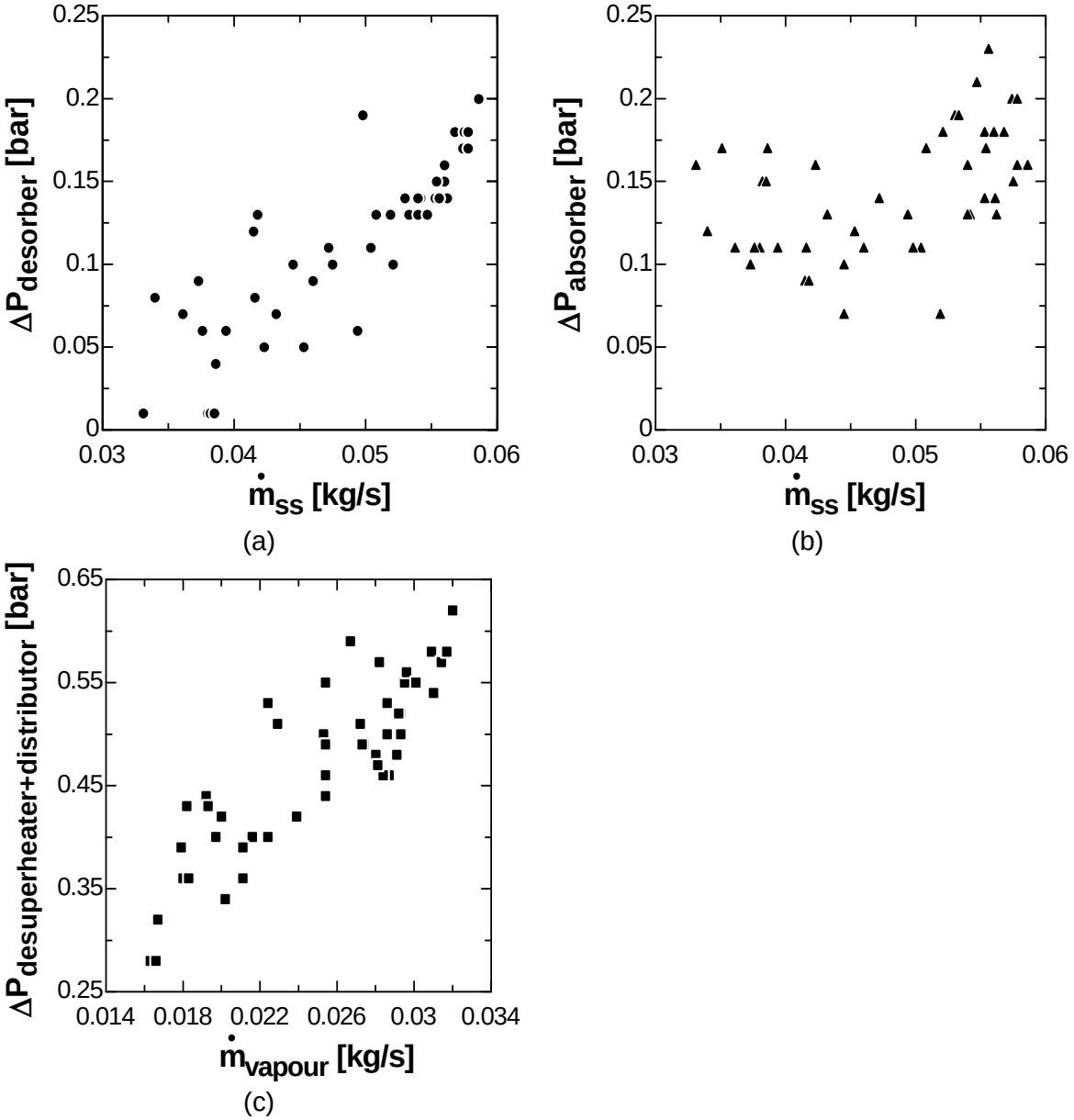

Figure 5–19: Pressure losses in (a) the absorber, (b) the desorber and (c) the desuperheater and vapour distributor.

5.4 Validation of the design models

5.4.1 Compressor

A combined two-stage compressor is difficult to model. The compressor in the test unit has been modelled with polynomials representing the volumetric and isentropic efficiency. Figure 5–16 shows a comparison between the experimental values and predicted values of the volumetric efficiency for the low-pressure and high-pressure stage. The predicted values for the volumetric efficiency at the low-pressure stage was 80-81% for a pressure ratio from 2.63 to

2.76, while the experimental volumetric efficiency was 72%. At the high-pressure stage the experimental values for the volumetric efficiency show the same decreasing trend with increasing pressure ratio as the predicted values. The experimental volumetric efficiency at the high-pressure stage was 10% to 20% higher than the predicted value.

The polynomials for the isentropic efficiency were determined for the separate stages. No comparison with experimental values is then possible.

5.4.2 Absorber

The heat exchanger model explained in chapter 3.7 has been modified in order to perform a comparison with the experimental values. The measured test conditions at the weak solution and vapour and heat sink inlet were supplied as inputs to the model.

5.4.2.1 Overall heat transfer coefficient

Figure 5–20 shows a comparison of the predicted and the experimental overall heat transfer coefficient of absorber 1 as function of the mass flux of strong solution. The predicted overall heat transfer coefficient is calculated as the ratio of the predicted heat load to the product of the heat transfer area and the predicted logarithmic mean temperature difference. This was done as the experimental heat transfer coefficient was calculated using the logarithmic mean temperature difference. The mass flux on the secondary side of the absorber was constant during the experiments. The predicted heat transfer coefficient is from 2.2 to 2.5 times the experimental heat transfer coefficient.

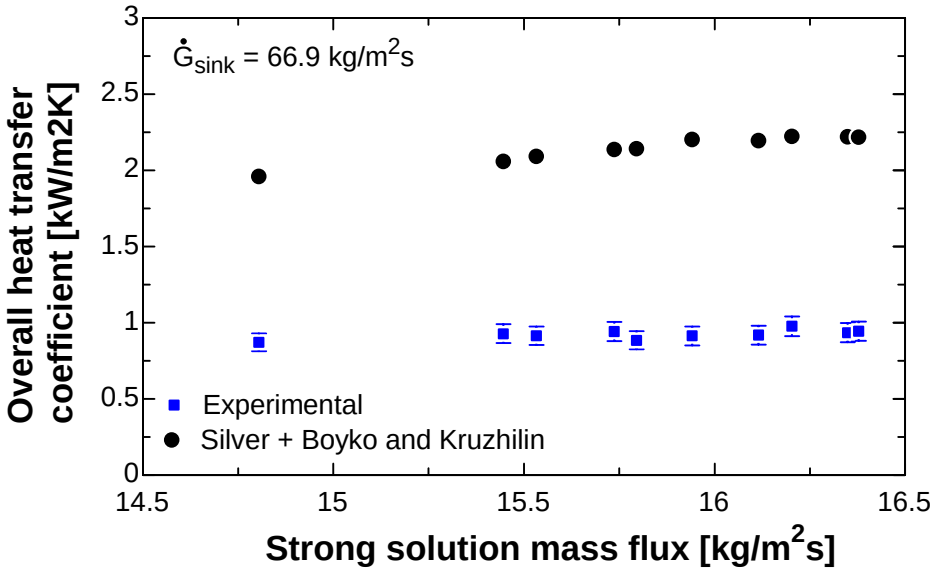

Figure 5–20: Overall heat transfer coefficient of absorber 1 as a function of the strong solution mass flux

The high prediction of the heat transfer coefficient shown for absorber 1 led to problems with the model validation for absorber 2 due to temperature crossing at the absorber 2 outlets.

5.4.2.2 Pressure drop

Figure 5–21 shows a comparison of the predicted pressure drop and the experimental values. The experimental pressure drop was up to 2 times the predicted pressure drop.

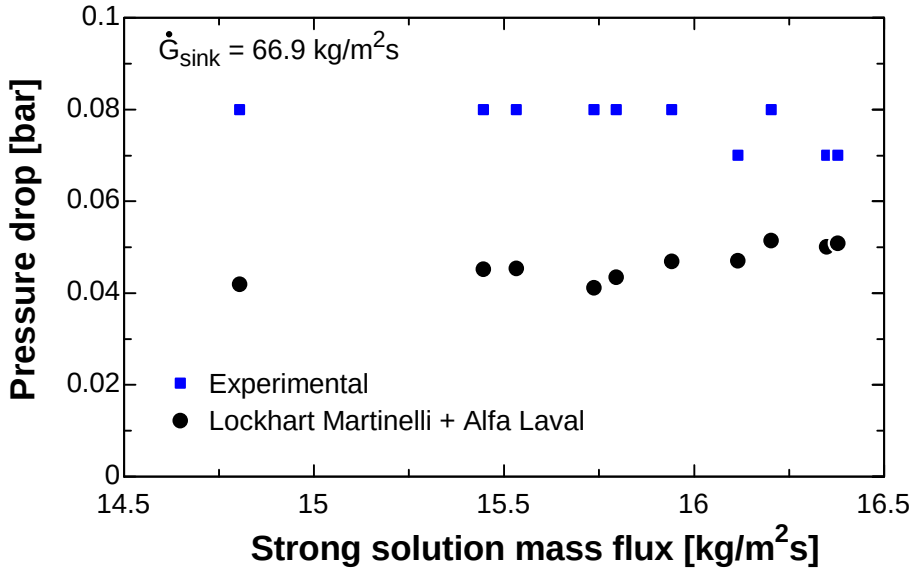

Figure 5–21: Pressure drop in absorber 1 as a function of the strong solution mass flux

5.4.3 Desorber

5.4.3.1 Overall heat transfer coefficient

The predicted overall heat transfer coefficient and the measured overall heat transfer coefficient is shown in Figure 5–22 versus solution mass flux and in Figure 5–23 versus the heat flux. The predicted overall heat transfer coefficient is calculated as the ratio of the predicted heat load to the product of the heat transfer area and the predicted logarithmic mean temperature difference for the same reasons as given for the absorber. The heat flux varies in Figure 5–22 and the solution mass flux varies in Figure 5–23. The design model predicts 3.2 to 3.9 times higher values for the overall heat transfer coefficient in the desorber than the experimental values.

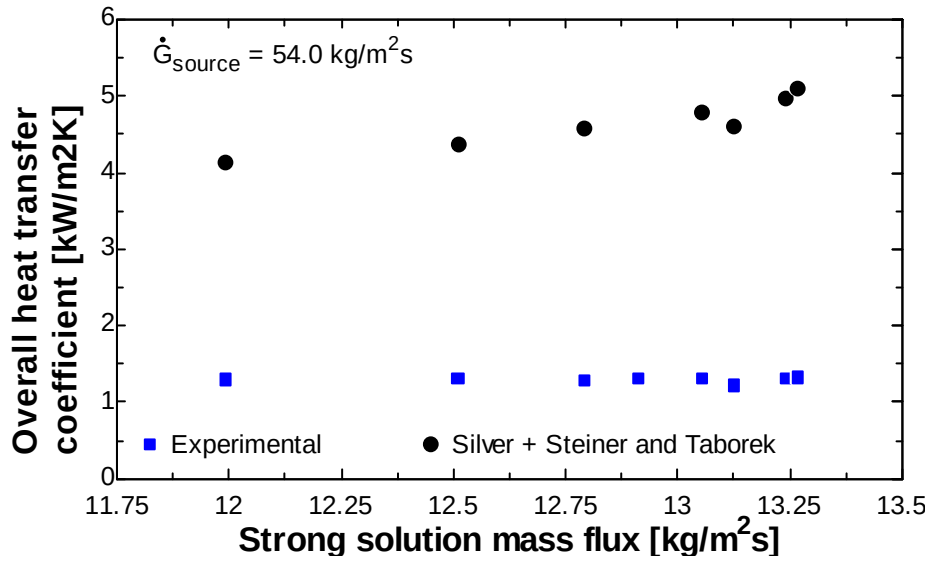

Figure 5–22: Overall heat transfer coefficient in desorber as a function of strong solution mass flux

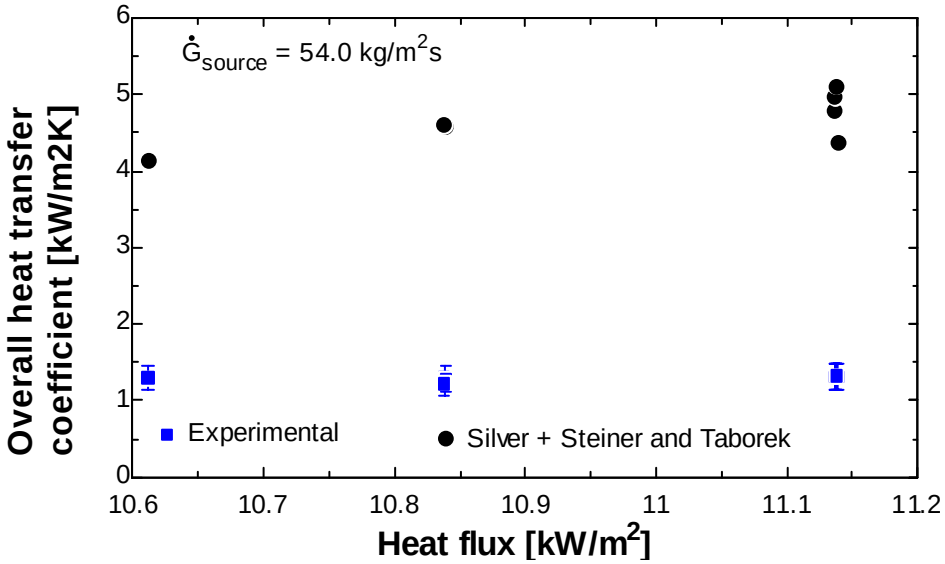

Figure 5–23: Overall heat transfer coefficient in the desorber as a function of the heat flux

5.4.3.2 Pressure drop

The predicted pressure loss in the desorber is compared with the measured pressure loss in Figure 5–24. The predicted pressure loss is 2 times higher than the measured pressure loss across the desorber.

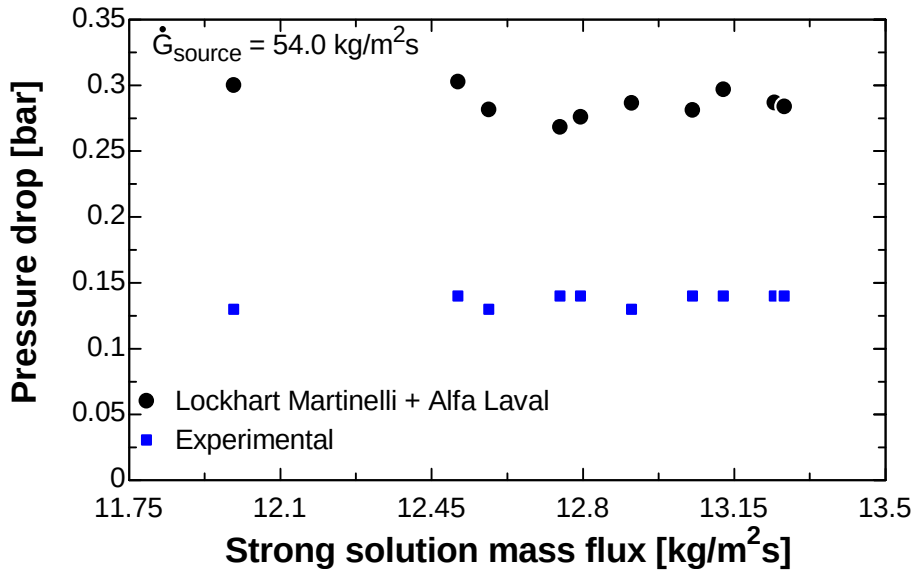

Figure 5–24: Pressure drop in the desorber as a function of the strong solution mass flux

5.4.4 CAHP model

The objective of the mathematical model described in chapter 3 was to design the laboratory test unit. Comparison is then difficult, but it is worth trying to validate the computer calculations using the experimental results.

The laboratory heat pump experience several losses compared to the theoretical model used as design basis.

The following assumptions are made in the theoretical model:

- The frictional pressure losses in the system are neglected.
- The efficiency of the compressor electrical motor is 92%.
- The compressor cylinder head cooling is set to 5% of the compressor shaft work.
- The volumetric efficiency of the compressor is given by the polynomial in Equation 3.2 on page 31.

An examination of the experimental results revealed significant pressure losses in the desuperheater and vapour distributor as shown in Figure 5–19. The electrical motor driving the compressor in the laboratory has low efficiency. The motor efficiency was measured to 81% using a torque gauge (strain gauge) early in the project. The compressor cylinder head cooling was measured to be up to 30% of the compressor shaft work in the experiments. The volumetric efficiency polynomial predicted too high values at the low-pressure stage.

In Figure 5–25 the experimental values are used as input to the mathematical model and corrected for each of these losses, resulting in 22% higher values for the $COP_{heating}$. The motor efficiency is most important, contributing to an increase of the $COP_{heating}$ of 13.6%.

The ammonia concentration in the weak solution was used as an input parameter to the model to take into consideration the effect of the liquid level in the high-pressure receiver. The volumetric efficiency at the low-pressure stage was set to 72%.

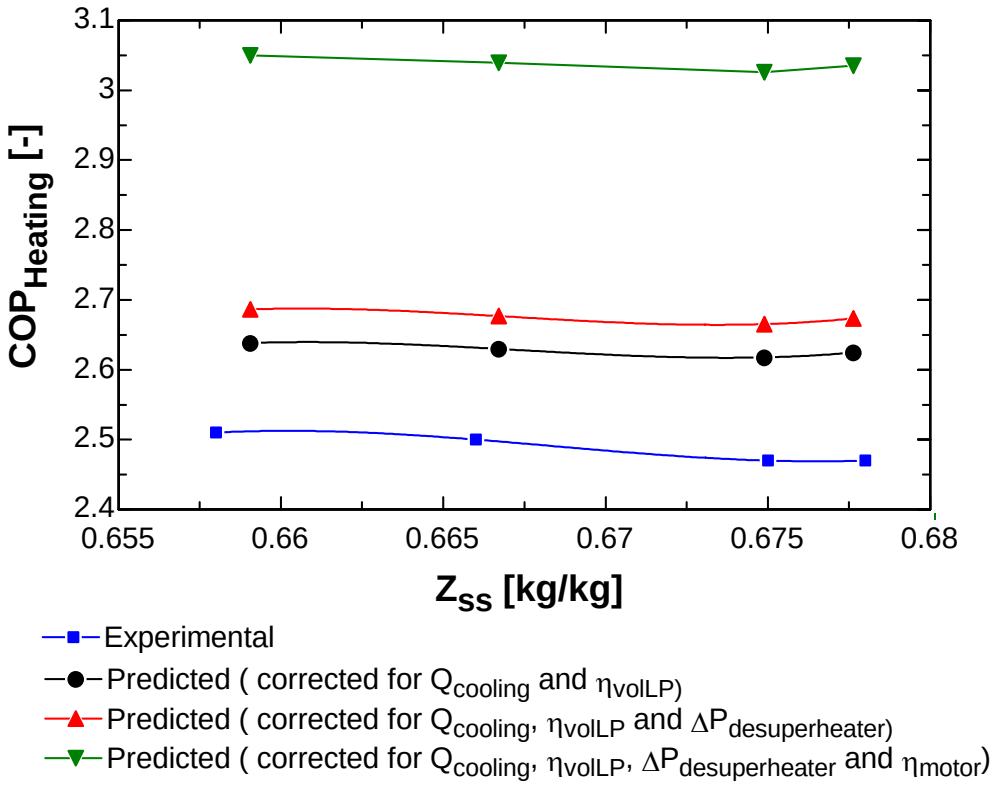

Figure 5–25: Predicted $COP_{heating}$ as a function of ammonia concentration in the strong solution

Additional losses are detected in the absorber and desorber heat exchange. The heat losses from heat pump are not taken into account in the model.

6 Discussion of Experimental Investigation

6.1 Overall performance

The experiments have shown that the CAHP can be operated in a stable and secure way. A heating COP of 2.47 was measured for the case of heating water from 50 to 93 °C, and at the same time chilling water from 50 to 17 °C.

The heat sink and heat source load increases as more of the refrigerant charge is transferred from the high-pressure receiver to the low-pressure separator. The vapour pressure in the low-pressure separator increases and consequently the vapour mass flow rate through the compressor increases. More ammonia is put into the solution circuit and the composition and mass flow of the circulating strong solution increases. The significant increase of the heat load is a result of the increased amount of vapour that has to be absorbed.

The measured heating COP values are somewhat lower than expected from simulations. The main reasons for the lower $COP_{heating}$ values can be traced back to several losses in the test plant:

- subcooling of the weak solution at absorber inlet,
- large pressure drop on the high-pressure vapour side,
- the measured volumetric efficiency of the compressor low-pressure stage is lower than the predicted volumetric efficiency,
- the measured compressor cylinder head cooling heat load is larger than assumed in the simulations,
- the measured overall heat transfer coefficient in the absorber and desorber is lower than expected.
- the efficiency of the electric motor driving the compressor is lower than assumed in the simulation.

Before useful heat rejection can occur in the absorber the weak solution needs to be heated above the heat rejection temperature. It is better to do this by heat exchange rather than by adiabatic absorption because the absorption raises the concentration of the weak solution and reduces the maximum available equilibrium temperature. The absorber inlet temperature affects the driving temperature difference for heat exchange in the absorber. Increased driving temperature difference give reduced pressure if the heat load is constant. Solution heat exchanger 1 and 2 provides internal heat recovery in the solution circuit. Solution heat exchanger 2 heats the weak solution going to the absorber, and chills the vapour at intermediate pressure. Cooling of the vapour at intermediate stage reduces the work input at the compressor high-pressure stage, and reduces the vapour discharge temperature. Solution heat

exchanger 1 provides precooling of the strong solution and preheating of the weak solution. The precooling of the strong solution reduces the flash losses in the expansion valve. The measured subcooling of the weak solution at the solution heat exchanger 2 outlet is 44 to 55 °C, resulting in a significant reduction of the heat rejection temperature. The measured heat load in solution exchanger 1 and solution heat exchanger 2 was from 0.6 to 1.8kW, and from 1.6 to 3.34kW, respectively. The vapour temperature at the low-pressure compressor outlet is lower than the design conditions for solution heat exchanger 2, giving a lower driving temperature difference for heat exchange and hence a lower heat load.

The pressure drop in the desuperheater and vapour distributor increases the compressor work and therefore directly influence the heating COP.

The volumetric efficiency of the low-pressure stage affects the vapour flow rate through the compressor. A lower volumetric efficiency then gives a lower absorber heat load as the amount of latent heat decreases. The heating COP is less affected by the decreased volumetric efficiency.

The necessary cylinder head cooling load to keep the vapour discharge temperature down was larger than anticipated, thus decreasing the heat delivered to the heat sink. The vapour discharge temperature also influences the amount of oil dissolved in the vapour phase, as the amount of dissolved oil in the vapour is a function of the temperature. The vapour temperature can be reduced by increasing the ammonia concentration in the solution circuit when keeping the heat sink inlet and outlet temperature constant. Increasing the average ammonia concentration gives a reduction of the pressure ratio. The vapour discharge temperature can also be reduced if two separate compressors is used. The intermediate pressure can then be adjusted to the optimal for a two-stage compression. More of the compressor work can the be done by the low-pressure stage, thus decreasing the compressor discharge temperature at the high-pressure stage.

The losses in the absorber and desorber limit the heat transfer in the absorber and desorber and therefore influence the heating COP. The performance of the desorber and absorber has a significant influence on the heat pump performance. The overall heat transfer coefficients in the absorber and desorber are sensitive to the solution mass flow rate. The solution temperature glide in the absorber and desorber varies when the mass flow of weak solution is altered. A reduction of the mass flow of weak solution resulted in a decrease of the heat transfer coefficient in the desorber. The suction pressure decreased resulting in a lower mass flow rate of vapour. The heat sink load decreased and the pressure ratio increased leading to a poorer heating COP.

6.2 Compressor Performance

The vapour temperature at the high-pressure discharge varied between 135 °C to 155 °C. At the low-pressure stage the discharge temperature was around 100 °C. The cooling water mass

flow to the compressor cylinder heads was adjusted to keep the vapour discharge temperature down. The cooling heat load was not included in the calculation of the heating COP. The cooling heat load was up to 35% of the compressor shaft work dependant of the pressure ratio across the compressor, giving a significant reduction of the heating COP. In the design model the compressor cylinder head cooling was assumed to be 5% of the shaft work. The extra cooling heat load corresponds to a reduction of the heating COP of 5.9 to 9.3% compared to the design model.

An increase of the composition of the solution increases the pressures at constant temperatures. Increasing the suction pressure decreases the specific work input and the vapour discharge temperature as the isentropes are steeper at higher pressures.

The magnetic valves in the oil return lines from the oil separators at the intermediate and high- pressure discharge was kept closed during the experiments. This was done as precaution to avoid water coming into the oil sump. The water content in the vapour is a function of the temperature, pressure and composition of the working fluid in the low-pressure receiver. At lower capacities the water content in the vapour increases as the desorber pressure decreases and the solution temperature at the desorber outlet increases. Increased water content in the vapour together with lower mass flow rates of vapour resulted

6.3 Heat exchangers

6.3.1 Absorber

The composition and mass flow rate of strong solution increases as the composition of the liquid in the low-pressure receiver increases. Increasing the ammonia content in the strong solution increases the vapour mass fraction at the desorber outlet and the absorber inlet. The solution mass flow has the largest effect on the performance of the absorber. The absorber is solution side limited, as illustrated by the increased overall heat transfer coefficient with an increase in solution flow rate. The heat transfer coefficient on the heat sink side varies relatively little since the water mass flow rate was kept constant.

Because the absorber is solution-side limited, any improvement in the solution-side flow distribution, surface wetting, and the corresponding increase in thermal conductance should increase the overall performance of the absorber.

Heat flux and concentration are linked together as adjusting the composition varies the heating capacity. The viscosity and flow rate have a large influence on the Reynolds number or turbulence of the solution. The viscosity of the liquid solution decreases as the composition increases.

The surface tension of the solution is also a function of the concentration. The surface tension and solution flow rate has a significant influence on the surface wetting of the heat exchanger area. The surface tension decreases with increasing concentration of ammonia.

The measured overall heat transfer coefficient in the absorber is considerably lower than the predicted overall heat transfer coefficient. Probable reasons for this deviation are:

- incomplete surface wetting
- the effect of an oil film on the heat transfer surface
- the mass transfer resistance on the solution side

To account for potential solution distribution and inadequate wetting problems, a correction factor in the form of an area effectiveness ratio, $R = A_{eff}/A_{actual}$, was utilized. The ratio R was varied in the model until the predicted heat load matched the corresponding measured values. The value of the area effectiveness ratio required achieving correspondence between model and experiment varied from 0.27 to 0.32. These values seems low given the small number of channels in the absorber.

The effect of an oil film on the overall heat transfer coefficient can be predicted as shown in Equation 6.1.

$$U = \left(\frac{1}{\alpha_w} + R_f + \frac{1}{\alpha_{eff,\,cond}}\right) \tag{6.1}$$

where α_w is the local heat transfer coefficient on the heat sink fluid side, R_f is the thermal resistance in the oil film, and $\alpha_{eff,\,cond}$ is the effective condensation heat transfer coefficient on the solution side. The thermal resistance in the oil film is predicted as:

$$R_f = \delta_{film}/k_{oil} \tag{6.2}$$

where δ_{film} is the thickness of the oil film, and k_{oil} is the thermal conductivity of the oil. The thermal conductivity of the oil is 0.1415 W/mK (Svendsen [62]).

A representative value for the calculated average heat transfer coefficient on the mixture side and on the heat sink fluid side is 4.84kW/m^{2}K and 7.88kW/m^{2}K respectively. Using these values the degradation of the heat transfer coefficient caused by the oil film is calculated. Figure 6–1 shows the calculated degradation of the overall heat transfer coefficient as a function of the oil film thickness. The effect of an oil film is strong. The degradation of the overall heat transfer coefficient increase from 17% to 68% when the thickness of the oil film increase from 0.01mm to 0.1mm.

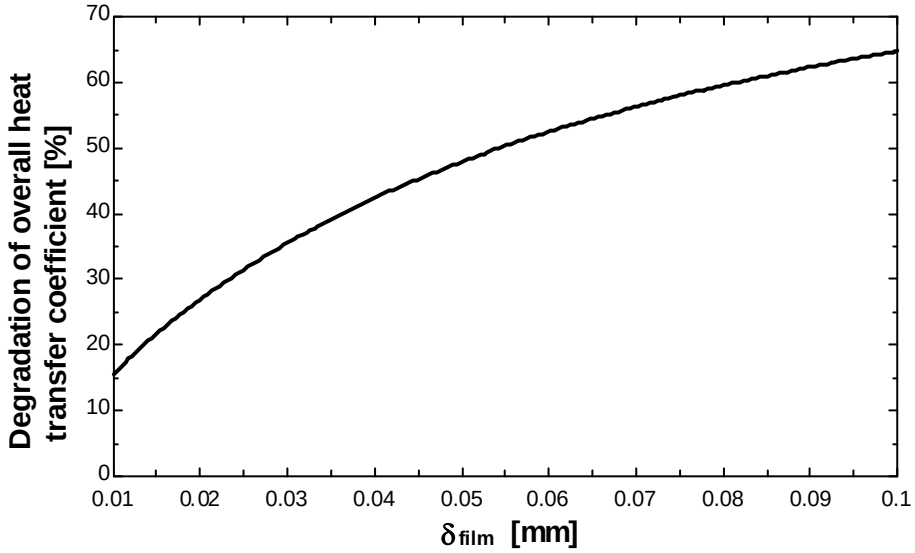

Figure 6–1: Effect of an oil film on the predicted overall heat transfer coefficient in the absorber as a function of the oil film thickness.

A plate heat exchanger has very complicated flow geometry with sudden contractions and changes in flow direction. This may keep the two phases of the working fluid mixture well mixed: The mass transfer resistance in the liquid film was neglected in the model, and the mass transfer resistance in the vapour was taken into account with the Ackermann factor. The experimental data can be compared with a Colburn and Drew type model as this is assumed to be more accurate.

The combined effect of incomplete surface wetting and an oil film on the heat transfer surface gives a likely explanation to the large deviations between the measurements and the model predictions. The effects of the mass transfer resistance in the vapour phase needs better understanding. The mathematical model needs better verification. Experiments with a single channel heat exchanger would eliminate the uncertainty with the distribution of the solution into the channels. The uncertainty with the distribution of the solution across the heat exchanger plate will remain. The effect of an oil film also need to be studied more closely.

6.3.2 Desorber

The measured overall heat transfer coefficients of the desorber are considerably lower than the predicted values. The vapour mass fraction at the desorber outlet increases with increasing ammonia concentration in the solution. A larger vapour mass fraction normally give a larger heat transfer coefficient. At low solution flow rates the overall heat transfer coefficient decreases with increasing ammonia concentration in the solution. At higher solution flow rates the overall heat transfer coefficient increases with increasing ammonia concentration. The flow pattern is apparently bad at small solution flow rates.

The reasons for the deviations between the model predictions and the experimental values for the overall heat transfer coefficient in the desorber are the same as for the absorber.

The effect of incomplete wetting of the heat transfer surface and the effect of an oil film was studied using the same method as for the absorber. The value of the area effectiveness ratio required achieving correspondence between model and experiment varied from 0.28 to 0.30. Figure 6–2 shows the degradation of the overall heat transfer coefficient in the desorber as a function of the oil film thickness. The reduction of the overall heat transfer coefficient is 16% for an oil film with a thickness of 0.01mm, and increases to 65% for an oil film thickness of 0.1mm.

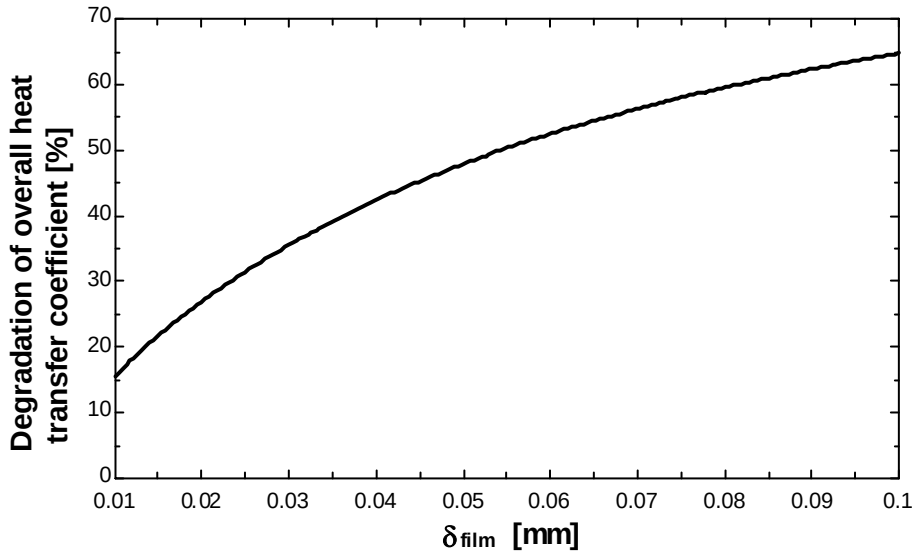

Figure 6–2: Effect of an oil film on the predicted overall heat transfer coefficient in the desorber as a function of the oil film thickness.

The effect of the mass transfer resistance in the vapour phase was neglected in the model. A Colburn and Drew type model can be used to take the mass transfer in the vapour phase into account.

The desorber model also needs better verification using experiments on a single channel heat exchanger to remove the effect of poor solution distribution among the channels in the plate hear exchanger.

7 Conclusions and Suggestions for Further Work

7.1 Conclusions

The following conclusions are derived, based on the work described in this thesis:

- A laboratory compression/absorption heat pump is designed and built. Experimental results obtained in this work suggest further investigation of compression/absorption heat pumps.
- A heating COP of 2.47 for a heat sink outlet temperature of 93° C was achieved. The heat source outlet temperature was 17° C. The heat sink and heat source inlet temperature was 50° C.
- The experimental results proved that capacity control could be achieved by adjusting the composition in the solution circuit. An optimization of the system charge is required.
- The operation of the CAHP test unit revealed the need for careful design of solution heat exchanger 2 and the desuperheater to prevent condensation in these heat exchangers.
- Plate heat exchangers were used a heat exchange devices in the experimental test unit. The overall heat transfer coefficient in the absorber and desorber was lower than expected. The dominating thermal resistance was on the solution side. The part load behaviour was poor.
- An optimization of the $COP_{heating}$ for a specific case will involve an adjustment of the composition in the solution circuit, and an adjustment of the temperature glide with the flow ratio between the vapour mass flow and the mass flow of weak solution.
- The two-stage compressor is not optimal for use in the compression/absorption system. Use of separate compressors for the high- and low-pressure stage make optimization of the intermediate pressure possible. This will decrease the work input and the vapour discharge temperature at the high-pressure stage.

7.2 Suggestions for Further Work

Based on the work performed in this thesis, the following are suggested for further work on compression/ absorption heat pumps:

General:

- Investigate the heat- and mass transfer characteristics in single channel plate heat exchanger. This will remove the uncertainty about distribution problems of the two-

phase mixture among the heat exchanger channels. The distribution across the heat exchanger surface still remains.

- Develop better correlations for prediction of the transport properties of ammonia-water mixtures. The effect of uncertainties in the estimation of the transport properties should be investigated.
- The influence of lubrication oil on the heat transfer characteristics needs investigation as the high vapour discharge temperatures increase the amount of dissolved oil.

Test unit:

- Install a drain line for oil recovery from the high-pressure receiver. The oil can be drained from the bottom of the receiver, as the oil is heavier than the liquid ammonia-water mixture.
- Means to reduce the amount of water in the vapour at the compressor suction inlet should be found to increase the heat load in the solution heat exchanger 2. The weak solution temperature increases and the absorber heat load increases.
- The vapour superheat at the high-pressure stage can be transferred to the weak solution coming from the solution heat exchanger 2 instead of the heat sink fluid. This will reduce the risk of condensation in the desuperheater.
- Use of two separate compressor units in the laboratory unit. In this way the intermediate pressure can be optimised and the compressor work reduced. The vapour discharge temperatures will also decrease. The cooling heat load can then be reduced.
- The solution flows upwards in the bubble absorber (absorber 1). Compressor lubrication oil can then accumulate in this heat exchanger. Counter-current flow on the solution side, with the liquid solution flowing downwards and the vapour flowing upwards, is difficult to manage in a plate heat exchanger. Therefore, the absorber 1 should be tested as a falling film device.
- Reduction of the pressure losses in the vapour circuit.

Bibliography

1. Alefeld, G. and R. Radermacher, *Heat conversion systems*. 1994: CRC Press Inc
2. Osenbrück, A., *Verfahren zur Kälteerzeugung bei Absorptionsmachinen,* in *Kaiserliches Patentamt*. 1895: Germany
3. Altenkirch, E., *Kompressionskältemachine mit Lösungskreislauf.* Kältetechnik, 1950. 2(10): 251-259; 2(11): 279-284; 2(12): 310-315.
4. Altenkirch, E., *Der Einfluß endlicher Temperaturdifferenzen aud die Betriebskosten von Kompressionskälteanlagen mit und ohne Lösungskreislauf.* Kältetechnik, 1951. 3(8):201-205; 3(9): 229-234; 3(10): 255-259
5. Morawetz, E., *Sorption-Compression Heat Pumps.* International Journal of Energy Research, 1989. 13: p. 83-102.
6. Ziegler, F., *Kompression-Absorptions-Wärmepumpen,* in *Forchungsberichte des Deutchen Kälte- und Klimatechnischen Vereins, Nr. 34*. 1991: Stuttgart.
7. Åhlby, L., *The compression/absorption heat pump cycle - system simulations*, in *Department of Heat and Power Technology.* 1992, Chalmers University of Technology: Göteborg, Sweden.
8. Groll, E.A. *Current status of absorption/compression cycle technology.* in *Proceedings of the 1997 ASHRAE Winter Meeting*. 1997. Philadelphia: ASHRAE
9. Itard, L.C.M., *Wet compression-resorption heat pump cycles: Thermodynamic analysis and design*, in *Laboratory of Refrigerating Engineering and Indoor Climate Technology.* 1998, Delft University of Technology: Delft
10. Brunin, O., *Pompe à chaleur à compression-absorption: Etude et réalisation expérimentale*, in *Méchanique Energétique*. 1995, Henry Poincaré: Nancy.
11. Bercescu, V. *Aspects du fonctionnement d'une installation experimentale de pompe de chaleur avec compression mecanique et circulation additionelle de la solution.* in *Preprints to the 16th International Congress of Refrigeration*. 1983. Paris.
12. Mucic, V. and B. Scheuermann, *2-Stoff-Kompressions-Wärmepumpe mit Lösungskreislauf. Versuchanlage Mannheim-Waldof.* 1984, BMFT Forschungsbericht BMFT-FB-T-84-197.
13. Stokar, M. and C. Trepp, *Compression heat pump with solution circuit Part 1: design and experimental results.* International Journal of Refrigeration, 1987. **10**: p. 87-96.
14. Malewski, W.F. *Integrated Absorption and Compression Heat Pump Cycle using Mixed Working Fluid Ammonia and Water.* in *Proceedings of the Inst. of Refrigeration 1987-1988*. 1988. London.
15. Mucic, V., *Resorption Compression Heat Pump with Solution Circuit for Steam Generation Using Waste Heat of Industry as Heat Source*, in *Newsletter of the IEA Heat*

Pump Center. 1989. p. 14-15.

16. Bergmann, G. and G. Hivessy. *Experimental hybrid heat pump of 1000kW heating capacity.* in *Proceedings of the 4th International Conference on Application and Efficiency of Heat Pump Systems in Environmentally Sensitive Times*. 1990. Munich, Germany.
17. Rane, M.V., *Experimental investigation of two-stage vapor compression heat pump with solution circuit*, in *Department of Mechanical Engineering*. 1991, University of Maryland, College Park.
18. Torstensson, H. and J.E. Nowacki, *Sorptions/kompressionvärmepump, slutrapport*. 1990, Studsvik Energy.
19. Groll, E.A. and R. Radermacher. *Vapor compression heat pump with solution circuit and desorber/absorber heat exchange*. in *Proceeding of the International Absorption Heat Pump Conference*. 1994. New Orleans.
20. Itard, L.C.M. and C.H.M. Machielsen, *Considerations When Modeling Compression Resorption Heat-Pumps.* International Journal of Refrigeration-Revue Internationale Du Froid, 1994. **17**(7): p. 453-460.
21. Hewitt, N.J., et al., *Advanced cycles and replacement working fluids in heat pumps.* Applied Thermal Engineering, 2001. **21**(2): p. 237-248
22. Heidelck, R. and H. Kruse. *Use of Commercial Compressors for Absorption/ Compression Heat Pumps with Ammonia-Water.* in *Heat Pumps - a Benefit for the Environment, 6th IEA Heat Pump Conference*. 1999. Berlin, Germany.
23. Mongey, B., et al., *Performance trends and heat transfer considerations in an ammonia-water resorption cycle.* International Journal of Energy Research, 2001. **25**(1): p. 41-5.
24. Ziegler, F., *State of the art in sorption heat pumping and cooling technologies.* International Journal of Refrigeration, 2002. **25**(4): p. 450-459
25. Hulten, M., *The compression/absorption heat pump - modelling and comparisons*, in *Department of Heat and Power.* 1999, Chalmers University of Technology: Göteborg.
26. Hulten, M. and T. Berntsson, *The compression/absorption cycle - influence of some major parameters on COP and a comparison with the compression cycle.* International Journal of Refrigeration, 1999. **22**(2): p. 91-106.
27. Hulten, M. and T. Berntsson, *The compression/absorption heat pump cycle--conceptual design improvements and comparisons with the compression cycle.* International Journal of Refrigeration, 2002. **25**(4): p. 487-497.
28. Berntsson, T., K. M. Berntsson, et al. (1985). *Heat transfer of nonazeotropic mixtures in a falling film evaporator.* ASHRAE Annual Meeting, Honolulu, ASHRAE Transactions.
29. Klein, S.A. and F.L. Alvarado, *EES - Engineering Equation Solver.* 1998, F-Chart Software: 4406 Fox Bluff Rd., Middelton, WI 55562

30. Tillner-Roth, R. and G. Roth, *AWMix 1.0*. 1998: Weinheim, Germany

31. Tillner-Roth, R. and D.G. Friend, *Helmholtz free energy formulation of the thermodynamic properties of the mixture {water plus ammonia}.* Journal of Physical and Chemical Reference Data, 1998. **27**(1): p. 63-96.

32. Harr, Gallagher, and Kell, *NBS/NRC Steam Tables*. 1984, Hemisphere Publishing Co.

33. Moran, M.J. and H.N. Shapiro, *Fundamentals of engineering thermodynamics*. 3 ed. 1998: Wiley.

34. Silver, L., *Gas cooling with aqueous condensation.* Trans. Inst. Chem. Eng., 1947. **25**: p. 30-42.

35. Bell, K.J. and M.A. Ghaly, *An approximate generalized design method for multicomponent/partial condensers.* AIChE Symp. Ser., 1973. **69**(131): p. 72-79.

36. Price, B.J. and K.J. Bell, *Design of binary vapor condensers using the Colburn-Drew equations.* AIChE Symp. Ser., 1974. **70**(138): p. 163-171.

37. Boyko, L.D. and G.N. Kruzhilin, *Heat transfer and hydraulic resistance during condensation of steam in a horisontal tube and in a bundle of tubes.* International Journal of Heat and Mass Transfer, 1967. **10**: p. 361-373.

38. Panchal, C.B. *Condensation heat transfer in plate heat exchangers*. in *ASME, HTD - Two-phase heat exchanger.* 1985. Denver.

39. Sardesai, R.G., R.A.W. Shock, and D. Butterworth, *Heat and mass transfer in multicomponent condensation and boiling.* Heat Transfer Engineering, 1982. **3**(3-4): p. 104-114.

40. Thome, J.R., *Boiling of new refrigerants: a state-of-the-art review.* International Journal of Refrigeration, 1996. **19**(7): p. 435-457

41. Stephan, K., *Two-phase heat exchange for new refrigerants and their mixtures.* International Journal of Refrigeration, 1995. **18**(3): p. 198-209.

42. Jung, D. and R. Radermacher, *Prediction of Evaporation Heat Transfer Coefficient and Pressure Drop of Refrigerant Mixtures.* International Journal of Refrigeration, 1993. **16**(5): p. 330-338.

43. Steiner, D. and J. Taborek, *Flow Boiling Heat-Transfer in Vertical Tubes Correlated by an Asymptotic Model.* Heat Transfer Engineering, 1992. **13**(2): p. 43-69.

44. Gnielinski, V., *New Equations for Heat and Mass-Transfer in Turbulent Pipe and Channel Flow.* International Chemical Engineering, 1976. **16**(2): p. 359-368

45. Colburn, A.P. and T.B. Drew, Trans. AIChE, 1937. **33**.

46. Thome, J.R. and S. Shakir, *A new correlation for nucleate boiling of aqueous mixtures.* AIChE Symp. Ser., 1987. **83**(257): p. 46-51.

47. Thonon, B., R. Vidil, and C. Marvillet, *Recent Research and Developments in Plate*

Heat-Exchangers. Journal of Enhanced Heat Transfer, 1995. **2**(1-2): p. 149-155.

48. Thonon, B., *Plate Heat-Exchangers - 10 Years of Research at Greth .1. Flow Pattern and Heat-Transfer in Single-Phase and 2-Phase Flows.* Revue Generale De Thermique, 1995. **34**(397): p. 77-90.
49. Thonon, B. and P. Mercier, *Plate heat exchangers: Ten years of research at GREThh .2. Sizing and flow maldistribution.* Revue Generale De Thermique, 1996. **35**(416): p. 561-568.
50. Thonon, B., A. Feldman, L. Margat, and C. Marvillet,, *Transition from nucleate boiling to convective boiling in compact heat exchangers.* International Journal of Refrigeration, 1997. **20**(8): p. 592-597.
51. Kang, Y.T., A. Akisawa, and T. Kashiwagi, *Analytical investigation of two different absorption modes: falling film and bubble types.* International Journal of Refrigeration, 2000. **23**(6): p. 430-443.
52. Baksaas, H.S. and S. Grandum. *Initial tests of high temperature absorption /compression heat pump*. in *Proceedings of the International Heat Pump Conference*. 1999. Munich, Germany
53. Sveine, T., S. Grandum, and H.S. Baksaas. *Design of high temperature absorption/ compression heat pump*. in *Natural Working Fluids, IIR - Gustav Lorentzen conference*. 1998. Oslo, Norway
54. Taylor B.N. and Kuyatt, C.E., *Guidelines for Evaluating and Expressing the Uncertainty of NIST Measurement Results*, National Institute of Standards and Technology Technical Note 1297, 1994
55. IIR, *Thermophysical properties of Liquid Secondary Refrigerants*. IIR Handbook on secondary refrigerants, ed. Å. Melinder. 1997, Paris.
56. Laesecke, A., *Personal communication*. 2001
57. Thorin, E., *Thermophysical properties of ammonia-water mixtures for prediction of heat transfer areas in power cycles.* International Journal of Thermophysics, 2001. **22**(1): p. 201-214
58. Reid, R.C., J.M. Prausnitz, and B.E. Poling, *The properties of gases & liquids*. 4 ed. Chemical Engineering Series. 1987: McGraw-Hill.
59. IIR, *Thermodynamic and physical properties of NH3-H2O*. Tables and diagrammes for the refrigeration industry. 1994.
60. Plank, R., *Handbuch der Kältetechnik*. 1988: Springer-Verlag.
61. CAS2000 Ver.3.7, June 2001.
62. Svendsen, Pål V., Esso Norge AS/ Mobil Norge AS, Personal communication, Jan. 2005.

Appendix

.

A Thermophysical Properties for Ammonia/Water

Thermodynamic properties

The equation of state given by Tillner-Roth and Friend [31] is the latest comprehensive equation of state for ammonia-water. The equation of state is based on a fundamental equation of state for the Helmholtz free energy $A = U - T \cdot S$, and the entire thermodynamic space of the mixture is described by one single equation. This is formed by the fundamental equations of state of the pure components and a mixing rule for the independent variables, reduced temperature and reduced density. The term for the departure from non-ideal mixture behaviour is fitted to the most reliable, available experimental data for the ammonia-water mixture. Equation A.1 show the formulation:

$$\frac{\bar{A}}{R_m \cdot T} = \Phi = \Phi^o(\tau^o, \delta^o, x) + \Phi^r(\tau, \delta, x) \qquad \text{(A.1)}$$

Φ is split into an ideal part Φ^o and a residual part Φ^r. $\bar{A}$ is the molar Helmholtz free energy, $R_m = 8.314471 Jmol^{-1}K^{-1}$ is the universal gas constant and T is the temperature i Kelvin.

The reference values values for enthalpy (or internal energy) and entropy are set to

$$u = 0 \qquad and \qquad s = 0$$

for saturated liquid at the triple point temperatures of both pure components, 273.16 K for water and 195.495 K for ammonia.

The equation of state is incorporated into the computer code AWMix© [30] that is a dynamic link library to be used together with the EES© (Engineering Equation Solver) [29] program by F-Chart software.

Typical uncertainties in the single phase regions are stated as $\pm 0.3\,\%$ for the density and $\pm 200 Jmol^{-1}$ for enthalpy. The vapour-liquid equilibrium properties are represented with an uncertainty of $\pm 0.01\,\%$ in liquid and vapour mole fractions, except in the victinity of the critical point, where it can increase to 0.04%.

Transport properties

The transport properties are the viscosity, the thermal conductivity and the diffusion coefficient. Related to the transport of momentum, heat and mass in the fluid, respectively. The viscosity and the thermal conductivity of the fluids are always needed when heat transfer processes between two flowing fluids are described. Mass transfer processes can be of importance when the condensation and evaporation of mixtures are involved, since the vapour and liquid phases during these processes have different compositions.

There exist almost no experimental data for transport properties of ammonia-water. According to Dr. Laesecke at the National Institute of Standards and Technology [56] , the the available calculation methods are without exception inadequate to predict the transport properties of ammonia-water.

Thorin [57] studied the influence of different correlations for transport properties on the heat transfer area of the heat exchangers in a Kalina power cycle and found differences up to 10% in the predicted heat transfer area for the individual heat exchangers.

Dynamic viscosity

The liquid viscosity is predicted by a correlation given in Handbuch der Kältechnik[60] :

$$\log\log(\eta + 1) = \frac{2000}{500 + T} - 4.41 + 0.925 \cdot X_l - 1.743 \cdot X_l^{\,2} + 0.021 \cdot X_l^{\,3} \qquad \left[10^{-3}\frac{kg}{ms}\right] \quad \text{(A.2)}$$

The vapour dynamic viscosity is predicted by the method of Reichenberg et al as given in Reid et al[58] .

Thermal conductivity

The liquid thermal conductivity is predicted by the Fillipov correlation as given in Reid et al. [58] :

$$\lambda_{mix,\,liquid} = Qu_g \cdot \lambda_{NH3} + (1 - Qu_g) \cdot \lambda_{H2O} - 0.72 \cdot Qu_g \cdot (1 - Qu_g) \cdot (\lambda_{H2O} - \lambda_{NH3}) \quad \text{(A.3)}$$

The parameter 0.72 may be replaced by an adjustable parameter if binary mixture data are available.

The vapour thermal conductivity is predicted by the correlation presented by El-Sayed (Thorin[57]):

$$\mu_m = \frac{\mu_{NH3} \cdot x_{NH3}}{x_{NH3} + F_{12} \cdot x_{water}} + \frac{\mu_{water} \cdot x_{water}}{x_{water} + F_{21} \cdot x_{NH3}} \quad \text{(A.4)}$$

where

$$F_{12} = \frac{[1 + (\mu_{NH3}/\mu_{water})^{0.5} \cdot (M_{water}/M_{NH3})^{0.25}]^2}{[8 \cdot (1 + (M_{NH3}/M_{water}))]^{0.5}} \quad \text{(A.5)}$$

and

$$F_{21} = F_{12} \cdot (\mu_{NH3}/\mu_{water}) \cdot (M_{NH3}/M_{water}) \quad \text{(A.6)}$$

M is the molar mass, x is the mole fraction and μ is the dynamic viscosity.

Surface tension

The surface tension is predicted by a polynomial fit to the data given in the IIR booklet, Thermodynamic and physical properties for NH3-H2O[59] . The fitted polynomial is given by Equation A.7.

$$\sigma = 0.042205 - 0.032504 \cdot X - 0.046048 \cdot X^2 - 0.13299 \cdot X^3 - 0.075618 \cdot X^4 \quad \text{(A.7)}$$

Since the experimental data for the transport properties of ammonia-water mixtures is very scarce, it is difficult to estimate the uncertainties of the calculations of the properties.

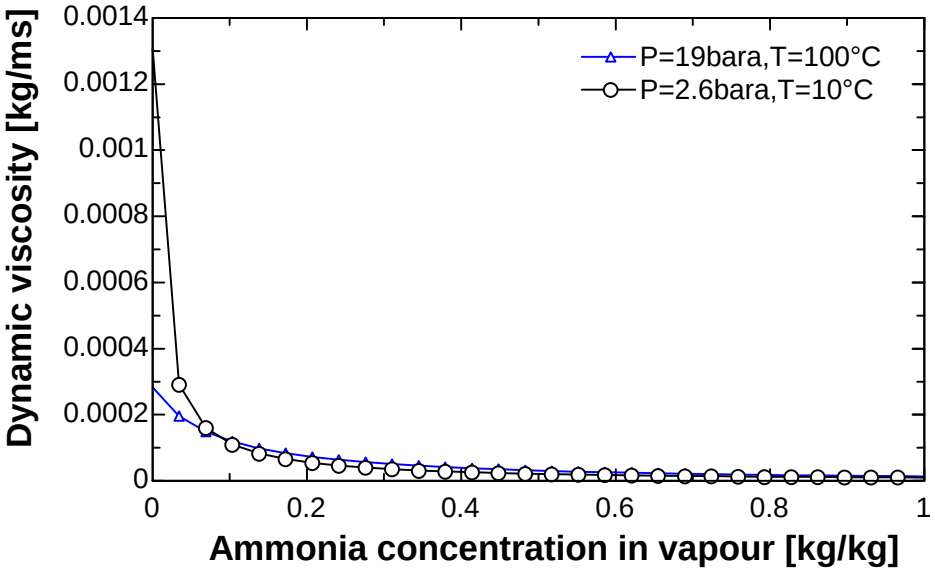

Figure A–1: Vapour dynamic viscosity as a function of ammonia concentration.

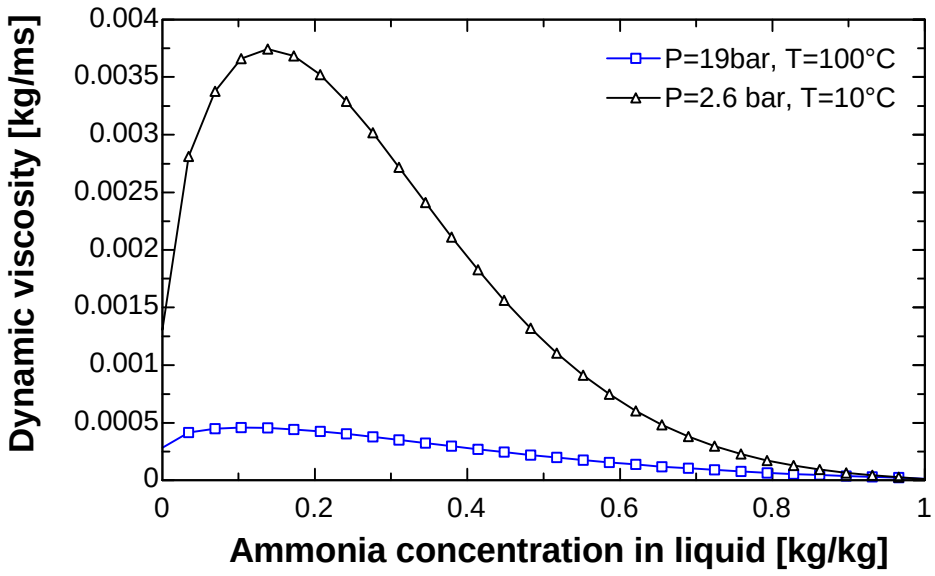

Figure A–2: Liquid dynamic viscosity as a function of the ammonia concentration

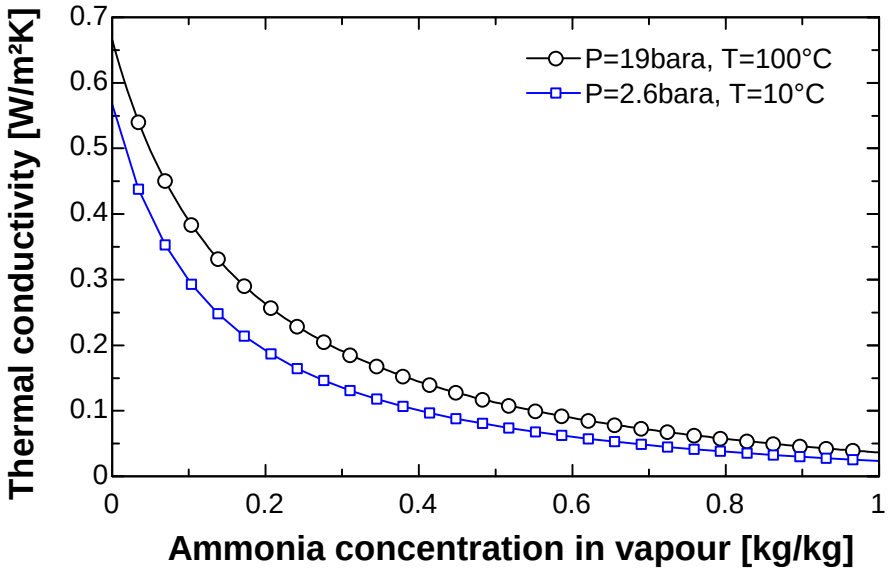

Figure A–3: Vapour thermal conductivity as a function of the ammonia concentration

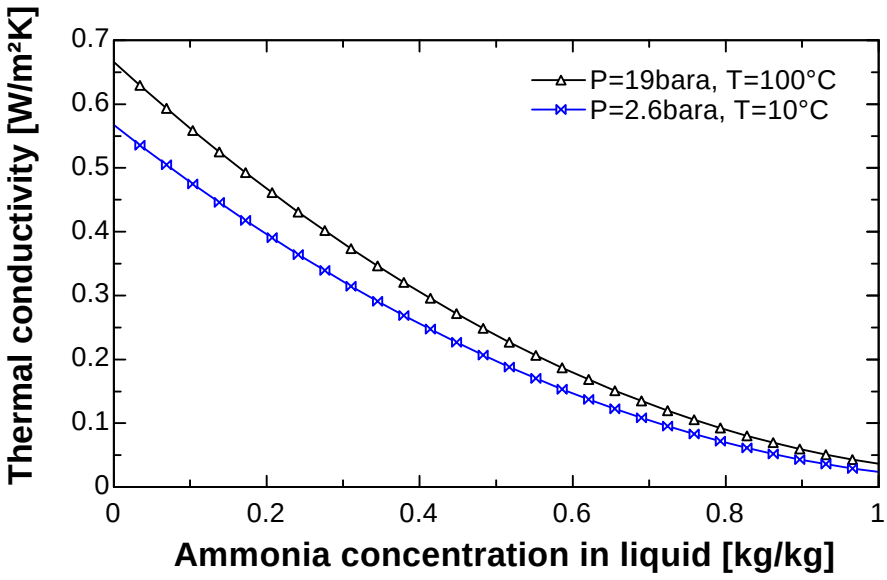

Figure A–4: Liquid thermal conductivity as a function of the ammonia concentration

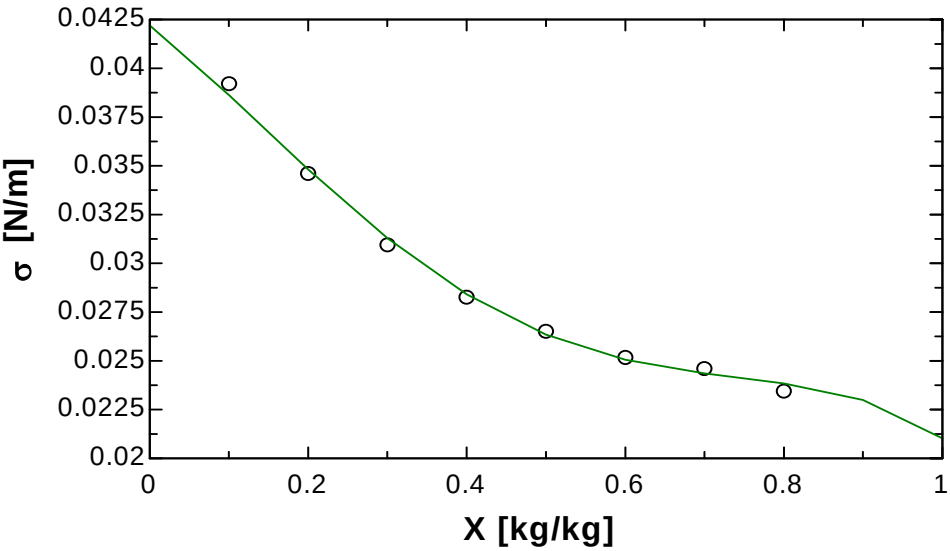

Figure A–5: Surface tension as a function of the ammonia concentration in the liquid

B The Silver/ Bell-Ghaly method

Silver [34] developed a method to derive an overall heat transfer coefficient for multicomponent condensation. This method was later rediscovered by Bell and Ghaly [35] , and has since then been generally used. The approximate procedure from Silver is explained in this section.

The total heat flux through the liquid film is given by:

$$\dot{q} = \frac{d\dot{Q}}{dA} \tag{B.1}$$

and the sensible heat flux in the vapour/gas phase by:

$$\dot{q}_g = \frac{d\dot{Q}_g}{dA} \tag{B.2}$$

where $\dot{Q}$ is the total heat transferred in area A of the heat transfer surface and $\dot{Q}_g$ is the portion of $\dot{Q}$ transferred for sensible cooling of the gas. Combining Equation B.1 and Equation B.2 we get:

$$\frac{\dot{q}_g}{\dot{q}} = \frac{d\dot{Q}_g}{d\dot{Q}} \tag{B.3}$$

Assuming that all heat released in cooling the condensate layer has to cross that layer, one can write:

$$\dot{q} = \alpha_l \cdot (T_i - T_w) \tag{B.4}$$

where α_l is the heat transfer coefficient of the condensate layer. For the sensible cooling one can write:

$$\dot{q}_g = \alpha_g \cdot (T_g - T_i) \tag{B.5}$$

where α_g is the gas phase heat transfer coefficient. By elimination of T_i from Equation B.4 and Equation B.5 one get:

$$\dot{q} = \frac{1}{\frac{1}{\alpha_l} + \frac{\dot{q}_g / \dot{q}}{\alpha_g}} \cdot (T_g - T_w) \tag{B.6}$$

Thus, the effective heat transfer coefficient is:

$$\alpha_{eff} = \frac{1}{\frac{1}{\alpha_l} + \frac{\dot{q}_g / \dot{q}}{\alpha_g}} \tag{B.7}$$

The ratio $\dot{q}_g / \dot{q}$ is usually written as Z. The Z factor is also given by:

$$Z = Qu_g \cdot c_{p,g} \cdot \frac{dT}{dh} \tag{B.8}$$

where Qu_g is the gas mass fraction, $c_{p,g}$ is the gas specific heat capacity, and $\frac{dT}{dh}$ is the gradient of the equilibrium condensation curve of the mixture.

Three assumptions that are usually made in order to simplify the evaluation of the terms in Equation B.8:

1) Z is evaluated on the basis of an equilibrium condensation curve.
2) α_g is calculated for the gas phase flowing alone in the system and therefore is not corrected for two-phase flow effects.
3) α_g is not corrected for mass transfer effects.

If the equilibrium curve is actually followed, the Silver method will be as accurate as any of the more advanced methods.

The method by Silver is originally developed for condensation, but by changing the direction of the heat flux this method can be used for evaporation. The heat flux for sensible heating of the vapour is given by:

$$\dot{q}_g = \alpha_g \cdot (T_i - T_g) \tag{B.9}$$

and the total heat flux crossing the film, again assuming that the sensible heat for the liquid crosses all the liquid, is given by:

$$\dot{q} = \alpha_c \cdot (T_w - T_i) + \alpha_{nb} \cdot (T_w - T_g) \tag{B.10}$$

where α_c is the forced convection heat transfer coefficient and α_{nb} is the nucleate boiling heat transfer coefficient. T_i, T_w and T_g is the interface temperature, the wall temperature and the bulk vapour temperature respectively.

By combination of Equation B.3, B.9 and B.10 the effective heat transfer coefficient is given by:

$$\alpha_{eff} = \frac{1 + \alpha_{nb}/\alpha_c}{\frac{1}{\alpha_c} + \frac{\dot{q}_g/\dot{q}}{\alpha_g}} \tag{B.11}$$

The nucleate boiling term α_{nb} must be corrected for mixture effects.

Sardesai et al.[39] studied the application of the Silver method on flow boiling. Equation B.11 is based an assumption that the bubble point temperature can be set equal to the vapour bulk temperature. This will lead to an overestimation of the total heat transfer. Assuming that the bubble point temperature is equal to the interface temperature will lead to more conservative results. The effective heat transfer coefficient can then be estimated with Equation B.12.

$$\alpha_{eff} = \frac{1}{\frac{1}{\alpha_c + \alpha_{nb}} + \frac{\dot{q}_g/\dot{q}}{\alpha_g}} \tag{B.12}$$

C Heat Transfer Correlations

The Boyko-Kruzhilin correlation

Boyko and Kruzhilin [37] developed a method for calculation of the heat transfer coefficient in two-phase flow based on an annular flow approach. The core is assumed to be a mixture of liquid and vapour. The shear stress at the wall is assumed to be equal to the shear stress at the interface, Equation C.1 and C.2.

$$\tau_i = \frac{f}{8} \cdot (\rho \cdot u^2)_{mix} \tag{C.1}$$

$$\tau_i = \frac{f}{8} \cdot (\rho_l \cdot u_l^{\,2}) \tag{C.2}$$

where u_l is the velocity of a liquid phase exerting the same force at the interface as the real core flow.

According to the Reynolds analogy between heat exchange and frictional force the heat transfer coefficient for single-phase flow can be described as in Equation C.2.

$$\alpha_{sp} \sim \frac{\tau_i}{u} \tag{C.3}$$

or for the region of the liquid/vapour flow using Equation C.2.

$$\alpha_{tp} \sim (\rho_l \cdot \tau_i)^{0.5} \tag{C.4}$$

Equation C.1 inserted into Equation C.4 gives:

$$\alpha_{tp} \sim \left(\frac{\rho_l}{\rho_m}\right)^{0.5} \tag{C.5}$$

When the fluid is a pure liquid ρ_m equals ρ_l and α_{tp} equals α_{sp}. This gives the equation for the local two-phase heat transfer coefficient.

$$\alpha_{tp} = \alpha_{sp,\,l} \cdot \sqrt{\frac{\rho_l}{\rho_m}} \tag{C.6}$$

The ratio between the liquid density and the vapour-liquid density can be expressed as follows:

$$\frac{\rho_l}{\rho_m} = 1 + \frac{\rho_l - \rho_g}{\rho_g} \cdot Qu_g \tag{C.7}$$

This method was compared to steam-water measurements during partial condensation in copper and steel tubes with a diameter of 8.0 mm at a pressure interval of 7 - 220 bar.

The Steiner and Taborek correlation

Steiner and Taborek [43] made a thorough investigation concerning flow boiling heat transfer in vertical tubes and tested their model on the University of Karlsruhe data bank containing over 13000 data points in vertical flow boiling. An asymptotic model was proposed.

$$\alpha_{tp}^{n} = (\alpha_{nb,0} \cdot F_{nbf})^{n} + (\alpha_{fc} \cdot F_{tp})^{n} \tag{C.8}$$

where:

$\alpha_{nb,0}$ is the local nucleate pool boiling heat transfer coefficient based on normalized conditions.

F_{nbf} is a correction factor to $\alpha_{nb,0}$ which compensates for the difference between pool and flow boiling.

α_{fc} is the local convective heat transfer coefficient, based on the total mass flow assumed to be all liquid. Steiner and Taborek recommends the Gnielinski correlation [44] .

F_{tp} is a two-phase enhancement factor which is a function of the vapour quality and the ratio of liquid/vapour densities. Steiner and Taborek gives two different equations for F_{tp} depending on outlet conditions.

n is an exponent to get an asymptotic behaviour in the transition area. Regression analysis of the data bank showed that n equal to 3 is acceptable.

The onset of nucleate boiling is calculated by the equation:

$$\dot{q}_{onb} = \frac{2 \cdot \sigma \cdot T_{sat} \cdot \alpha_{fc}}{r_{cr} \cdot \rho_{g} \cdot \Delta h_{fg}} \tag{C.9}$$

where r_{cr} is the critical bubble radius. $r_{cr} = 0.3 \cdot 10^{-6} m$ is recommended.

If the actual heat flux is lower than the onset of nucleate boiling, the nucleate boiling contribution is set to zero.

D Frictional pressure drop correlations

The Lockhart-Martinelli model

The model is based upon the following relations:

$$\left(\frac{dp}{dl}\right)_{tp} = \phi_l^2 \cdot \left(\frac{dp}{dl}\right)_l \tag{D.1}$$

$$\left(\frac{dp}{dl}\right)_{tp} = \phi_g^2 \cdot \left(\frac{dp}{dl}\right)_g \tag{D.2}$$

The parameter ϕ is a function of the Lockhart-Martinelli parameter X.

$$X^2 = \frac{\left(\frac{dp}{dl}\right)_{ls}}{\left(\frac{dp}{dl}\right)_{gs}} \tag{D.3}$$

In the original paper the relation between X and ϕ is presented as curves and tables based on low-pressure measurements of air/water and air/oil.

Chisholm has made a fit of the Lockhart-Martinelli data:

$$\phi_l^2 = 1 + \frac{C}{X} + \frac{1}{X^2} \tag{D.4}$$

The constant C is determined from the criteria tabulated in Table D–10

Table D–10: The Chisholm constant C.

Flow regimes of the phases	C
gas laminar - liquid laminart	5
gas laminar- liquid turbulent	10
gas turbulent- liquid laminar	12
gas turbulent - liquid turbulent	20

E Prediction of the mixture ammonia concentration

The ammonia concentration in the circulating working fluid mixture is used to determine the thermodynamic state in the different parts of the heat pump. Two different methods for the determination of the ammonia concentration can be used in the data analysis:

1) The density, pressure and temperature of the solution are used as inputs to the thermodynamic property routine AWMix [30] to estimate the ammonia concentration in the strong and weak ammonia/water solutions. The density in the solutions is measured with the coriolis meters. The pressure and temperature are taken from the nearest pressure transmitter and the nearest thermoelement.
2) Equilibrium can be assumed at the desorber 2 outlet. The ammonia concentration in the vapour and liquid can the be estimated with the AWMix routine. The ammonia concentration in the circulating solution can then be predicted from a component balance in the liquid/vapour separator. The mass flows of the solution strong in ammonia and the solution weak in ammonia are taken from the mass flow measurements with the coriolis meters.

In order to verify which of the two methods that give the most accurate prediction of the ammonia concentration a series of samples of the strong and weak solution were taken. Samples were taken both during standstill and during operation of the heat pump. The ammonia concentration were determined by titration with a 0.1M HCl acid using a Mettler Toledo DL50 titrator with an accuracy of $\pm 0.6\,\%$. The density were found using a 100 mL graduated flask with an accuracy of $\pm 0.01 mL$ and a precision weighting device with an accuracy of $\pm 0.01 g$. The diluted samples used in the titrator were taken using a pipette with an accuracy of $\pm 0.6\,\%$. The volume of the diluted sample were 0.1mL.

The relative uncertainty in the measurements of the ammonia concentration by titration was $\pm 0.85 - 0.92\,\%$, and the relative uncertainty in the density measurements was $\pm 0.08 - 0.4\ \%$.

Figure E–1 shows the results from the comparison of density measurements from the coriolis meters and those from using the graduated flask. The density measurements using the graduated flask are used as reference. The comparison shows that the coriolis meters predict the density within $\pm 5\,\%$.

The temperature transmitter upstream the coriolis meters and the nearest pressure transmitter are used when predicting the ammonia concentration with the coriolis meter density measurements. The nearest pressure transmitter is located at the absorber 1 inlet and at the absorber 2 outlet for the coriolis meter for the weak and strong solution respectively.

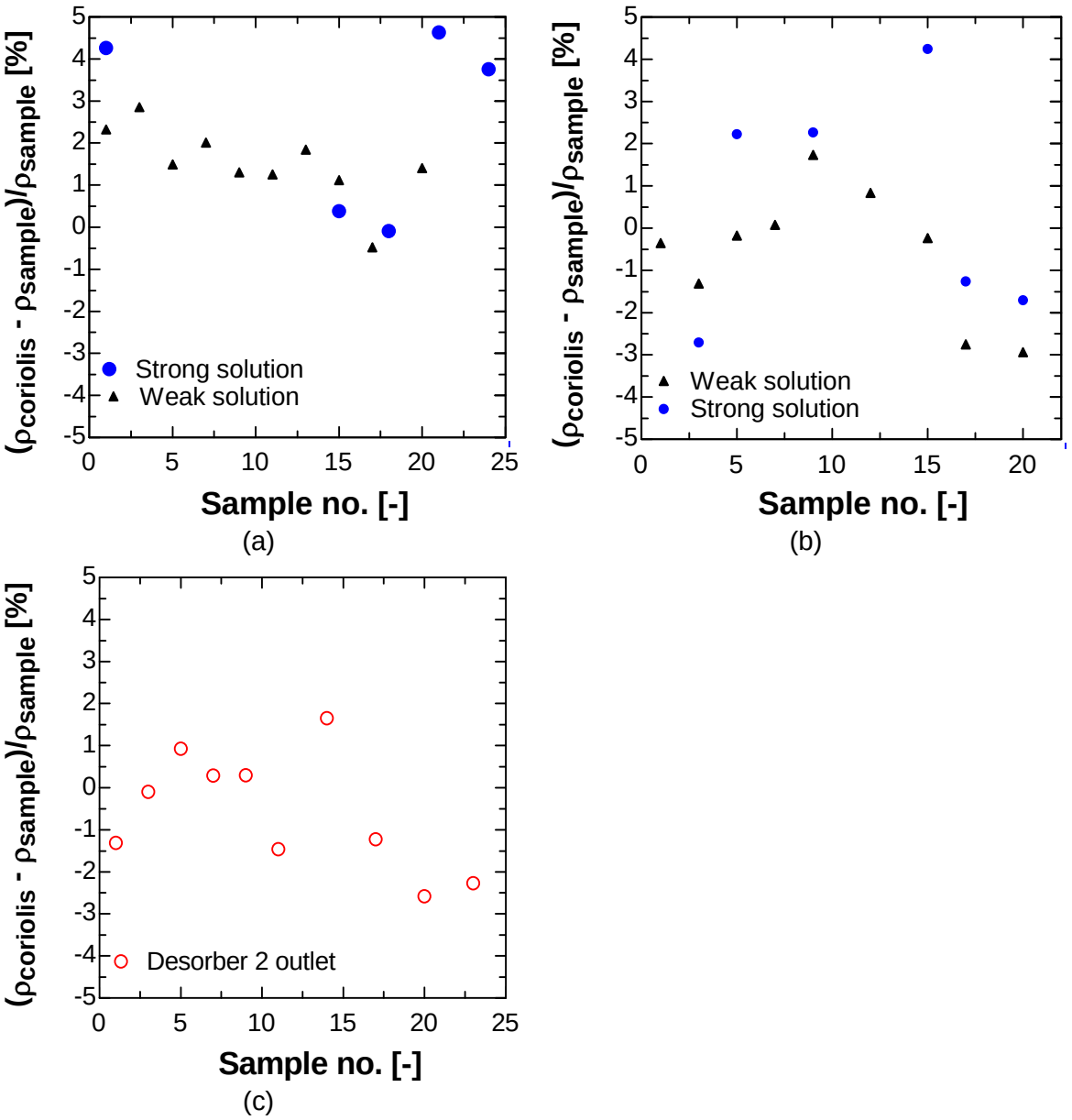

Figure E–1: Comparison of density measurements (a) At standstill (b) In operation (c) At desorber 2 outlet

The ammonia concentration determined from titration of the samples are compared with the predicted ammonia concentrations in Figure E–2. z_{calc} is the predicted ammonia concentrations using density determined from the coriolis meters, and when assuming equilibrium at the desorber 2 outlet. The deviation from the titration sample is largest for the samples taken from the strong solution during operation. This is probably due to the strong flashing when taking the samples. The samples were taken by dissolving the ammonia/water mixture in a known amount of distilled water. The sample bottles used were ordinary plastic bottles. A better procedure for taking the samples are required to avoid losing ammonia vapour from the sample.

It appears from the comparison of the different methods that the ammonia concentration is best predicted from the equilibrium considerations at the desorber 2 outlet. This will be used during the data reduction.

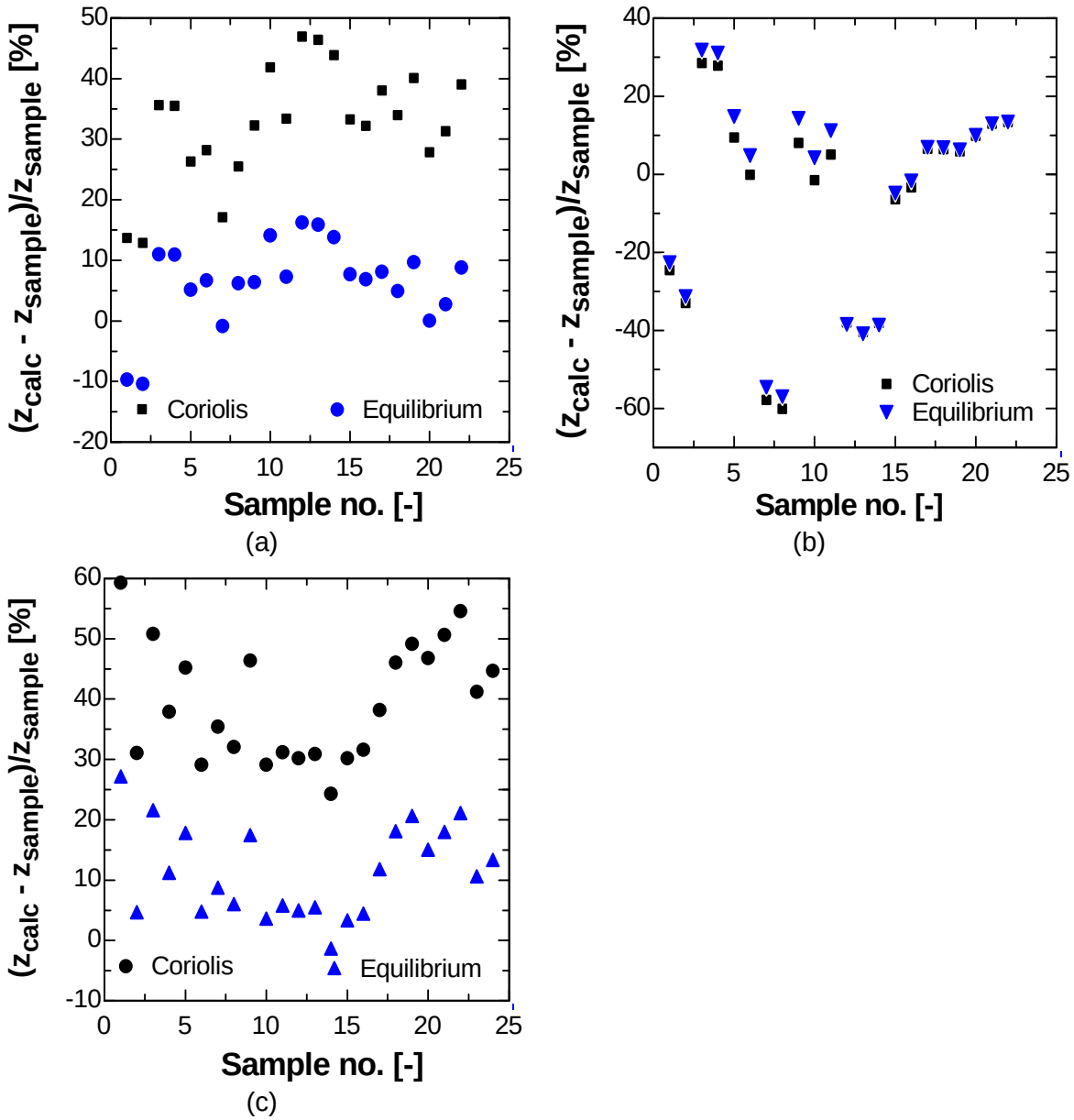

Figure E–2: Ammonia concentration measurements. (a) Weak solution (b) Strong solution (c) Desorber 2 outlet

F Estimation of Uncertainties

A result of a given measurement is only an estimate of the specific value of the quantity subject to the measurement. The result is therefore complete only when supplemented with a quantitative uncertainty. The uncertainties of the calculated value is predicted using the uncertainty calculation capability of the Engineering Equation Solver program [29] . The method for determining this uncertainty propagation is described in NIST Technical Note 1297 [54] . Assuming the individual measurements are uncorrelated and random, the uncertainty in the calculated quantity can be determined as

$$U_Y = \sqrt{\sum_i \left(\frac{\partial Y}{\partial X_i}\right)^2 \cdot U_{X_i}{}^2} \tag{F.1}$$

where U represents the uncertainty of the variable.

The relative uncertainty of a quantity is defined as the ratio of its absolute uncertainty to its value:

$$\text{Relative Uncertainty} = \frac{U_Y}{Y} \cdot 100 \tag{F.2}$$

Heat sink and heat source heat loads

The heat load of the heat sink and heat source were determined by the following energy balance:

$$\dot{Q} = \dot{m}_w \cdot c_{p,\,w} \cdot (T_{w,\,out} - T_{w,\,in}) \tag{F.3}$$

and the uncertainty becomes:

$$\Delta\dot{Q} = \sqrt{(\Delta\dot{m}_w \cdot c_{p,\,w} \cdot (T_{w,\,out} - T_{w,\,in}))^2 + (\Delta c_{p,\,w} \cdot \dot{m}_w \cdot (T_{w,\,out} - T_{w,\,in}))^2 + 2 \cdot (\dot{m}_w \cdot c_{p,\,w} \cdot \Delta T)^2} \tag{F.4}$$

where $\Delta\dot{m}_w$ is the uncertainty of the mass flow measurement, and ΔT is the uncertainty of the temperature measurements.

Coefficient of performance

The heating coefficient of performance was defined as a ratio of the heating capacity to the power input, i.e. the electrical engine motor power. The solution pump and booster pump power was neglected.

$$COP_{heating} = \frac{\dot{Q}_{abs1} + \dot{Q}_{abs2} + \dot{Q}_{desuperheater}}{\dot{W}_{motor}} \tag{F.5}$$

The uncertainty becomes:

$$\Delta COP_{heating} \tag{F.6}$$

$$= \sqrt{\left(\frac{\Delta\dot{Q}_{abs1}}{\dot{W}_c}\right)^2 + \left(\frac{\Delta\dot{Q}_{abs2}}{\dot{W}_c}\right)^2 + \left(\frac{\Delta\dot{Q}_{desuperheater}}{\dot{W}_c}\right)^2 + \left(-\frac{\dot{Q}_{abs1} + \dot{Q}_{abs2} + \dot{Q}_{desuperheater}}{\dot{W}_c^2} \cdot \Delta\dot{W}_c\right)^2}$$

Overall heat transfer coefficients

The overall heat transfer coefficients for the heat exchangers were calculated as:

$$U = \frac{\dot{Q}}{A \cdot LMTD} \tag{F.7}$$

The uncertainty of the overall heat transfer coefficient becomes:

$$\Delta U = \sqrt{\left(\frac{\Delta\dot{Q}}{A \cdot LMTD}\right)^2 + \left(\frac{\dot{Q}}{A \cdot \Delta LMTD}\right)^2} \tag{F.8}$$

Isentropic efficiency

The isentropic efficiency of the compressor was defined as as a ratio of the compressors isentropic work to shaft power consumption as given by:

$$\eta_{isen} = \frac{\dot{m}_1 \cdot (h_{2isen} - h_1) + \dot{m}_3 \cdot (h_{4isen} - h_3)}{W_{shaft}} \tag{F.9}$$

where the nominator is the shaft work. The uncertainty then becomes:

$$\begin{aligned}\Delta\eta_{isen}{}^2 = &\left(\frac{(h_{2isen} - h_1)}{W_{shaft}} \cdot \Delta\dot{m}_1\right)^2 + \left(\frac{\dot{m}_1}{W_{shaft}} \cdot \Delta h_{2isen}\right)^2 + \left(\frac{\dot{m}_1}{W_{shaft}} \cdot \Delta h_1\right)^2 \\ &+ \left(\frac{(h_{4isen} - h_3)}{W_{shaft}} \cdot \Delta\dot{m}_3\right)^2 + \left(\frac{\dot{m}_3}{W_{shaft}} \cdot \Delta h_{4isen}\right)^2 + \left(\frac{\dot{m}_3}{W_{shaft}} \cdot \Delta h_3\right)^2 \\ &+ \left(\frac{\dot{m}_1 \cdot (h_{2isen} - h_1) + \dot{m}_3 \cdot (h_{4isen} - h_3)}{W_{shaft}^2} \cdot \Delta W_{shaft}\right)^2\end{aligned} \tag{F.10}$$

Volumetric efficiency

The volumetric efficiency was defined as a ratio of the theoretical mass flow rates of refrigerant to actual mass flow rates of working fluid:

$$\eta_{vol} = \frac{\dot{m}_1 \cdot v_1}{V_{disp}} \tag{F.11}$$

where V_{disp} is the compressor displacement volume and v_1 is the specific volume of the ammonia-water vapour at the compressor suction inlet. Its uncertainty is:

$$\Delta\eta_{vol} = \sqrt{\left(\frac{v_1}{V_{disp}} \cdot \Delta\dot{m}_1\right)^2 + \left(\frac{\dot{m}_1}{V_{disp}} \cdot \Delta v_1\right)^2 + \left(\frac{\dot{m}_1 \cdot v_1}{V_{disp}^2} \cdot \Delta V_{disp}\right)^2} \tag{F.12}$$

Thermodynamic properties

The uncertainties of the thermodynamic properties involved in the calculation were a function of temperature (T), pressure (P) and ammonia concentration (Z), and were calculated by the following relationship:

$$\Delta f = \sqrt{\left(\frac{\partial f}{\partial T} \cdot \Delta T\right)^2 + \left(\frac{\partial f}{\partial P} \cdot \Delta P\right)^2 + \left(\frac{\partial f}{\partial Z} \cdot \Delta Z\right)^2} \tag{F.13}$$

G Summary of experimental results

The indexes in table G.1 to G.10 refer to the numbered measurement point in Figure G–1.

The test runs used in chapter 5 are T-01, T-02, T-03, T-05, T-06, T-07, T-08, T-09, T-11, T-12,T-13, T-14, T-15, T-16, T-23 and T-24.

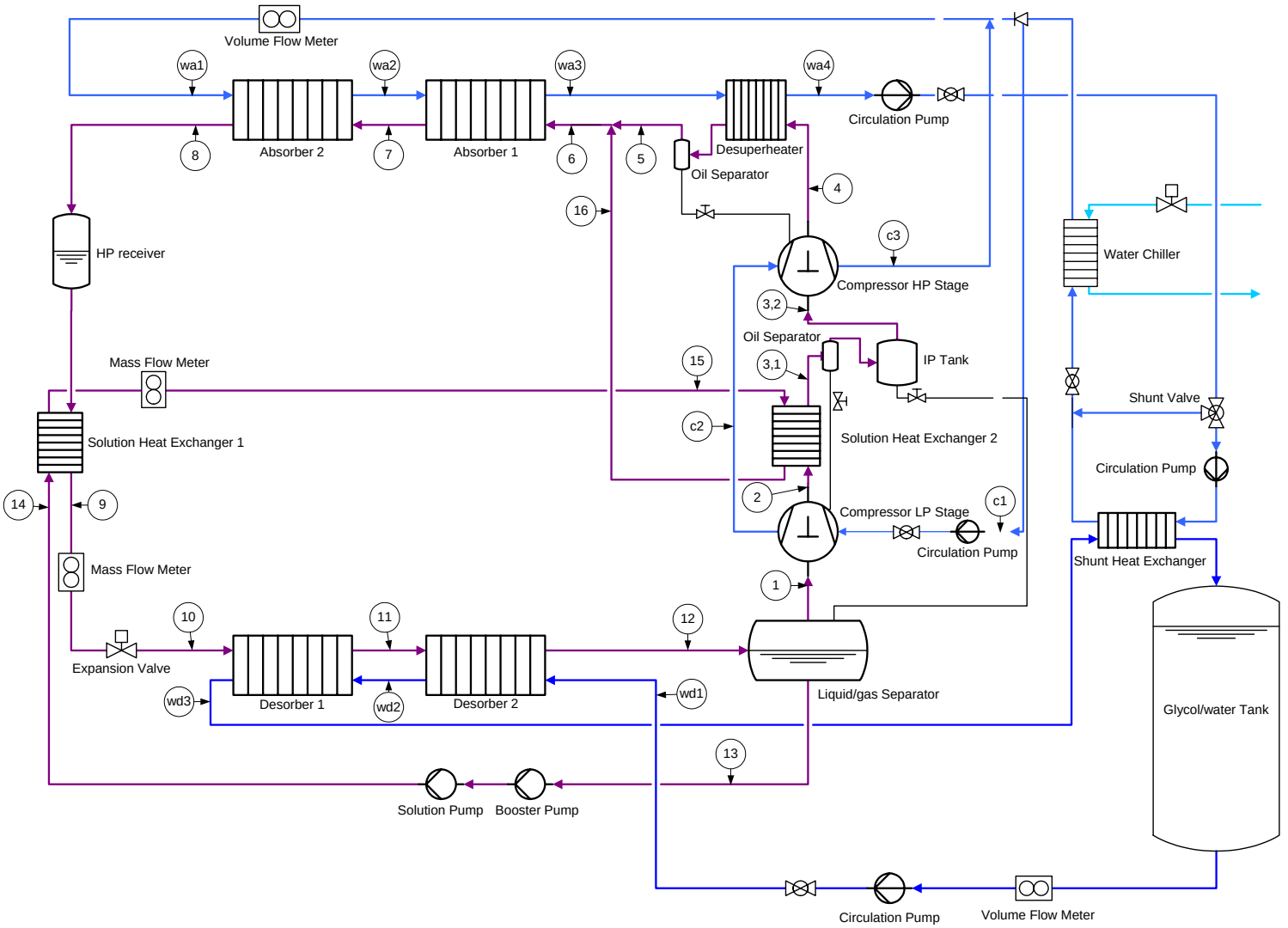

Figure G–1: Measurement points

Table G–1: Temperatures in °C

Test #	T_1	T_2	$T_{3,1}$	$T_{3,2}$	T_4	T_5	T_7	T_8	T_9	T_{10}	T_{11}	T_{12}	T_{13}	T_{14}	T_{15}	T_{16}	T_{wa1}	T_{wa2}	T_{wa3}	T_{wa4}
T-01	49	100.8	66	63.8	142.6	88.6	70.4	58.4	51.5	2.6	28.6	50.2	50.2	46.8	56.4	83	50.6	61.3	80	84.1
T-02	49.5	102.8	69	67	146.2	91	71.4	59.4	52.4	1.9	29	50.2	50.2	45.4	57.4	85.4	51.4	62.7	82.2	86.6
T-03	47.5	100.6	63.2	62.6	139.6	85.4	70.5	57.5	50.4	6.4	29.1	47.8	47.8	44.9	54.5	79.2	50	61	78.6	82.2
T-04	44.7	100	60.6	61.2	134.7	86.6	71	57.3	50.5	8.1	30.1	45.2	45.2	43.8	54.3	76.7	49.6	62.4	80.9	83.9
T-05	46	97.6	60.7	58.7	134.5	83.1	68.8	55.7	50.3	5.5	30.3	46.9	46.9	44	52.7	75.5	49.1	59.1	75.4	78.6
T-06	46.8	97.4	61.9	59.3	134.9	81.3	65.7	54.8	50.3	2.7	30.4	47.6	47.6	45.2	52.4	77.2	47.9	56.5	73.6	76.7
T-07	47.5	98	63.9	61.4	138.5	82.5	66.5	56.3	51.6	1.5	30.7	48.1	48.1	45.9	54.3	79.5	50.2	57.9	74.4	78.3
T-08	48.3	99.9	67.4	64.6	144	85.1	66.7	57.6	52.5	-1.3	31	49	49	46.2	55.6	81.2	51.1	58.6	75.4	79.9
T-09	42.8	102.2	65.9	63	142.4	102.1	76.4	57.7	51.5	4.5	24.7	44	40.9	38.4	51.9	77.8	50.2	67.6	88.1	91
T-10	42.9	102.3	64.3	62.2	141.9	102.4	76.4	56.8	51	4.8	24.7	44	41.3	38.4	51.1	77.9	49.9	67.6	88	91.5
T-11	43.5	103.1	69.6	66.1	144.5	101.5	75.1	55.3	50	3.9	26.2	44.7	41.9	38.3	50.2	76.1	50	66.3	86.5	88.9
T-12	43.2	101.2	61	59.5	138.4	95.4	74.6	54.9	49.7	5.7	26	44.3	41.8	39.4	49.7	77.1	49.8	65.7	85.8	90
T-13	43.4	102.4	69.5	65.4	140.9	97.7	75.7	56	50.3	6	25.7	44.8	41.4	38.3	50.3	72.6	50.2	67.2	86.8	93
T-14	43.2	103.4	71.6	67.4	142.7	99.6	76.5	57.3	51.2	6.1	25.2	44.4	41.8	38.6	51.4	74	50.6	68.3	87.6	94.1
T-15	42.9	103.4	71.9	67.9	142.5	99.5	76.2	57.1	51	6	24.7	44	41.5	38.2	51.2	73.9	50.1	67.9	87.3	93.8
T-16	44.8	100.5	69.7	64.9	144.3	98.3	76.4	58.6	53	6.2	27.8	45.9	43.1	41.7	53.1	72.4	51.1	67.4	88.2	89.5
T-17	43.8	102.3	69	66.9	143.9	98.2	76.2	57.7	52.4	6	25.9	44.7	42.8	41.2	52.4	72.8	50.6	67.5	88	89
T-18	43.4	102.9	68.5	65.1	145	99.9	76.3	57.6	52	5.2	25.7	44.6	42	40.3	52.1	74.1	50.1	67.6	88.3	89.2
T-19	42.9	103.6	68.9	65.2	146.6	100.7	76.1	57.2	51.5	4.8	24.9	43.8	41.4	39.5	51.5	74.2	50.2	67.3	88	90.6

Table G–1: Temperatures in °C

Test #	T_1	T_2	$T_{3,1}$	$T_{3,2}$	T_4	T_5	T_7	T_8	T_9	T_{10}	T_{11}	T_{12}	T_{13}	T_{14}	T_{15}	T_{16}	T_{wa1}	T_{wa2}	T_{wa3}	T_{wa4}
T-20	42.3	104.1	69.4	65.4	147.9	101.2	76.1	57.1	51.1	4.4	23.8	43.2	40.9	38.8	51.3	74.3	49.9	67.5	87.8	91.4
T-21	42.1	105.1	71	66.7	150.5	102.7	76.7	57.5	51.3	4	23.3	43.2	40.5	38.2	51.4	74.9	50.2	68.2	88.6	90
T-22	41.8	106.7	73.3	68.4	154.3	105.1	78	58.3	52	3.4	22.1	43.1	40.3	37.8	52.1	76.2	49.9	69.5	90.2	91.1
T-23	43.1	103.7	75.8	71.1	143	109	74.8	60.7	54.4	6.2	25.2	44.1	41.7	41.1	54.6	71.7	49.6	66.5	86.8	87.5
T-24	42.7	103.8	82.4	76.5	146.6	104.3	75.4	61.8	54.8	6.1	25.5	43.9	40.8	40.1	54.9	68	51	67.3	86.2	87.8
T-25	42	104.9	71	66.8	148.8	99.8	77.4	62.6	55.3	4.6	23.4	43.1	40.6	39.5	55.5	78.5	50.1	69.2	89.3	91.2
T-26	41.4	105.2	71	67.2	149.8	99.6	76.9	61.9	54.7	4	22.4	42.4	40	38.7	54.7	78.2	49.4	68.7	88.7	90.5
T-27	38.8	105.8	71.7	67.5	152.7	100	76.9	62	54.3	2.8	17.2	39.2	38.7	37.2	54.7	78.4	50.3	68.7	88.2	89.7

Table G–2: Temperatures in °C

Test #	T_{wd1}	T_{wd2}	T_{wd3}	T_{c1}	T_{c2}	T_{c3}
T-01	52.7	46.6	24.4	47.9	57	64.6
T-02	52.4	46.6	22.9	48.6	57.8	65.7
T-03	51.3	43.3	24.7	47.7	56.3	63.5
T-04	50.3	39.3	22.4	47.2	56	62.8
T-05	49.9	42.7	24.5	46.7	54.7	61.3
T-06	49.8	44.2	25.2	45.5	53.6	60.6
T-07	50.1	45	25.5	47.8	55.8	62.8
T-08	50.5	46.5	25.5	48.5	56.8	64.4

Table G–2: Temperatures in °C

Test #	T_{wd1}	T_{wd2}	T_{wd3}	T_{c1}	T_{c2}	T_{c3}
T-09	49.9	34	16.3	47.2	56.1	63.6
T-10	50.1	33.9	16.4	46.8	55.7	63.1
T-11	49.7	35.9	16.4	47.1	55.9	63.6
T-12	50.1	35.1	17.4	47.1	55.1	62.3
T-13	50.9	34.6	17.3	47.4	55.8	63.3
T-14	50.8	34	17.2	47.9	56.2	63.8
T-15	50.4	33.5	16.8	47.3	55.8	63.5
T-16	51.6	37.1	18.7	48	56.2	63.9
T-17	51.3	35.3	17.7	47.7	56	63.7
T-18	50.9	35.2	17.3	47.2	55.7	63.5
T-19	50.5	34.2	16.6	47.2	55.9	63.8

Table G–3: Pressures in bars

Test #	P_1	P_2	P_4	P_5	P_6	P_7	P_8	P_{10}	P_{11}	P_{12}	P_{wa1}
T-01	1.86	4.92	17.48	17.18	16.97	16.97	16.88	2.09	2.13	1.97	1.51
T-02	2	5.34	19.02	18.77	18.47	18.47	18.38	2.25	2.28	2.12	1.56
T-03	1.72	4.51	15.12	14.85	14.59	14.52	14.52	1.93	1.97	1.83	1.49
T-04	1.87	4.85	15.16	14.8	14.57	14.5	14.5	2.11	2.13	1.98	1.51
T-05	1.57	4.1	14.02	13.78	13.58	13.47	13.47	1.75	1.8	1.67	2.12

Table G–3: Pressures in bars

Test #	P_1	P_2	P_4	P_5	P_6	P_7	P_8	P_{10}	P_{11}	P_{12}	P_{wa1}
T-06	1.51	3.96	13.99	13.79	13.56	13.46	13.46	1.69	1.73	1.6	2.05
T-07	1.52	4.08	15.19	14.9	14.76	14.65	14.65	1.7	1.76	1.63	2.11
T-08	1.6	4.35	16.95	16.75	16.53	16.41	16.41	1.79	1.85	1.71	2.11
T-09	2.29	6.08	20.33	20	19.87	19.79	19.68	2.53	2.55	2.39	2.93
T-10	2.26	6	20.03	19.77	19.57	19.49	19.38	2.5	2.53	2.37	2.9
T-11	2.24	6	20.15	19.79	19.67	19.59	19.5	2.48	2.51	2.35	2.77
T-12	2.17	5.72	18.94	18.57	18.45	18.37	18.32	2.42	2.44	2.28	2.8
T-13	2.26	6.04	19.44	19.04	18.91	18.84	18.77	2.52	2.54	2.38	2.8
T-14	2.34	6.23	19.93	19.52	19.38	19.31	19.24	2.59	2.61	2.45	2.82
T-15	2.36	6.29	19.84	19.42	19.28	19.22	19.15	2.61	2.63	2.47	2.79
T-16	2.22	5.9	19.6	19.33	19.11	19.03	18.95	2.47	2.48	2.33	2.67
T-17	2.21	5.9	19.57	19.2	19.07	18.99	18.89	2.47	2.48	2.32	2.67
T-18	2.15	5.77	19.61	19.24	19.11	19.03	18.93	2.42	2.43	2.27	2.69
T-19	2.12	5.7	19.61	19.24	19.09	19.01	18.91	2.39	2.4	2.23	2.67
T-20	2.11	5.68	19.67	19.26	19.12	19.04	18.94	2.39	2.39	2.21	2.66
T-21	2.12	5.71	20.06	19.63	19.48	19.4	19.33	2.4	2.4	2.22	2.67
T-22	2.07	5.71	20.66	20.45	20.04	19.96	19.88	2.4	2.4	2.2	2.73
T-23	2.29	6.08	18.78	18.42	18.3	18.22	18.07	2.53	2.55	2.39	4.01
T-24	2.24	6.07	19.07	18.72	18.6	18.51	18.39	2.48	2.5	2.35	3.64
T-25	2.15	5.83	19.95	19.55	19.41	19.33	19.21	2.43	2.44	2.26	3.33

Table G–3: Pressures in bars

Test #	P_1	P_2	P_4	P_5	P_6	P_7	P_8	P_{10}	P_{11}	P_{12}	P_{wa1}
T-26	2.11	5.76	19.8	19.37	19.23	19.15	19.03	2.4	2.41	2.22	3.31
T-27	2.05	5.6	20.14	19.71	19.56	19.48	19.4	2.32	2.32	2.15	3.25

Table G–4: Mass flow in kg/s and densities in kg/m^3

Test #	m_{ss}	m_{ws}	m_{sink}	m_{source}	mc_{ooling}	ρ_{13}	ρ_9
T-01	0.0415	0.0186	0.255	0.257	0.052	858.7	727.2
T-02	0.0418	0.0164	0.255	0.257	0.052	859.5	713.7
T-03	0.0445	0.0221	0.255	0.258	0.052	864.8	752.2
T-04	0.0519	0.0252	0.255	0.258	0.052	857.9	752.4
T-05	0.0416	0.0224	0.255	0.258	0.052	867.5	760.4
T-06	0.0373	0.0191	0.255	0.258	0.052	869.3	754.1
T-07	0.0361	0.0168	0.255	0.258	0.052	870	746
T-08	0.034	0.014	0.255	0.258	0.052	868.6	727.4
T-09	0.053	0.0243	0.255	0.258	0.052	837.5	719.4
T-10	0.0533	0.0249	0.252	0.245	0.052	838.1	723
T-11	0.0508	0.0228	0.255	0.248	0.052	837.8	719.4
T-12	0.0542	0.0268	0.255	0.258	0.052	841.5	733.8
T-13	0.0553	0.0267	0.255	0.258	0.052	839.9	729
T-14	0.0561	0.0266	0.255	0.258	0.052	837.3	724.4
T-15	0.0562	0.0266	0.255	0.258	0.052	836.3	723
T-16	0.054	0.0267	0.255	0.258	0.052	842.7	732
T-17	0.056	0.0267	0.255	0.258	0.052	842.6	731.5
T-18	0.0553	0.0267	0.255	0.258	0.052	842.2	729.5
T-19	0.056	0.0267	0.255	0.258	0.052	842.9	729.2
T-20	0.0568	0.0267	0.255	0.258	0.052	842.6	727.6
T-21	0.0575	0.0266	0.255	0.258	0.052	842.1	724.7
T-22	0.0586	0.0266	0.255	0.258	0.052	841.8	719.3
T-23	0.0556	0.0265	0.255	0.258	0.052	839	725
T-24	0.0547	0.0266	0.255	0.258	0.052	840.5	724.9
T-25	0.0574	0.0264	0.255	0.258	0.052	841.5	717.4

Table G–4: Mass flow in kg/s and densities in kg/m^3

Test #	m_{ss}	m_{ws}	m_{sink}	m_{source}	mc_{ooling}	ρ_{13}	ρ_{9}
T-26	0.0578	0.0264	0.255	0.258	0.052	841.4	716.6
T-27	0.0578	0.0261	0.255	0.258	0.052	839.5	714.5

Table G–5: Rotational velocity of compressor and solution pump in RPM. Compressor motor work in kW.

Test #	$RPM_{compressor}$	RPM_{pump}	W_{motor}
T-01	1005	967	15.68
T-02	990	834	16.91
T-03	1005	1112	14.18
T-04	1005	1110	14.76
T-05	1005	967	13.18
T-06	1005	834	12.95
T-07	1005	695	13.53
T-08	1005	695	14.52
T-09	990	1253	18.75
T-10	990	1168	18.52
T-11	975	1392	18.57
T-12	990	1392	17.61
T-13	990	1392	18.31
T-14	975	1392	18.81

Table G–5: Rotational velocity of compressor and solution pump in RPM. Compressor motor work in kW.

Test #	$RPM_{compressor}$	RPM_{pump}	W_{motor}
T-15	975	1391	18.87
T-16	990	1391	18
T-17	1020	1391	18.57
T-18	1065	1391	18.92
T-19	1080	1391	19.33
T-20	1110	1391	19.84
T-21	1140	1391	20.65
T-22	1200	1391	21.95
T-23	990	1391	17.91
T-24	990	1391	18.1
T-25	1110	1391	20.24
T-26	1140	1391	20.58
T-27	1170	1391	20.91

Table G–6: Reduced parameters

Test #	Z_{ss}	X_{ws}	Y_v	Z_a	PR	PR_{LP}	PR_{HP}	CR	$COP_{Heating}$	Heat-Efficiency	Q_{sink}	Q_{source}	Qu_6	Qu_7	SCD
	[kg/kg]	[kg/kg]	[kg/kg]	[kg/kg]	-	-	-	-	-	-	[kW]	[kW]	[kg/kg]	[kg/kg]	
T-01	0.653	0.276	0.958	0.464	9.40	2.65	3.55	0.81	2.26	0.927	35.74	29.78	0.466	0.145	1.057
T-02	0.697	0.287	0.962	0.492	9.51	2.67	3.56	0.65	2.20	0.922	37.55	31.04	0.528	0.214	0.923

Table G–6: Reduced parameters

Test #	Z_{ss}	X_{ws}	Y_v	Z_a	PR	PR_{LP}	PR_{HP}	CR	$COP_{Heating}$	Heat-Efficiency	Q_{sink}	Q_{source}	Qu_6	Qu_7	SCD
T-03	0.621	0.277	0.961	0.449	8.79	2.62	3.35	0.99	2.39	0.957	34.36	28.01	0.425	0.169	1.211
T-04	0.646	0.302	0.970	0.474	8.11	2.59	3.13	0.94	2.45	0.968	36.61	29.39	0.452	0.231	1.084
T-05	0.587	0.269	0.958	0.428	8.93	2.61	3.42	1.17	2.36	0.926	31.48	26.77	0.377	0.111	1.406
T-06	0.598	0.260	0.953	0.4289	9.26	2.62	3.53	1.05	2.35	0.935	30.75	25.92	0.397	0.093	1.409
T-07	0.630	0.260	0.953	0.445	9.99	2.68	3.72	0.87	2.19	0.901	29.97	25.92	0.440	0.128	1.329
T-08	0.669	0.262	0.953	0.4653	10.59	2.72	3.90	0.70	2.10	0.897	30.71	26.34	0.490	0.145	1.196
T-09	0.684	0.336	0.979	0.5102	8.88	2.66	3.34	0.85	2.30	0.932	43.57	35.39	0.484	0.213	0.833
T-10	0.678	0.335	0.979	0.5064	8.86	2.65	3.34	0.88	2.34	0.973	43.91	33.77	0.476	0.208	0.848
T-11	0.687	0.330	0.978	0.5083	9.00	2.68	3.36	0.81	2.21	0.925	41.53	33.72	0.492	0.206	0.8317
T-12	0.656	0.327	0.977	0.4916	8.73	2.64	3.31	0.98	2.41	0.949	42.93	34.44	0.443	0.166	0.9146
T-13	0.666	0.331	0.978	0.4984	8.60	2.67	3.22	0.93	2.47	0.979	45.71	35.37	0.452	0.190	0.8803
T-14	0.675	0.338	0.979	0.5064	8.52	2.66	3.20	0.90	2.44	0.986	46.46	35.37	0.464	0.209	0.8443
T-15	0.678	0.341	0.980	0.5094	8.41	2.67	3.15	0.90	2.44	0.991	46.68	35.38	0.466	0.214	0.8364
T-16	0.652	0.322	0.975	0.4874	8.83	2.66	3.32	0.98	2.25	0.903	40.98	34.63	0.435	0.161	0.9262
T-17	0.668	0.328	0.977	0.4977	8.86	2.67	3.32	0.91	2.18	0.882	40.99	35.37	0.457	0.197	0.9016
T-18	0.662	0.325	0.977	0.4936	9.12	2.68	3.40	0.93	2.18	0.893	41.75	35.37	0.452	0.183	0.925
T-19	0.667	0.327	0.977	0.4968	9.25	2.69	3.44	0.91	2.21	0.910	43.14	35.69	0.460	0.193	0.9262
T-20	0.673	0.328	0.978	0.5005	9.32	2.69	3.46	0.89	2.21	0.918	44.32	36.22	0.469	0.206	0.9199
T-21	0.678	0.329	0.978	0.5034	9.46	2.69	3.51	0.86	2.04	0.863	42.49	36.95	0.477	0.216	0.9046
T-22	0.683	0.328	0.978	0.5056	9.98	2.76	3.62	0.83	1.98	0.855	44	38.42	0.487	0.229	0.9139

Table G–6: Reduced parameters

Test #	Z_{ss}	X_{ws}	Y_v	Z_a	PR	PR_{LP}	PR_{HP}	CR	$COP_{Heating}$	Heat-Efficiency	Q_{sink}	Q_{source}	Qu_6	Qu_7	SCD
T-23	0.672	0.336	0.979	0.5039	8.20	2.66	3.09	0.91	2.23	0.899	40.47	34.43	0.470	0.215	0.8719
T-24	0.665	0.334	0.979	0.4996	8.51	2.71	3.14	0.95	2.14	0.870	39.27	34.44	0.450	0.196	0.9283
T-25	0.681	0.332	0.979	0.5068	9.28	2.71	3.42	0.85	2.14	0.901	43.89	36.53	0.483	0.237	0.9156
T-26	0.684	0.333	0.979	0.5087	9.38	2.73	3.44	0.84	2.11	0.891	43.9	36.96	0.487	0.243	0.925
T-27	0.695	0.345	0.983	0.5201	9.82	2.73	3.60	0.82	1.99	0.796	42.06	40.75	0.496	0.258	0.9465

Table G–7: Calculated variables

Test #	Qu_{10}	Qu_{11}	Qu_{12}	$\frac{\Delta T_{solution}}{\Delta T_{sink}}$	$\frac{\Delta T_{solution}}{\Delta T_{source}}$	$\Delta T_{out,\,shx2}$	$\Delta P_{desorber}$	$\Delta P_{absorber}$	ΔP_{4-6}	U_{abs1}	U_{abs2}	U_{des1}	U_{des2}
										[kW/ m^2·K]	[kW/ m^2·K]	[kW/ m^2·K]	[kW/ m^2·K]
T-01	0.158	0.423	0.552	1.609	1.682	9.6	0.12	0.09	0.51	0.694	0.751	0.736	0.512
T-02	0.219	0.491	0.608	1.526	1.637	11.6	0.13	0.09	0.55	0.763	0.801	0.809	0.516
T-03	0.183	0.387	0.503	1.544	1.556	8.7	0.1	0.07	0.53	0.683	0.770	0.757	0.690
T-04	0.228	0.421	0.514	1.334	1.33	6.3	0.13	0.07	0.59	0.858	0.931	0.962	1.043
T-05	0.132	0.354	0.462	1.701	1.63	8	0.08	0.11	0.44	0.598	0.736	0.775	0.717
T-06	0.127	0.378	0.488	1.781	1.825	9.5	0.09	0.1	0.43	0.614	0.638	0.703	0.585
T-07	0.177	0.429	0.535	1.892	1.894	9.6	0.07	0.11	0.43	0.599	0.626	0.685	0.538
T-08	0.196	0.485	0.588	1.906	2.012	11.8	0.08	0.12	0.42	0.613	0.611	0.670	0.440
T-09	0.176	0.421	0.542	1.282	1.176	14	0.14	0.19	0.46	0.942	1.267	1.108	1.402

Table G–7: Calculated variables

Test #	Qu_{10}	Qu_{11}	Qu_{12}	$\frac{\Delta T_{solution}}{\Delta T_{sink}}$	$\frac{\Delta T_{solution}}{\Delta T_{source}}$	$\Delta T_{out,\,shx2}$	$\Delta P_{desorber}$	$\Delta P_{absorber}$	ΔP_{4-6}	U_{abs1}	U_{abs2}	U_{des1}	U_{des2}
T-10	0.173	0.411	0.533	1.295	1.163	13.2	0.13	0.19	0.46	0.928	1.327	1.057	1.346
T-11	0.181	0.439	0.551	1.398	1.225	19.4	0.13	0.17	0.48	0.883	1.399	1.117	1.233
T-12	0.154	0.387	0.506	1.385	1.18	11.3	0.14	0.13	0.49	0.897	1.380	1.125	1.349
T-13	0.163	0.394	0.517	1.322	1.155	19.2	0.14	0.14	0.53	0.931	1.425	1.131	1.449
T-14	0.174	0.403	0.526	1.279	1.14	20.2	0.14	0.14	0.55	0.949	1.412	1.115	1.468
T-15	0.174	0.402	0.527	1.26	1.131	20.7	0.14	0.13	0.56	0.959	1.382	1.124	1.477
T-16	0.145	0.390	0.506	1.278	1.207	16.6	0.14	0.16	0.49	0.956	1.173	1.118	1.299
T-17	0.178	0.404	0.523	1.266	1.152	16.6	0.15	0.18	0.5	0.980	1.271	1.101	1.331
T-18	0.159	0.397	0.517	1.265	1.173	16.4	0.15	0.18	0.5	0.972	1.282	1.095	1.327
T-19	0.170	0.402	0.523	1.283	1.15	17.4	0.16	0.18	0.52	0.965	1.288	1.102	1.354
T-20	0.176	0.405	0.530	1.277	1.128	18.1	0.18	0.18	0.55	0.956	1.323	1.089	1.455
T-21	0.178	0.411	0.537	1.267	1.117	19.6	0.18	0.15	0.58	0.971	1.352	1.095	1.460
T-22	0.179	0.411	0.546	1.219	1.088	21.2	0.2	0.16	0.62	0.996	1.374	1.106	1.443
T-23	0.182	0.402	0.523	1.161	1.159	21.2	0.14	0.23	0.48	0.991	1.039	1.046	1.325
T-24	0.172	0.395	0.514	1.184	1.156	27.5	0.13	0.21	0.47	0.926	1.028	1.136	1.389
T-25	0.193	0.415	0.540	1.104	1.11	15.5	0.17	0.2	0.54	1.004	1.109	1.096	1.460
T-26	0.195	0.415	0.543	1.105	1.094	16.3	0.18	0.2	0.57	0.997	1.121	1.094	1.464
T-27	0.215	0.402	0.548	1.113	0.9406	17	0.17	0.16	0.58	0.993	1.107	1.206	1.610

Table G–8: Calculated variables

Test #	$U_{desuperheater}$	U_{shx1}	U_{shx2}	$\Delta T_{in,\,shx1}$	$\frac{Q_{cooling}}{W_{shaft}}$	$\frac{W_{pumps}}{W_{motor}}$	$\Delta T_{16,\,subcooling}$	$\Delta T_{8,\,subcooling}$
	[kW/m^2·K]	[kW/m^2·K]	[kW/m^2·K]	[K]	[%]	[%]	[K]	[K]
T-01	1.684	7.900	0.288	2	28.6	1.0	48.4	5.1
T-02	1.772	6.435	0.240	2	27.2	0.8	47.7	3.4
T-03	1.623	6.642	0.271	3	29.9	1.2	44.7	3.2
T-04	1.557	6.669	0.341	3	28.4	1.3	41.4	0.7
T-05	1.407	4.351	0.255	3	29.7	1.3	47.0	6.1
T-06	1.327	4.043	0.234	2.4	31.3	1.1	47.4	5.6
T-07	1.604	4.170	0.236	2	29.8	0.9	49.1	3.7
T-08	1.668	4.043	0.184	2	29.4	0.8	52.3	3.1
T-09	1.081	3.209	0.189	5.8	23.5	1.1	47.4	9.2
T-10	1.290	3.104	0.202	5.7	23.6	1.1	46.9	10.1
T-11	0.829	2.958	0.138	5.1	23.9	1.1	50.1	11.0
T-12	1.876	3.285	0.258	5.2	23.2	1.3	46.4	11.7
T-13	2.658	3.246	0.132	5.7	23.3	1.2	51.3	10.7
T-14	2.662	3.385	0.130	5.9	22.7	1.2	49.6	9.5
T-15	2.642	3.362	0.128	5.9	23.0	1.2	48.7	9.3
T-16	0.527	3.275	0.130	5.5	23.7	1.3	54.0	9.8
T-17	0.403	3.288	0.147	5.3	23.1	1.2	52.2	9.1
T-18	0.343	3.290	0.151	5.5	23.1	1.2	51.7	9.8

Table G–8: Calculated variables

Test #	$U_{desuperheater}$	U_{shx1}	U_{shx2}	$\Delta T_{in,\,shx1}$	$\frac{Q_{cooling}}{W_{shaft}}$	$\frac{W_{pumps}}{W_{motor}}$	$\Delta T_{16,\,subcooling}$	$\Delta T_{8,\,subcooling}$
T-19	0.955	3.292	0.150	5.7	23.1	1.2	51.2	9.7
T-20	1.288	3.441	0.150	5.8	22.9	1.1	50.8	9.3
T-21	0.471	3.402	0.145	6.1	23.0	1.1	50.9	9.3
T-22	0.289	3.347	0.141	6.2	22.7	1.0	51.3	9.2
T-23	0.206	3.324	0.105	6.1	24.3	1.2	49.6	3.7
T-24	0.496	3.254	0.065	6.9	23.6	1.2	54.4	4.1
T-25	0.736	3.387	0.173	7.1	23.3	1.1	46.4	3.6
T-26	0.675	3.318	0.171	7.2	23.2	1.1	46.0	3.6
T-27	0.526	3.401	0.167	7.3	22.9	1.1	43.9	3.3

Table G–9: Calculated variables

Test #	$\mathbf{LMTD_{absorber}}$	$\mathbf{LMTD_{desorber}}$	$\dot{G}_{mix,\,des}$	$\dot{G}_{mix,\,abs}$	$\dot{G}_{\sin k,\,abs}$	$\dot{G}_{source,\,des}$	$\dot{q}_{abs1}$	$\dot{q}_{abs2}$	$\dot{q}_{des1}$	$\dot{q}_{des2}$
			[kg/m^2·s]	[kg/m^2·s]	[kg/m^2·s]	[kg/m^2·s]	[kW/m^2]	[kW/m^2]	[kW/m^2]	[kW/m^2]
T-01	15.0	8.9	9.796	12.1	66.8	54.0	11.09	6.34	14.6	4.02
T-02	14.6	8.3	9.867	12.2	66.8	54.0	11.56	6.69	15.58	3.82
T-03	13.8	8.9	10.504	13.0	66.9	54.1	10.44	6.51	12.24	5.27
T-04	12.2	8.9	12.251	15.1	66.9	54.1	10.97	7.58	11.12	7.25
T-05	13.8	8.7	9.820	12.1	66.9	54.1	9.67	5.92	11.98	4.75

Table G–9: Calculated variables

Test #	$\mathbf{LMTD_{absorber}}$	$\mathbf{LMTD_{desorber}}$	$\dot{G}_{mix,\,des}$	$\dot{G}_{mix,\,abs}$	$\dot{G}_{\mathrm{sink},\,abs}$	$\dot{G}_{source,\,des}$	$\dot{q}_{abs1}$	$\dot{q}_{abs2}$	$\dot{q}_{des1}$	$\dot{q}_{des2}$
T-06	14.7	8.7	8.805	10.9	66.9	54.1	10.14	5.10	12.51	3.69
T-07	14.3	8.9	8.521	10.5	66.9	54.1	9.78	4.56	12.84	3.36
T-08	14.9	8.8	8.026	9.9	66.8	54.1	9.95	4.44	13.82	2.64
T-09	12.1	8.5	12.511	15.4	66.9	54.1	12.17	10.31	11.64	10.48
T-10	11.6	8.6	12.581	15.5	66.1	51.5	11.97	10.36	10.95	10.16
T-11	11.0	8.2	11.991	14.8	66.9	52.0	11.99	9.65	12.33	8.74
T-12	10.6	8.4	12.794	15.8	66.9	54.1	11.93	9.42	11.64	9.88
T-13	10.6	8.4	13.054	16.1	66.9	54.1	11.63	10.07	11.37	10.74
T-14	11.1	8.5	13.242	16.3	66.8	54.1	11.46	10.48	11.04	11.07
T-15	11.2	8.4	13.266	16.4	66.9	54.1	11.52	10.54	10.98	11.13
T-16	11.9	8.7	12.747	15.7	66.8	54.0	12.34	9.65	12.09	9.55
T-17	11.4	8.9	13.219	16.3	66.8	54.1	12.17	10.01	11.57	10.54
T-18	11.9	8.9	13.054	16.1	66.9	54.1	12.29	10.37	11.77	10.34
T-19	11.5	9.0	13.219	16.3	66.9	54.1	12.29	10.13	11.57	10.74
T-20	11.7	9.1	13.408	16.6	66.9	54.1	12.05	10.43	11.04	11.59
T-21	11.7	9.2	13.573	16.8	66.9	54.1	12.11	10.66	11.17	11.92
T-22	12.3	9.3	13.832	17.1	66.9	54.1	12.30	11.61	11.43	12.58
T-23	13.9	8.8	13.124	16.2	66.9	54.1	12.05	10.01	11.04	10.47
T-24	13.8	8.3	12.912	15.9	66.8	54.1	11.21	9.65	11.31	10.21
T-25	14.4	9.1	13.549	16.7	66.9	54.1	11.94	11.31	10.98	11.86

Table G–9: Calculated variables

Test #	$\mathbf{LMTD_{absorber}}$	$\mathbf{LMTD_{desorber}}$	$\dot{G}_{mix,\,des}$	$\dot{G}_{mix,\,abs}$	$\dot{G}_{\mathrm{sink},\,abs}$	$\dot{G}_{source,\,des}$	$\dot{q}_{abs1}$	$\dot{q}_{abs2}$	$\dot{q}_{des1}$	$\dot{q}_{des2}$
T-26	14.5	9.2	13.644	16.8	66.9	54.1	11.88	11.44	10.91	12.19
T-27	13.7	9.0	13.644	16.8	66.9	54.1	11.58	10.90	10.12	15.35

Table G–10: Calculated variables

Test #	$Re_{vap,\,desuperheater}$	$Re_{vap,\,shx2}$	$Re_{ws,\,shx1}$	$Re_{ws,\,shx2}$	$Re_{ss,\,shx1}$
T-01	7931	1764	326.6	33.72	712.8
T-02	8790	1965	288.2	29.99	779.7
T-03	7852	1735	380.2	39.44	723.5
T-04	9675	2120	425	45.01	874.5
T-05	6780	1490	382.3	39.37	635.3
T-06	6358	1398	328	33.49	574.3
T-07	6678	1479	289.7	29.93	589.4
T-08	6831	1526	243.3	25.21	595.8
T-09	10385	2314	397.7	42.88	954.3
T-10	10285	2288	408.9	43.63	942.9
T-11	10042	2243	375.8	39.59	901.8
T-12	9980	2205	441.1	46.3	910.8
T-13	10361	2297	438.3	46.42	952.4

Table G–10: Calculated variables

Test #	$Re_{vap,\ desuperheater}$	$Re_{vap,\ shx2}$	$Re_{ws,\ shx1}$	$Re_{ws,\ shx2}$	$Re_{ss,\ shx1}$
T-14	10670	2371	439.1	46.77	991.4
T-15	10730	2384	438.4	46.74	996
T-16	9750	2192	443.9	47.41	928.9
T-17	10516	2350	443.4	47.2	980.4
T-18	10223	2287	439.9	47.05	958.6
T-19	10445	2342	437.8	46.83	975.7
T-20	10708	2406	436	46.77	998
T-21	10922	2464	432.9	46.65	1022
T-22	11198	2539	432.1	46.91	1058
T-23	10510	2335	436.8	47.82	1004
T-24	10048	2253	434.7	48.09	984.3
T-25	11022	2478	430.5	47.94	1067
T-26	11147	2510	428.3	47.64	1074
T-27	11249	2551	420.2	47.28	1095